FINITE ELEMENT MODELING OF INTERNAL FLOW AND STABILITY OF DROPLETS LEVITATED IN ELECTRIC AND MAGNETIC FIELDS

By

YUNLONG HUO

A dissertation submitted in partial fulfillment of
the requirement for the degree of

DOCTOR OF PHILOSOPHY
(Mechanical Engineering)

WASHINGTON STATE UNIVERSITY
The school of Mechanical and Materials Engineering

AUGUST 2005

To the Faculty of Washington State University:

The members of the Committee appointed to examine the dissertation of YUNLONG HUO find it satisfactory and recommend that it be accepted.

_____
Chair

_____

_____

_____

ACKNOWLEDGMENTS

The author wishes to record here his indebtedness and gratitude to many who have contributed their time, knowledge and effort towards the fulfillment of this work. Particularly, he would like to express his heartfelt gratitude and thanks to Dr. Ben Q. Li for his invaluable guidance, supervision, encouragement and patience during the investigation.

The author would like to thank Dr. Gary, J. Cheng, Dr. P. Dutta, Dr. Deuk Heo, and Dr. P. Pedrow for their input in the thesis, their time and energy to serve on the examination committee. The classmates in the Dr. Li's Laboratory are also to be thanked for their assistance during the phase of the investigation. The author is also grateful to Mr. Michael Shook for being the consultants of computer facility.

The financial support of this work from the NASA (Grant #: NNM04AA17G) and the school of Mechanical and Materials Engineering is gratefully acknowledged.

The author also wants to express his appreciation to my wife, Cheng Yana, for her love, support and understanding throughout my studies. The author finally expresses his gratitude to his family, his parents, his parents-in-law, and his friends for their continuous support and encouragement.

FINITE ELEMENT MODELING OF INTERNAL FLOW AND STABILITY OF DROPLETS LEVITATED IN ELECTRIC AND MAGNETIC FIELDS

Abstract

by Yunlong Huo, Ph.D.
Washington State University
August 2005

Chair: Ben Q. Li

The present study presents the numerical model of the free surface deformation and oscillation, heat and mass transfer, and Marangoni flow in the electrostatically levitated droplets under microgravity conditions. The free surface deformation, heat and mass transfer, and Marangoni flow are also investigated in the electrostatically levitated droplets comprised of the immiscible liquid metals. The present study not only investigates the steady-state fluid flow and heat transfer, but also the transient fluid flow and heat transfer, which is important for the fundamental study of nucleation and crystal growth phenomena. The 3-D vertical and horizontal movement of the magnetically levitated droplet is also investigated in the present study.

The coupled boundary method is developed to predict the electric potential distribution in the electrostatically levitated droplets. The surface deformation is determined using the weighted residuals method to solve the normal stress balance equations. The complex 3-D fluid flow and heat transfer fields are solved by using the Galerkin finite element method. The computational methodology for the oscillation of the

electrostatically levitated droplets entails solving the Laplace equation by the boundary element method, solving the Navier-Stokes equations by the Galerkin finite element method, and the use of deforming elements to track the oscillating free surface shapes. The coupled boundary and finite element methods with edge element algorithm are applied to the solution of the movement of the conducting droplet in the magnetic levitation mechanism. The numerical model should be a useful toolkit for developing electrostatic and magnetic levitation systems for space applications as well as for planning relevant experiments in space shuttle flights or in the International Space Station under construction.

TABLE OF CONTENTS

LIST OF FIGURES

LIST OF TABLES

NOMENCLATURE

a	radius of a sphere
B	magnetic flux density
B	magnetic flux density in complex form
$C(r_i)$	geometric coefficient resulting from boundary integral formulation
C_p	heat capacity
D_{AB}	mass diffusivity coefficient
D	electric flux density
D	electric flux density in complex form
E_0	electric field intensity in the electrostatic levitation
E	electric field intensity
E	electric field intensity in complex form
H	magnetic field intensity
H	magnetic field intensity in complex form
f	frequency
F	force vector from numerical formulation
G	Green's function
$\overline{\overline{G}}$	Dyadic Green's function
$\hat{i}$	unit vector of ith component
J	electric current density
J	electric current density in complex form

k	thermal conductivity
k	Wave number
n (n_r, n_z)	outward normal, its r and z components
Q	net charge on the droplet
Q_c	critical charge
Q_o	laser beam heat flux constant
Re	Reynolds number, $Re = \rho V_{max} a_d / \mu$
r, $\hat{\mathbf{r}}$, r	point vector, unit vector, and r coordinate
R	distance measured from the center of the un-formed droplet
t	tangential vector
T, T_∞, T_r	temperature, temperature of surroundings, reference temperature
T_{max}, T_{min}	maximum and minimum temperatures
ΔT	difference between T_{max} and T_{min}
U_{max}	maximum velocity
u	velocity
X	free surface coordinate
z	z coordinate
z_c	center of mass along the z-axis

Greek

β	thermal expansion coefficient
ε_0	electric permittivity of free surface or region designated by Ω_2
ε	emissivity

∇	gradient operator
φ_{AB}	mass diffusivity coefficient
ϕ	shape function of velocity
Φ	electric potential
γ	surface tension
κ	geometric parameter for elliptical functions
η	molecular viscosity
ρ	density
Θ	shape function of temperature
ψ	shape function of pressure
ξ	shape function of molar concentration
σ	electrical conductivity
σ_e	surface charge distribution
σ_s	Stefan-Boltzmann constant
$\overline{\sigma}$	stress tensor
Ω	computational domain

Subscripts

d	droplet
i	the ith point
l	laser beam
1	outer layer region inside the droplet
2	region outside the droplet

3	inner layer region inside the droplet

Superscripts

i	the ith component
T	Matrix transpose
1	outer layer region inside the droplet
2	region outside the droplet
3	inner layer region inside the droplet

CHAPTER 1

INTRODUCTION

1.1 Introduction

Both electrostatic and magnetic levitation mechanisms have received more attention because of the broad theoretical and engineering application, such as the fundamental study of nucleation and crystal growth phenomena, the measurement of thermophysical properties of molten materials under microgravity conditions, melting metal without contamination, and high-speed magnetic levitated rails. The electrostatic levitation facilities have been designed in the United States and Japan, where the terrestrial experiments have been undergone in preparation for space shuttle flight experiments [Rhim, 1997a, b]. The magnetic levitation method has been proposed in German [Muhlbauer *et al*. 1991; Zgraja *et al*. 1991] in order to melt the metal without contamination. Later on, the TEMPUS unit for the thermophysical measurement in microgravity condition is designed by the German scientist and engineers [Flemings *et al*. 1996]. The melting metal droplets are used as the experimental and computational samples in most of the previous studies. Although the investigators have conducted the experimental and numerical studies of the droplets levitated in the electrostatic and magnetic fields, there is still much scope for further investigation in the numerical simulation of the levitated droplets.

The present research focuses on the numerical study of steady state and transient 3-D Marangoni convection, heat and mass transfer in electrostatically levitated droplets,

the 3-D moving study of the droplets in the magnetic levitation, the 2-D numerical study of the surface oscillation of the electrostatically levitated droplets, and the 2-D numerical study of the internal convection in the electrostatically levitated droplets comprised of immiscible liquid metals, which have not been investigated by other researchers. In the study of the physical phenomena in the electrostatic levitation mechanism, the boundary element and the weighted residuals methods are applied to iteratively solve for the electric field distribution and for the unknown free surface shapes. The Galerkin finite element method is employed to solve the thermal and fluid flow field in both the transient and steady states. The boundary and finite element method with the edge element are used to solve the electromagnetic fields in order to calculate the 3-D movement of the magnetically levitated droplets.

1.2 Literature Review

The investigation of the physical phenomena in the electrostatically and magnetically levitated mechanism has been widely studied experimentally and numerically over the past century. In an electrostatic levitator, droplets are suspended by the Coulomb forces that are generated by the interaction of charges impressed on the droplets and a static electric field surrounding them. As early as 1882, Lord Rayleigh, through asymptotic analysis, showed that there exists a threshold value of charges applied to the droplets before they become disintegrated. This threshold limits the size of a droplet that can be levitated in normal gravity condition. In microgravity environment, however, the Coulomb forces are mainly derived from induced charges and the applied electric field

and are to confine a liquid droplet at a desired location. This allows a liquid sample of large size to be positioned, which is important for measuring certain physical properties such as interdiffusion coefficients in undercooled binary alloys.

One major advantage of electrostatic levitation is that in principle it can be applied to a very wide range of materials including metals, insulators and semiconductors. At present, the author only studied the electrically conducting samples levitated in vacuum. From the Gauss Law, the electrical potential in the electrically conducting droplet will be kept the same value and thus the Maxwell stress tensor inside the droplet is uniform, as shown by the initial researchers [Taylor, 1966; Torza, 1971; Ajayi, 1978]. From Torza, *et al.,* an electric field induces a non-uniform distribution of electric pressure along the surface of a droplet. This may have a great effect on the planned experiment for the measurement of certain thermophysical properties such as melt viscosity and surface tension by induced droplet oscillation in microgravity.

Study of the behavior of an electrically charged droplet has been a subject of long history and new and emerging applications with the droplet have provided continuous thrusts for the research community. Analyses have been carried out on either an inviscid oscillation of charged droplets for simple electric field configuration and shape stability [Brown, 1980; Adornato, 1983; Tsamopoulos, 1984; Natarajan, Feng, 1990] or Marangoni convection in the limit of Stokes flow for a sample of a perfect sphericity [Sadhal, 1996]. Brown, *et al*. (1980) studied the equilibrium shapes and stability of rotating drops held together by surface tension through using the computer-aided analysis that used expansions in finite element basis functions. Adornato and Brown (1983) described asymptotic and Galerkin finite element calculations of the shape and stability

of a charged drop levitated in a uniform electric field. In their research, the finite element results confirmed the prediction of the asymptotic analysis and gave the limits of existence of stable drop shapes. Tsamopoulos and Brown (1984) investigated the moderate-amplitude axisymmetric oscillations of charged inviscid drops using a multiple-timescale expansion. Both frequency and amplitude modulation of the oscillation are predicted for drop motions starting from general initial deformations. In 1987, a nonlinear analysis of the non-axisymmetric shapes and oscillations of charged, conducting drops was carried out near the Rayleigh limit by Natarajan and Brown. They concluded that the drop shapes in the bifurcating family for values of charge just below the Rayleigh limit were prolate spheroids which were unstable to perturbations that have the same axis of symmetry, and the bifurcating shapes for values of charges just above the Rayleigh limit were oblate spheroids that were unstable to non-axisymmetric perturbations. Later on, Feng and Beard (1990) used the analytical method of multiple-parameter perturbations to study the nature of axisymmetric oscillations of electrostatically levitated drops. The oscillatory response at each frequency was studied, which consisted of several Legendre polynomials rather than one. The characteristic frequency for each axisymmetric mode decreased as the electric field strength increased.

Based on the analytic and simple numerical results, the experimental measurement of thermophysical properties has been developed using the high-temperature electrostatic levitator at the Jet Propulsion Laboratory [Rhim, 1993, 1997a; Paradis, 1999]. Rhim, *et al*. presented that six theromphysical properties of both solid and liquid conductive samples can be measured. The properties include density, thermal expansion coefficient, constant pressure heat capacity, total hemispherical emissivity,

surface tension, and viscosity. The system design and feedback control mechanism are mainly concerned on the experimental study of the electrostatic levitation.

Song and Li (2000a, 2000b, 2001) have recently used the coupled finite element and boundary element methods to predict the scalar potential distributions in the droplets levitated in the electrostatic fields. The coupled finite element and boundary element scheme was further integrated with a WRM-based algorithm to predict the free surface deformation of electrostatically levitated droplets. Results showed that an applied electrostatic field only generated a normal stress distribution along the droplet surface, which, combined with surface tension, caused the droplet to deform into an ellipsoidal shape in microgravity. Therefore, the internal flows must arise from other sources. Laser heating induced a non-uniform temperature distribution in the droplet, which in turn produced recirculating convection in the droplet. They have already carried out the 2-D numerical simulation for different materials and various operating conditions.

Although Song and Li's 2-D model (2000a, 2000b, 2001) is able to be implemented to simulate the single and double laser beam heating arrangements when two laser beams are placed at the poles or one beam is placed at both poles, it is impossible to calculate the complex 3-D flow structures, which result from the tetrahedral or octahedral heating arrangements. Therefore, the 3-D model should be introduced to deal the numerical study of steady-state and transient complex Marangoni convection and heat transfer in electrostatically levitated droplets. Nobody has used this kind of 3-D numerical model to calculate the complex internal convection levitated in the electric fields. In the present study, the 3-D model is created, and then the complicated physical phenomena is analyzed in order to provide useful data for developing electrostatic

levitation systems for space applications as well as for planning relevant experiments in space shuttle flights or in the International Space Station under construction. Corresponding to Feng's analytic method, the 2-D coupled finite element and boundary element methods are also renewed for the comprehensive explanation of the nature of axisymmetric oscillations of electrostatically levitated droplets. The effect of the viscous force is considered in the computation of the oscillation of the droplets levitated in the electric fields and the front tracking technique is used to update the velocity in the computation.

The first metallurgical process in magnetic levitation mechanism was patented in Germany [Muck, 1923]. About 30 years later, Okress *et al.* (1952) pioneered research on the topic of magnetic levitation, which analyzed the range from electrodynamics to transport phenomena in the magnetic levitation mechanism through using analytic and numerical methods. The subsequent years have seen considerable research efforts devoted to a better understanding of the magnetically levitated process. Rony (1969) studied magnetic levitation melting processes for metals. Mestel (1982) used an analytical approach to investigate the magnetically induced deformation and fluid flow in an isothermal droplet. Bayazitouglu and his students completely studied the physical phenomena associated with the magnetically-levitated droplets. Suryanarayana and Bayazitoglu (1991) considered the oscillations of an aspherical droplet subjected to different external forces such as the acoustic, electromagnetic, and combined acoustic-electromagnetic forces. Bayazitoglu and Sathuvalli (1994) calculated the Joule heating in the magnetically levitated conductive sphere. Bayazitoglu and Sathuvalli (1996) developed a method to calculate the Lorentz force on an electrically conducting sphere

placed in an arbitrary sinusoidally alternating magnetic field. In their research, they used multipole expansion to express the vector potential of the external magnetic field in terms of the source. The external magnetic field was calculated by using a gradient formula. Lohofer (1989) solved the underlying quasistatic Maxwell equations using analytic expansion in spherical harmonics and Bessel functions. The power absorption and lifting force in the conducting sphere exposed to the external, time-varying magnetic fields were analytically calculated. In his previous publication (1993), he studied the force and torque of an electromagnetically levitated metal sphere. Lohofer (1994) also analyzed the magnetization and impedance of an electrically conducting sphere, which was inductively coupled with an arbitrary, sinusoidally alternating current density distribution. Li (1993) presented an analytical study of the electromagnetic and thermal phenomena in magnetic levitation. Analysis showed that the power input, the lifting forces and the temperature distributions, both global and local, were proportional to the square of input current. At high frequency limit, the total power input and the temperature were proportional to the square root of applied frequency and inversely proportional to the square root of electrical conductivity. Li (1994a) reported an analytic study of magnetohydrodynamic phenomena in electromagnetic levitation processes. In his study, the flow was treated as a Stokes flow, and the turbulence in the system was accounted for by using a constant eddy viscosity model. Calculated results illustrated that the flow field was characterized by two toroidal recirculating loops, and was strongly correlated to the distribution of the curl of the force field, which in turn depended on the coil placement. Li (1994b) further analyzed the transient electrodynamics and fluid flow phenomena in a magnetically-levitated liquid sphere.

The numerical models were originally developed by Zong, *et al.* (1992, 1993). In their formulation the electromagnetic force field was calculated using a modification of the volume integral method and these results were then combined with the FIDAP code to calculate the steady state melt velocities and the transient evolution of the velocity and the temperature fields when the heating current is switched off. All these numerical studies focused on the isothermal melt flow and the detailed temperature effects were not considered. Later on, Song and Li (1998a, 1998b, 1999a) further developed the numerical models to couple the boundary and finite element methods. They addressed the research on how the free surface deformation would affect the Joule heating distribution and hence the temperature field in a droplet in magnetic levitation systems. Their study indicated that a more accurate assessment must include free surface deformation and sample position in the levitation potential well. Ai and Li (2004) addressed fluid flow instabilities and flow transition to turbulence chaotic motions through numerical analysis and turbulence in magnetic levitated droplets through numerical simulations. Their results indicated that both turbulence kinetic energy and dissipations attained finite values along the free surface of the droplets.

Although a lot of study has been implemented using the various methods such as the analytic, experimental, and numerical methods, many important issues remain still unknown, for example, the movement of droplets in the magnetic levitation mechanism. Only, Enokizono, *et al.,* (1995) investigated the simulation of the movement of metal in the levitation-melting apparatus. However, nodal-based elements are used in their boundary and finite element methods so that the spurious solution occurred. While various approaches may be applied to alleviate the problem, the approach in the present

study uses the edge elements to satisfy the divergence-free condition so as to eliminate the spurious solution. Consequently, both the finite element and boundary element interpolations are edge-based to ensure the finite and boundary element method compatibility. While possible in theory, the numerical implementation of an edge-based FEM/BEM method does not appear to have been attempted for the solution of electromagnetic-heating-moving problems in general 3-D geometries.

1.3 Objectives of Present Research

The major objectives of this research are to develop 2-D and 3-D numerical models for solving the electromagnetic, fluid flow, heat transfer, mass transfer and surface deformation phenomena in electrostatic and magnetic levitation mechanism under the microgravity conditions in order to provide information for the measurement of thermophysical properties and the fundamental study of nucleation and crystal growth phenomena. The numerical method can test the experimental results and predict the multi-physical phenomena that can not be implemented by using the analytical and experimental methods.

Various numerical studies are implemented in the electrostatically or magnetically levitated droplets. The 2-D coupled boundary and finite elements with a WRM-based algorithm are used to predict the free surface deformation with hydraulic effect and without hydraulic effect. The 3-D Galerkin finite element method is used to solve the Navier-Stokes and energy equations. The complex 3-D steady-state and transient Marangoni convection and heat transfer in electrostatically levitated droplets are

investigated using the 3-D finite element model. The 3-D coupled boundary and finite elements with edge elements are used to predict the droplet movement in the magnetic levitation mechanism.

1.4 Scope of Present Research

In the present study, eight major sections are discussed. Chapter 2 lists the complete mathematical statement of physical phenomena in the electrostatically and magnetically levitated droplets. Chapter 3 presents the detail of the computational methodology, which is used to solve governing equations and boundary conditions, as described in chapter 2. Chapter 4 discusses the numerical results of free surface deformation, and the steady state and transient 3-D Marangoni convection and heat transfer in electrostatically levitated droplets. Chapter 5 analyzes the solute transport phenomena in electrostatically levitated droplets under microgravity, based on the computational results of the free surface deformation, full 3-D Marangoni convection in chapter 4. Chapter 6 presents the free surface deformation and Marangoni convection in immiscible droplets positioned by an electrostatic field and heated by laser beams under microgravity. Chapter 7 shows the computed results of the oscillation of the electrostatically levitated droplet under microgravity. Chapter 8 depicts the 3-D movement of the conducting droplet in the magnetic levitation mechanism.

CHAPTER 2

PROBLEM STATEMENT

2.1 Electrostatically Levitated Droplets under Microgravity

Let us consider the problem as illustrated in Figure 2.1. An electrically conducting liquid droplet is immersed in a uniform electrostatic field, which is generated by placing two electrodes far apart (Figure 2.1a). By the principle of electrostatics, a constant potential is established on the surface of the droplet, and surface electric charges are induced so that the electric field inside the droplet is zero. The charge distribution is non-uniform along the surface and, when combined with a self-induced electric field local to the charges, results in a non-uniform electric surface force acting in the outnormal direction [Reitz, 1979]. This normal force combines with other surface forces to define the equilibrium shape of the droplet. The internal and tangential surface Maxwell stresses are both zero because the electric potential is constant everywhere inside the droplet by the Gauss law and thus there will be no convection resulting from the electric origin. Laser beams are applied to melt the sample and/or heat it up to a designated temperature. Figure 2.1b shows a heating arrangement with two laser beams directed at two poles. Various other laser beam arrangements are also considered in this study, including single beam, dual beam, tetrahedral and hexahedral beams. The heating will result in a non-uniform temperature distribution inside the droplet and cause convection if the surface tension of the liquid varies with the surface temperature, as for most metallic and semiconductor melts. Since the laser heating applied here is not necessarily axisymmetric, the surface

tension driven flows are bound to be three-dimensional. As shown later, very complex 3-D flow structures and temperature distributions are developed in a droplet for some heating conditions. One important objective of this present study is to develop an understanding of these complex transport phenomena under both steady and transient conditions, which each have specific applications for space materials processing and thermophysical property measurements.

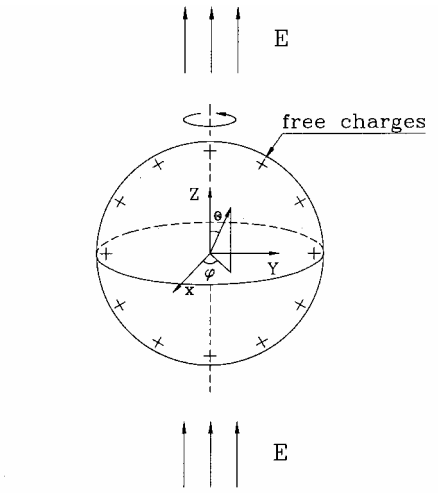

(a)

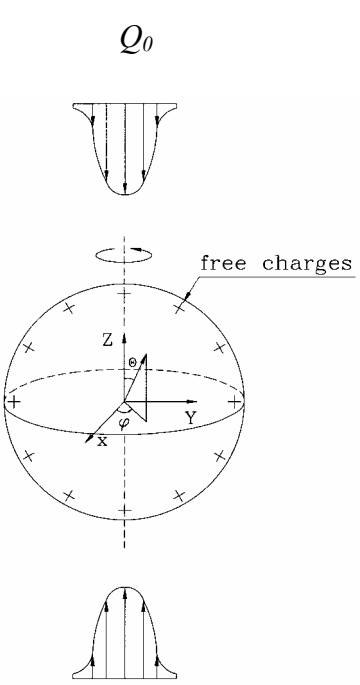

(b)

Figure 2.1 Schematic representation of a positively charged melt droplet levitated in an electrostatic field: (a) levitation mechanism and (b) two-laser-beam heating arrangement.

2.1.1 Governing equations and boundary conditions for the thermal convection in the electrostatically levitated droplet under microgravity

A complete description of the electrically induced surface deformation and thermally induced fluid flow phenomena in a droplet requires the solution of the coupled Maxwell and Navier-Stokes equations, along with the energy balance equation. However, for metal and semiconductor melts, the electric Reynolds number, $(\varepsilon_0/\sigma)V_{max}/a$, is on an order of 10^{-16}, which suggests that the convective transport of surface charges (or electric field) may be neglected and the electric field distribution can be calculated as if the liquid droplet were solid [James, 1981]. With this, the Maxwell equation is simplified to a partial differential equation governing the distribution of the electric field outside the droplet. The buoyancy effects being neglected for microgravity applications, the equations for the electric, fluid flow and thermal fields may be written as follows,

$$\nabla^2 \Phi = 0 \qquad \in \Omega_2 \qquad (2.1)$$

$$\nabla \cdot \mathrm{u} = 0 \qquad \in \Omega_1 \qquad (2.2)$$

$$\rho \frac{\partial \mathrm{u}}{\partial t} + \rho \mathrm{u} \cdot \nabla \mathrm{u} = -\nabla p + \nabla \cdot \eta \left(\nabla \mathrm{u} + (\nabla \mathrm{u})^T \right) \qquad \in \Omega_1 \qquad (2.3)$$

$$\rho C_p \frac{\partial T}{\partial t} + \rho C_p \mathrm{u} \cdot \nabla T = \nabla \cdot k \nabla T \qquad \in \Omega_1 \qquad (2.4)$$

where Ω_1 and Ω_2 refer to the regions inside the droplet and outside the droplet respectively. Φ is the electric potential, u the velocity, p the pressure, and T the temperature. Also, η is the molecular viscosity, ρ the density, C_p heat capacity, and k

thermal conductivity. The solution of above electric field, fluid flow and heat transfer equations may be obtained by applying the appropriate boundary conditions, which are stated below,

$$\Phi = \Phi_0 \qquad \in \Omega_1 \cap \Omega_2 \qquad (2.5)$$

$$\varepsilon_0 \mathbf{n} \cdot \nabla \Phi = -\sigma_e \qquad \in \Omega_1 \cap \Omega_2 \qquad (2.6)$$

$$\oiint_{\partial\Omega_1} \sigma_e ds = -\oiint_{\partial\Omega_1} \varepsilon_0 \mathbf{n} \cdot \nabla \Phi ds = Q \qquad \in \Omega_1 \cap \Omega_2 \qquad (2.7)$$

$$\Phi = -E_0 R \cos\theta \qquad R \to \infty \qquad (2.8)$$

$$-k\mathbf{n} \cdot \nabla T = \varepsilon\sigma_s \left(T^4 - T_\infty^4\right) + \mathbf{n} \cdot \hat{\mathbf{r}}_l Q_o e^{-r_l^2/a_l^2} \qquad \in \Omega_1 \cap \Omega_2 \qquad (2.9)$$

$$\mathbf{u} \cdot \mathbf{n} = 0 \qquad \in \Omega_1 \cap \Omega_2 \qquad (2.10)$$

$$\mathbf{n} \cdot \overline{\sigma} \cdot \mathbf{n} + K - \mathbf{n} \cdot \mathbf{T}_E \cdot \mathbf{n} = 2H\gamma \qquad \in \Omega_1 \cap \Omega_2 \qquad (2.11)$$

$$\mathbf{t} \cdot \overline{\sigma} \cdot \mathbf{n} = \frac{d\gamma}{dT} \mathbf{t} \cdot \nabla T \qquad \in \Omega_1 \cap \Omega_2 \qquad (2.12)$$

$$\int_{\Omega_1} dV = V_0 \qquad \in \Omega_1 \cap \Omega_2 \qquad (2.13)$$

$$\int_{\Omega_1} z dV = z_c \qquad \in \Omega_1 \cap \Omega_2 \qquad (2.14)$$

In the above, Eq. (2.6) is the jump condition for the electric field along the droplet surface, a manifestation of a well known fact that charges are distributed only on the surface of a conducting body. Eq. (2.8) describes the electric potential condition at infinity. The law of charge conservation is described by Eq. (2.7), where Q is the total free charge applied on the droplet, which is zero for the problem under consideration for

microgravity applications. In Eq. (2.9), the absorption coefficient is factored into Q_o and $\hat{\mathbf{r}}_l$ the unit vector of laser beam pointing outward from the origin of the laser, i.e., $\mathbf{n} \cdot \hat{\mathbf{r}}_l \leq 0$. Eq. (2.11) describes the balance of the hydrodynamic, Maxwell and surface tension stresses along the normal direction, which determines the shape of the droplet. The last equation represents the fact that the flow along the surface of the droplet is induced by surface tension force if it is a function of temperature. The constraints of the volume conservation (Eq. (2.13)) and the center of the mass (Eq. (2.14)) of the electrostatically levitated droplet are needed to determine the shape and position of the droplet.

2.1.2 Governing equations and boundary conditions for the mass transfer in the electrostatically levitated droplet under microgravity

For some applications such as impurity doping and diffusivity measurements [Johnson, 2002], foreign material may be continuously introduced on the surface once flow is established. A strong recirculation in the droplet will likely play an important role in transporting the impurity from the surface to the inside, as sketched in Figure 2.2. A quantitative assessment of the convection effect on the impurity transport in the droplet will be made in this study for the conditions of relevance to diffusion coefficient measurements [Johnson, 2002].

The deformation, fluid flow and heat transfer is calculated from eq. (2.1) to eq. (2.14). Combined with the above equations, the governing equation for mass transfer may be written as follows,

$$\frac{\partial C}{\partial t} + \mathbf{u} \cdot \nabla C = \nabla \cdot D_{AB} \nabla C \qquad \in \Omega_1 \qquad (2.15)$$

The solution of the above mass transfer equation is obtained by applying the appropriate boundary conditions, which are stated below

$$C = 1 \qquad \text{for } t > t_0 \qquad \in \Omega_1 \cap \Omega_3 \qquad (2.16)$$

$$C = 0 \qquad \text{at } t = 0 \qquad \in \Omega_1 \qquad (2.17)$$

where Ω_3 refer to the metal solute layer on the surface of the droplet, D_{AB} the mass diffusivity coefficient. Eqs. (2.16-2.17) are the boundary and initial conditions for the concentration distribution. The concentration is non-dimensionalized such that the value on the surface of the droplet is unity. Here it is tacitly assumed that the surface concentration is uniform, which may be approximately achieved by rotating the flux deposition source. Of course, other conditions may also be used if they are known. Note that the boundary and initial conditions for the concentration, as set in Eqs. (2.16) and (2.17), represent the situation in which impurities are applied after the heating and flow have already established.

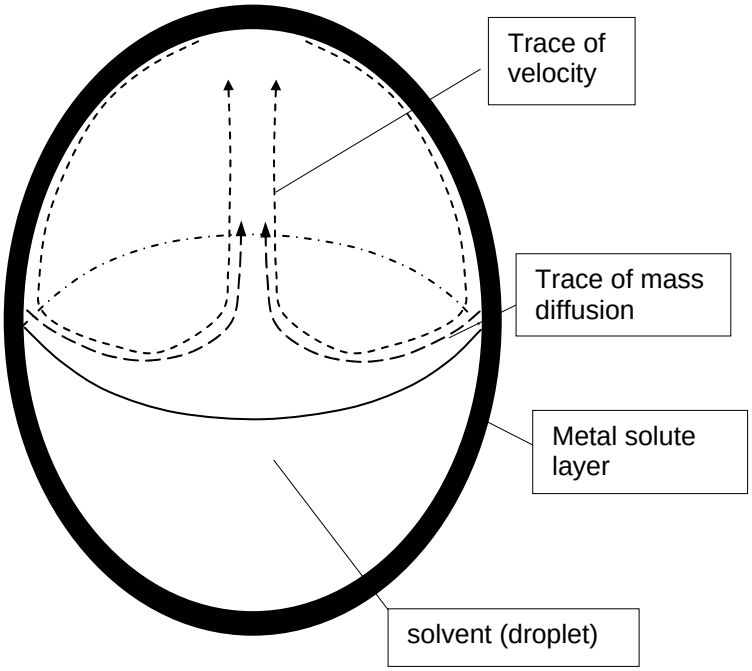

Figure 2.2 Schematic representation of solute transport in the outer layer into the heated droplet. Note that the solute concentration at the surface is dilute but kept at a constant.

2.1.3 Governing equations and boundary conditions for the thermal convection in the electrostatically levitated droplet comprised of immiscible liquid metals under microgravity

A positively charged droplet comprised of immiscible liquid metals levitated in an electrostatic field is also investigated in the present study. The numerical model is capable of providing the significant information about the internal convection in the droplet, which is useful for the thermophysical measurement for the immiscible liquid metals. Like the equations described in section 2.1.1, a complete description of the

electrically induced surface deformation and thermally induced fluid flow phenomena in a droplet comprised of immiscible liquid metals requires the solution of the coupled Maxwell and Navier-Stokes equations, along with the energy balance equation in different regions. The buoyancy effects being neglected for microgravity applications, the equations for the electric, fluid flow and thermal fields may be written as follows,

$$\nabla^2 \Phi = 0 \qquad \in \Omega_2 \qquad (2.18)$$

$$\nabla \cdot \mathbf{u}_j = 0 \qquad \in \Omega_1 \cup \Omega_3 \qquad (2.19)$$

$$\rho \frac{\partial \mathbf{u}_j}{\partial t} + \rho \mathbf{u}_j \cdot \nabla \mathbf{u}_j = -\nabla p_j + \nabla \cdot \eta_j \left(\nabla \mathbf{u}_j + (\nabla \mathbf{u}_j)^T \right) \qquad \in \Omega_1 \cup \Omega_3 \qquad (2.20)$$

$$\rho_j C_{p_j} \frac{\partial T_j}{\partial t} + \rho_j C_{p_j} \mathbf{u}_j \cdot \nabla T_j = \nabla \cdot k_j \nabla T_j \qquad \in \Omega_1 \cup \Omega_3 \qquad (2.21)$$

where j (= 1, 3) with the subscript 1 refers to the outer layer of the droplet and 3 to the inner layer. The solution of above electric field, fluid flow and heat transfer equations may be obtained by applying the appropriate boundary conditions, which are stated below,

$$\Phi = \Phi_0 \qquad \in \Omega_1 \cap \Omega_2 \qquad (2.22)$$

$$\varepsilon_0 \mathbf{n}_1 \cdot \nabla \Phi = -\sigma_e \qquad \in \Omega_1 \cap \Omega_2 \qquad (2.23)$$

$$\oiint_{\partial\Omega_1 \cap \partial\Omega_2} \sigma_e \, ds = - \oiint_{\partial\Omega_1 \cap \partial\Omega_2} \varepsilon_0 \mathbf{n} \cdot \nabla \Phi \, ds = Q \qquad \in \Omega_1 \cap \Omega_2 \qquad (2.24)$$

$$\Phi = -E_0 R \cos\theta \qquad R \to \infty \qquad (2.25)$$

$$-k\mathbf{n}_1 \cdot \nabla T_1 = \varepsilon\sigma_s\left(T_1^4 - T_\infty^4\right) + \mathbf{n}_1 \cdot \hat{\mathbf{r}}_l Q_o e^{-r_l^2/a_l^2} \qquad \in \Omega_1 \cap \Omega_2 \qquad (2.26)$$

$$\mathbf{u} \cdot \mathbf{n}_1 = 0 \qquad \in \Omega_1 \cap \Omega_2 \qquad (2.27)$$

$$\mathbf{n}_1 \cdot \bar{\sigma}_1 \cdot \mathbf{n}_1 + K - \mathbf{n}_1 \cdot \mathbf{T}_E \cdot \mathbf{n}_1 = 2H\gamma \qquad \in \Omega_1 \cap \Omega_2 \qquad (2.28)$$

$$\mathbf{t}_1 \cdot \bar{\sigma}_1 \cdot \mathbf{n}_1 = \frac{d\gamma}{dT}\mathbf{t}_1 \cdot \nabla T_1 \qquad \in \Omega_1 \cap \Omega_2 \qquad (2.29)$$

$$\mathbf{u}_1 = \mathbf{u}_3 \qquad \in \Omega_1 \cap \Omega_3 \qquad (2.30)$$

$$T_1 = T_3 \qquad \in \Omega_1 \cap \Omega_3 \qquad (2.31)$$

$$\mathbf{n}_3 \cdot \bar{\sigma}_3 \cdot \mathbf{n}_3 - \mathbf{n}_3 \cdot \bar{\sigma}_1 \cdot \mathbf{n}_3 = 2H\gamma_3 \qquad \in \Omega_1 \cap \Omega_3 \qquad (2.32)$$

$$\mathbf{t}_3 \cdot \bar{\sigma}_3 \cdot \mathbf{n}_3 - \mathbf{t}_3 \cdot \bar{\sigma}_1 \cdot \mathbf{n}_3 = \frac{d\gamma_3}{dT}\mathbf{t}_3 \cdot \nabla T \qquad \in \Omega_1 \cap \Omega_3 \qquad (2.33)$$

$$\int_{\Omega_1+\Omega_3} dV = V_0 \qquad \in \Omega_1 \cup \Omega_3 \qquad (2.34)$$

$$\int_{\Omega_1+\Omega_3} z\, dV = z_c \qquad \in \Omega_1 \cup \Omega_3 \qquad (2.35)$$

In the above, eqs. (2.22-2.29, 2.34-2.35) have the same formulation like that in section 2.1.1 except that they are calculated in the droplet comprised of the immiscible metals. Eqs. (2.30-2.31) respectively present that the velocity and temperature are the same on the surface between the immiscible liquid metals. The normal and tangential stress balance is represented by Eqs. (2.32-2.33)

It is noted that in the above formulations, the effect of surrounding gas is omitted. The liquid droplet is generally processed under a vacuum condition, although recently attempts have been made to process in an inert gas environment. For the latter case, it is

estimated that the surrounding inert gas contributes about 3% or less to the Marangoni convection.

2.1.4 Governing equations and boundary conditions for the computation of the oscillation of the electrostatically levitated droplet under microgravity

In the study of the oscillation of electrostatically levitated droplets under microgravity, Eqs. (2.1-2.3) are the governing equations. Parts of the boundary conditions may be expressed in Eqs. (2.5-2.8), Eq. (2.11), and Eqs. (2.13-2.14). Also one additional boundary condition is needed, as shown below.

$$(\mathbf{u} - \mathbf{u_s}) \cdot \mathbf{n} = 0 \qquad \in \Omega_1 \cap \Omega_2 \qquad (2.36)$$

where $\mathbf{u_s}$ is surface velocity. Along the free surface of the droplet, eq. (2.36) results in the following boundary condition:

$$\frac{\mathbf{dX}}{\mathbf{dt}} + \mathbf{u} \cdot \nabla \mathbf{X} = \mathbf{0} \qquad \in \Omega_1 \cap \Omega_2 \qquad (2.37)$$

with $\mathbf{X}$ being the free surface coordinates.

2.2 Magnetically Levitated Droplets under Microgravity

Figure 2.3 shows the TEMPUS device in use [Song, 1998a, 1998b, 1999a]. The system consists of two types of coils: (1) the inner four current loops (or heating coils) for sample heating and melting, and (2) the outer eight loops (or positioning coils) for sample positioning in space. During the operation, AC currents flow through these coils to generate an appropriate magnetic field. In magnetic levitation, eddy currents are induced in the sample and the dot product of eddy currents generates the Joule heating for the melting of the sample. These eddy currents also interact with the applied and induced magnetic fields to produce the Lorentz force in the sample. At present, we investigate the effect of the Lorentz force on the metal's movement in the magnetic levitation mechanism.

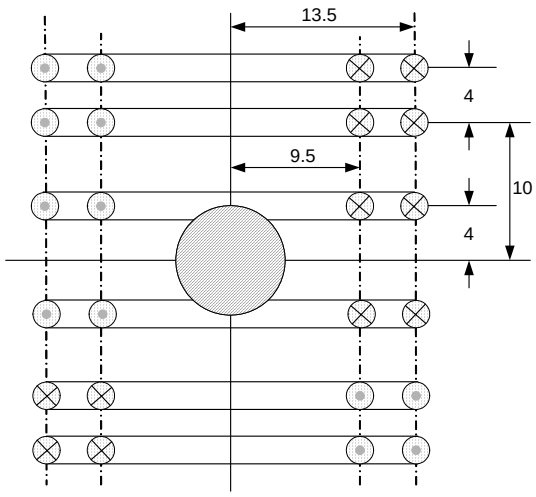

Figure 2.3 Schematic representation of magnetic levitation System

2.2.1 Governing equations and boundary conditions for the computation of the electromagnetic field

In order to calculate the distribution of electromagnetic fields in the specimen surrounded by the exciting coils, the Maxwell's equations have to be solved. The Maxwell's equations is written as follows,

$$\nabla \times E = -\frac{\partial B}{\partial t} \tag{2.38}$$

$$\nabla \times H = J_i + J_c + \frac{\partial D}{\partial t} \tag{2.39}$$

$$\nabla \cdot B = 0 \tag{2.40}$$

$$\nabla \cdot D = \rho_e \tag{2.41}$$

When the electromagnetic field is time-harmonic, the Maxwell's equations may be rewritten,

$$\nabla \times \mathbf{E} = -j\varpi\mathbf{B} \tag{2.42}$$

$$\nabla \times \mathbf{H} = \mathbf{J}_\mathbf{i} + \mathbf{J}_\mathbf{c} + j\varpi\mathbf{D} \tag{2.43}$$

$$\nabla \cdot \mathbf{B} = 0 \tag{2.44}$$

$$\nabla \cdot \mathbf{D} = \boldsymbol{\rho}_\mathbf{e} \tag{2.45}$$

with the constitutive equations as described below

$$D = \varepsilon E \qquad \mathbf{D} = \varepsilon \mathbf{E} \tag{2.46}$$

$$B = \mu H \qquad \mathbf{B} = \mu \mathbf{H} \tag{2.47}$$

$$J_c = \sigma E \qquad \mathbf{J_c} = \sigma \mathbf{E} \tag{2.48}$$

and the general boundary conditions described as follow,

$$n \times (E_2 - E_1) = 0 \qquad n \times (\mathbf{E}_2 - \mathbf{E}_1) = 0 \tag{2.49}$$

$$n \cdot (D_2 - D_1) = q_e \qquad n \cdot (\mathbf{D}_2 - \mathbf{D}_1) = q_e \tag{2.50}$$

where E (**E**) is the electric field intensity, H (**H**) the magnetic field intensity, D (**D**) the electric flux density, B (**B**) the magnetic flux density, J_i ($\mathbf{J_i}$) impressed electric current density, J_c ($\mathbf{J_c}$) conduction electric current density, ρ_e ($\boldsymbol{\rho}_\mathbf{e}$) electric charge density, ε permittivity, μ permeability, and σ conductivity.

However, Maxwell's equations are coupled partial differential equations, which have more than one unknown variables. Therefore, the vector wave equation derived from the Maxwell's equations combined with the energy equation is taken as the governing equations to simulate the microwave heating problems. With the analysis above, the equations for the electric and thermal fields may be written as follows

$$\nabla \times \frac{1}{\mu_r} \nabla \times \mathbf{E} - \omega^2 \mu \varepsilon_c \mathbf{E} = -j\omega\mu \mathbf{J}_i \tag{2.51}$$

In the above, $\mathbf{J}_i$ is an impressed or source current, and ε_c (=ε-jσ/ω) results from the combination of the induced current ($\sigma\mathbf{E}$) and displacement current (j$\omega\mathbf{D}$). The appropriate boundary conditions are stated below.

$$-\frac{1}{\mu_{r1}}\hat{\mathbf{n}}_1 \times \nabla \times \mathbf{E}_1 = -\mathbf{U}_1 = \mathbf{U}_2 = \hat{\mathbf{n}}_2 \times \nabla \times \mathbf{E}_2 \qquad \in \Omega_1 \cap \Omega_2 \qquad (2.52)$$

where Ω_1 and Ω_2 are the FEM domain, BEM domain respectively. $\hat{\mathbf{n}}_1$ is outnormal from the FE region, and $\hat{\mathbf{n}}_2$ is outnormal from the BE region.

2.2.2 Governing equations and boundary conditions for the computation of the movement of the droplet in the magnetic levitation mechanism

After the computation of the electromagnetic field, the time-averaged electromagnetic force induced in the sphere which is responsible for levitation as well as for fluid motion, is the cross product of induced current and the complex conjugate of the magnetic field,

$$\mathbf{F} = \frac{\mathbf{1}}{\mathbf{2}}\mathrm{Re}(\mathbf{J} \times \mathbf{B}^*) \qquad (2.53)$$

$$\mathbf{F}_{\mathbf{total}} = \int_V \mathbf{F} \cdot dV \qquad (2.54)$$

where *i* is the element number. As the levitating motion, we considered the translation. Therefore, the translation equations are introduced into this analysis. The Leap Frog

Algorithm is used. This algorithm evaluates the velocities at half-integer time steps and uses these velocities to compute new positions.

$$\mathrm{v}^{\mathrm{n}+\frac{1}{2}} \equiv \frac{s^{n+1} - s^{n}}{\Delta t} \tag{2.55}$$

$$\mathrm{v}^{\mathrm{n}-\frac{1}{2}} \equiv \frac{s^{n} - s^{n-1}}{\Delta t} \tag{2.56}$$

So we can derive the new position, based on the old position and velocity:

$$\mathrm{s}^{\mathrm{n}+1} = \mathrm{s}^{\mathrm{n}} + \Delta \mathrm{t} \mathrm{v}^{n+\frac{1}{2}} \tag{2.57}$$

From the Verlet algorithm, we have the following expression for velocity:

$$\mathrm{v}^{\mathrm{n}+\frac{1}{2}} = \mathrm{v}^{\mathrm{n}+\frac{1}{2}} + \Delta t \mathrm{a}^{\mathrm{n}} \tag{2.58}$$

$$\mathrm{a}^{\mathrm{n}} = \mathrm{F}_{\mathrm{total}}^{n} / \mathrm{m} \tag{2.59}$$

where **a** is the acceleration, **m** is the weight of the metal, Δ**t** the width of time step, **v** the velocity at center of the metal and **s** the position vector. The fluid flow and temperature distribution may also be calculated at every time step.

After the time-averaged electromagnetic force is calculated, the torque with respect to the axis may be written as follows,

$$N_{ti} = \mathrm{R}_i \times \mathrm{F}_{ti} \tag{2.60}$$

$$\mathrm{N}_{\mathrm{total}} = \sum_{i=1} N_{ti} \tag{2.61}$$

The rotating moving equations at every time step are given by,

$$\omega^{n+1} = \omega^{\mathrm{n}} + \Delta\omega^n \tag{2.62}$$

$$\theta^{n+1} = \theta^{\mathrm{n}} + \Delta\theta^n \tag{2.63}$$

with

$$\Delta\omega^n = \mathrm{N}_{\mathrm{total}} \Delta t / I_m \tag{2.64}$$

$$\Delta\theta^n = \omega^n \Delta t + \mathrm{N}_{\mathrm{total}} \Delta t^2 / (2I_m) \tag{2.65}$$

where R_i is the radius vector drawn from center to surface of a sphere metal, ω the angular velocity, θ the rotational angle, and I_m the moment of inertia. In the present study, the droplet is assumed to be spherical without considering the deformation of the droplet. Therefore, the moment of inertia I_m may be written as,

$$I_m = (2/5)\mathrm{mR}^2$$

where m is the weight of the droplet, R the radius of the spherical droplet.

CHAPTER 3

NUMERICAL SOLUTIONS

In the present study of the droplet in electric levitation mechanism, the electric field is calculated by the boundary element method (BEM) and the shape deformation by the Weighted Residuals method. The numerical model for the transport phenomena is developed based on the Galerkin finite element solution (FEM) of the Navier-Stoke equations, the energy balance equation and the mass transport equation. The computational models developed here enable the prediction of the electric field distribution, electric pressure distribution along the surface of a droplet, droplet shapes, the internal fluid flow, thermal and solute distributions in electrostatically positioned droplets. For the movement of the droplet in the magnetic levitation mechanism, the numerical models are implemented using the boundary and finite element method with edge elements to calculate the electromagnetic fields in the conducting droplets. And then the force is calculated by the integral volume of the droplet, which is used in the dynamic equations to solve the movement of the droplet. From now on, unless otherwise indicated, the FEM and BEM respectively represent the finite element method and boundary element method.

3.1 An Introduction to the FEM and BEM

Let's begin with an introductory definition of the finite element method (FEM): The FEM is a computer-aided mathematical technique for obtaining approximate numerical

solution of the physical phenomena subject to the external influence. The FEM originally arises from the area of solid mechanics (elasticity, plasticity, statics, and dynamics). Applications to date have been expanded to the broad field of engineering science such as heat transfer (conduction, convection and radiation), fluid mechanics (inviscid or viscous, compressible or incompressible), acoustics, and electromagnetics.

The basic idea of the FEM is summarized as follows: (a). the domain of the problem is partitioned into smaller regions, called elements, (b). in each element the governing equations are transformed into algebraic equations, called the element equations, (c). the terms in the element equations are numerically evaluated for each element in the mesh, (d). the resulting numbers are assembled into a much larger set of algebraic equations, called the system equations, (e). the system equations are solved by using the numerical technique on computer, (f). the final operation displays the solutions to tabular, graphical, or pictorial form.

There are two types of optimizing route leading to the FEM formulation: (a). methods of weighted residuals (MWR), which are applicable when the governing equations are differential equations, (b). variational method (VM), which is applicable when the governing equations are variational (integral) equations. The MWR seek to minimize the residue in the differential equations. There are four basic types in the MWR route: (a). the collocation method, (b). the subdomain method, (c). the least-squares method, (d). the Galerkin method. The variational principles try to minimize some physical quantity, such as energy.

Over recent decades, the boundary element method (BEM) has received much attention from researchers and has become an important technique in the computational

solution of a number of physical problems. It is based on the boundary integral equation and the methods of weighted residuals, where the Green's function of the corresponding governing equation is chosen as the trial function. The advantages in the boundary element method arise from the fact that only the boundary of the domain requires sub-division. The method is particularly suited to solve problems with boundaries at infinity. The method includes the following steps: (a). the surface of the domain of the problem is partitioned into smaller regions, called boundary element, (b). the Green's function is selected as the trial function and the governing equations are transformed into algebraic equations on the boundary elements, (c). the final element matrix is assembled over element by element, (d). the system equations are solved by using the numerical technique on computer.

3.2 Computation of the Deformation of the Droplet in the Electric Levitation Mechanism

As stated in chapter 2, for practical applications, droplet deformation is essentially axisymmetric and viscous forces make a negligible contribution. Thus, the electric and droplet deformation calculations may be decoupled from the thermal and fluid calculations. The procedures for the computation of electrically induced droplet deformation are detailed in our previous publications [Huo, 2004a, 2004b, 2005a]. Since the electric field inside the droplet is zero, only the potential distribution outside needs to be solved for.

3.2.1 Computation of the distribution of the electric potential

We now apply the BEM to determine the scalar electric potential in the exterior region of the droplet levitated in the electric field. We are seeking an approximate solution to the problem governed by

$$\nabla^2 \Phi = 0 \qquad \in \Omega_2 \qquad (3.1)$$

which is the same as Eq. (2.1). The error introduced by replacing Φ by an approximate solution can be minimized by writing the following weighted residual statement:

$$\int_{\Omega_2} \nabla^2 \Phi(r) G(r_i, r) d\Omega(r) = \int_{\Gamma} q(r) G(r_i, r) d\Gamma(r) - \int_{\Gamma} \Phi(r) q^*(r_i, r) d\Gamma(r) \qquad (3.2)$$

where G is interpreted as a weighting function and

$$q^*(r_i, r) = \frac{\partial G(r_i, r)}{\partial n(r)} \qquad (3.3)$$

The integration of Eq. (3.3) by parts with respect to x_i gives

$$-\int_{\Omega_2} \frac{\partial \Phi(r)}{\partial x_i(r)} \frac{\partial G(r_i, r)}{\partial x_i(r)} d\Omega(r) = -\int_{\Gamma} q(r) G(r_i, r) d\Gamma(r) + \int_{\Gamma} \Phi(r) q^*(r_i, r) d\Gamma(r) \qquad (3.4)$$

where *i*= 1, 2, 3 and Einstein's summation convection for repeated indices is implied. Integrating by parts once more,

$$\int_{\Omega_2} \nabla^2 G(r_i, r) u(r) d\Omega(r) = -\int_{\Gamma} q(r) G(r_i, r) d\Gamma(r) + \int_{\Gamma} \Phi(r) q^*(r_i, r) d\Gamma(r) \tag{3.5}$$

Assuming *G* to be fundamental solution to Laplace's equations means that

$$\nabla^2 G(r_i, r) = -2\alpha\pi\delta(r_i, r) \tag{3.6}$$

where δ is the Dirac Delta function. Here G is the Green's function. Substituting Eq. (3.6) into Eq. (3.5) gives

$$2\alpha\pi\Phi(r_i) + \int_{\Gamma} \Phi(r) q^*(r_i, r) d\Gamma(r) = \int_{\Gamma} q(r) G(r_i, r) d\Gamma(r) \tag{3.7}$$

So, taking the point r_i to the boundary and accounting for the jump of the left-hand side integral in Eq. (3.7) yields the boundary integral equation

$$C(r_i)\Phi(r_i) + \int_{\Gamma} \Phi(r) q^*(r_i, r) d\Gamma(r) = \int_{\Gamma} q(r) G(r_i, r) d\Gamma(r) \tag{3.8}$$

After some transformation, we can get the final form used for the BEM simulation.

$$C(r_i)\Phi'(r_i) + \oint_{\partial\Omega_2} \Phi'(\mathbf{n}\cdot\nabla G)rd\Gamma + \oint_{\partial\overline{\Omega}_2} \Phi'(\mathbf{n}\cdot\nabla G)rd\Gamma = \oint_{\partial\Omega_2} G(\mathbf{n}\cdot\nabla\Phi')rd\Gamma + \oint_{\partial\overline{\Omega}_2} G(\mathbf{n}\cdot\nabla\Phi')rd\Gamma \tag{3.9}$$

where

$$C(r_i) = \begin{cases} 1; & \text{when } r_i \text{ lies inside domain} \\ \dfrac{1}{2}; & \text{when } r_i \text{ lies on a smooth domain} \\ \dfrac{2\pi - \beta_1 - \beta_2}{2\pi}; & \text{when } r_i \text{ lies on a nonsmooth domain} \end{cases}$$

and $\Phi' = \Phi + Er\cos\theta$, $\partial\Omega_2$ designates the surface of the droplet and $\partial\overline{\Omega}_2$ denotes the boundary at infinity. The Green function, G, and its normal derivative are calculated by the following expressions written for a cylindrical coordinate system [Jackson, 1975].

$$G(r_i, r) = \frac{4}{\sqrt{(r_i + r)^2 + (z - z_i)^2}} K(\kappa) \tag{3.10}$$

$$\frac{\partial G}{\partial n} = \frac{4}{\sqrt{(r + r_i)^2 + (z - z_i)^2}} \left\{ \begin{array}{l} \dfrac{n_r}{2r}\left[E(\kappa) - K(\kappa)\right] - \\ \dfrac{n_r(r - r_i) + n_z(z - z_i)}{(r - r_i)^2 + (z - z_i)^2} E(\kappa) \end{array} \right\} \tag{3.11}$$

where κ is the geometric parameter calculated by

$$\kappa^2 = \frac{4r_i r}{(r_i + r)^2 + (z_i - z)^2} \tag{3.12}$$

The function G and Φ' have the following asymptotic properties,

$$\Phi'(r_i, R) \approx O(R^{-2}), \quad \frac{\partial \Phi'}{\partial n}(r_i, R) \approx O(R^{-3}) \text{ as } R \to \infty \tag{3.13}$$

$$G(r_i, R) \approx O(R^{-2}), \quad \frac{\partial G}{\partial n}(r_i, R) \approx O(R^{-3}) \text{ as } R \to \infty \tag{3.14}$$

Also $d\Gamma = R(\theta)\, d\theta$. Thus, the two integrals each approach zero as $R \to \infty$,

$$\oint_{\partial \Omega_2} \Phi'(\mathbf{n} \cdot \nabla G) r d\Gamma \to 0 \text{ and } \oint_{\partial \Omega_2} G(\mathbf{n} \cdot \nabla \Phi') r d\Gamma \to 0 \text{ as } R \to \infty \tag{3.15}$$

Thus, Eq. (3.9) simplifies to a boundary integral that involves only the surface of the droplet, $\partial\Omega_2$. Following the standard boundary element discretization, noticing that the potential on the surface is a constant and substituting $\Phi = \Phi' - Er\cos\theta$ into the resultant equation, one obtains the final matrix form for the unknowns on the surface of the droplet,

$$\mathbf{H}\{\Phi_0\} = -\mathbf{G}\left\{\frac{\partial \Phi}{\partial n}\right\} + E\mathbf{G}\left\{\frac{\partial z}{\partial n}\right\} - \mathbf{H}E\{z\} \tag{3.16}$$

where **H** and **G** are the coefficient matrices involving the integration of $\partial G/\partial n$ and G over a boundary element. To complete the solution, Eq. (2.8) is discretized and solved along with the above equation to obtain the surface distribution of $\partial\Phi/\partial$n and the constant Φ_0.

3.2.2 Computation of the deformation of the droplet

The study of the free surface deformation of the electrostatically levitated droplet plays an important role in the future computation of the fluid flow and temperature distribution. In particular, it can affect the ratio of the radiation when the laser beams are switch off. For the electrostatically levitated droplet, its shape is determined by the hydrostatic pressure, the electrostatic pressure and the surface tension of the liquid, as shown in Eq. (2.11). The normal stress balance equation (Eq. (2.11)) along the droplet surface is solved using the Weighted Residuals method. Written in a spherical coordinate system, which is more convenient for the calculations.

$$\frac{1}{r^2\sin\theta}\left[\frac{(2r^2+r_\theta^2)\sin\theta}{\sqrt{r^2+r_\theta^2}}-\frac{d}{d\theta}\left(\frac{rr_\theta\sin\theta}{\sqrt{r^2+r_\theta^2}}\right)\right]=-K-Br\cos\theta-\frac{a}{\gamma}P_m \qquad (3.17)$$

where a is the radius of the undeformed sphere, r the non-dimensionalized radial coordinate, $K=aP_0/\gamma$, $B=\rho g a^2/\gamma$, and $P_m=-\varepsilon_0(n\cdot\nabla\Phi)^2/2$. The weighted residual method may be applied to solve Eq. (3.17) once the potential field distributions are known. The solution of Eq. (3.17) by the weighted residual method is constructed by integrating Eq. (3.17) with a weighting function ψ along the droplet surface,

$$\int_{\partial\Omega_1}\left\{\begin{array}{l}\dfrac{1}{r^2\sin\theta}\left[\dfrac{(2r^2+r_\theta^2)\sin\theta}{\sqrt{r^2+r_\theta^2}}-\dfrac{d}{d\theta}\left(\dfrac{rr_\theta\sin\theta}{\sqrt{r^2+r_\theta^2}}\right)\right]+\\ K+Br\cos\theta+\dfrac{a}{\gamma}P_m\end{array}\right\}\psi_i ds=0 \tag{3.18}$$

Where $r_\theta = dr/d\theta$. Integrating by parts, the weighted residuals approach leads to the following integral representation of the force equilibrium along the surface.

$$\int_0^\pi\left\{\begin{array}{l}\dfrac{rr_\theta\dfrac{d\psi_i}{d\theta}+\psi_i\left(2r^2+r_\theta^2\right)}{\sqrt{r^2+r_\theta^2}}+\\ r^2\psi_i\left(K+Br\cos\theta-\dfrac{a}{\gamma}P_m\right)\end{array}\right\}\sin\theta d\theta=0 \tag{3.19}$$

The variables r and r_θ are calculated by

$$r=\sum_{i=1}^{Ne}\psi_i r_i \quad \text{and} \quad r_\theta=\sum_{i=1}^{Ne}r_i\frac{d\psi_i}{d\zeta}\frac{d\zeta}{d\theta} \tag{3.20}$$

The constraints of the volume conservation and the center of the mass of the levitated sphere are needed to determine the shape and position of the droplet. In dimensionless form, the two constraints are expressed as

$$\frac{1}{a_d^3}\int_0^\pi r^3\sin\theta d\theta=2 \tag{3.21}$$

$$\frac{3}{8a_d^3}\int_0^{\pi} r^4 \cos\theta \sin\theta d\theta = z_c \tag{3.22}$$

where z_c is the center of mass. The free surface may be discretized into N elements and Eqs. (3.20-3.22) are integrated numerically. The results may be arranged in the following matrix form:

$$\mathbf{KX} = F \tag{3.23}$$

where

$$\mathbf{K} = \begin{bmatrix} a_{1,1} & a_{1,2} & & & & & b_1 & \\ a_{2,1} & a_{2,2} & a_{2,3} & & & & b_2 & \\ & \cdot & \cdot & \cdot & & & \cdot & \\ & & \cdot & \cdot & \cdot & & \cdot & \\ & & & a_{n-1,n-2} & a_{n-1,n-1} & a_{n-1,n} & b_{n-1} & \\ & & & & a_{n,n-1} & a_{n,n} & b_n & \\ b_1 & b_2 & \cdot & \cdot & b_{n-1} & b_n & & \\ c_1 & c_2 & \cdot & \cdot & c_{n-1} & c_n & & -1 \end{bmatrix} \quad \mathbf{X} = \begin{bmatrix} r_1 \\ r_2 \\ \cdot \\ \cdot \\ r_{n-1} \\ r_n \\ K \\ z_c \end{bmatrix} \quad F = \begin{bmatrix} F_1 \\ F_2 \\ \cdot \\ \cdot \\ F_{n-1} \\ F_n \\ 2 \\ 0 \end{bmatrix} \tag{3.24}$$

where $a_{i,j}$, b_j, c_j and F_j are calculated by

$$a_{i,j} = \int_{-1}^{1} \left\{ \begin{array}{l} \dfrac{\psi_i [2r\psi_j (\dfrac{d\theta}{d\xi})^2 + \dfrac{dr}{d\xi}\dfrac{d\psi_j}{d\xi}) + \psi_j \dfrac{d\psi_j}{d\xi}\dfrac{dr}{d\xi}}{\sqrt{(\dfrac{dr}{d\xi})^2 + (r\dfrac{d\theta}{d\xi})^2}} + \\ r\psi_i\psi_j \dfrac{aP_m}{\gamma} |\dfrac{d\theta}{d\xi}| \end{array} \right\} \sin\theta d\xi \tag{3.25}$$

$$b_i = \int_{-1}^{1} r^2 \psi_i \sin\theta |\frac{d\theta}{d\xi}| d\xi \tag{3.26}$$

$$c_j = \frac{3}{8}\int_{-1}^{1} r^3 \psi_j \cos\theta \sin\theta |\frac{d\theta}{d\xi}| d\xi \tag{3.27}$$

$$F_i = -\int_{-1}^{1} Br^3 \psi_i \cos\theta \sin\theta |\frac{d\theta}{d\xi}| d\xi \tag{3.28}$$

3.3 Computation of Thermal and Fluid Flow Fields

With the droplet shape known, the momentum and energy equations for the thermal and fluid flow fields along with the boundary conditions may be solved using the Galerkin finite element method. Both the transient and steady-state temperature and fluid flow fields are calculated in the present study.

3.3.1 Computation of thermal and fluid flow fields in a single-phrase droplet

In essence, the computational domain is first divided into small elements. With each element, the dependent variable **u**, P and T are interpolated by shape functions ϕ, ψ and θ,

$$\begin{aligned} \mathbf{u}^i(x,t) &= \phi^T \mathbf{U}^i(t) \\ P(x,t) &= \psi^T \mathbf{P}(t) \\ T(x,t) &= \theta^T \mathbf{T}(t) \end{aligned} \tag{3.29}$$

where the $\mathbf{U}^i$, $\mathbf{P}(t)$ and $\mathbf{T}$ are column vectors of element nodal point unknowns.

Substituting Eq. (3.29) into the governing Eqs. (2.2-2.4), we get the residuals R_1, R_2 and R_3 which represent the momentum, mass convection and energy equations respectively. The Galerkin form of the Method of Weighted Residuals seeks to reduce these errors to zero, and the shape functions are chosen the same as the weighting function. The governing equations for the fluid flow and heat transfer may be rewritten as

$$\left(\int_{\Omega_1} \psi(\hat{i}\cdot\nabla\phi^T)dV\right)U^i = -\varepsilon_p\left(\int_{\Omega_1}\psi\psi^T dV\right)P \tag{3.30}$$

$$\begin{aligned} &\left(\int_{\Omega_1}\rho\phi\phi^T dV\right)\frac{dU^i}{dt} + \left(\int_{\Omega_1}\rho\phi u\cdot\nabla\phi dV\right)U^i - \left(\int_{\Omega_1}(\hat{i}\cdot\nabla\phi)\psi^T dV\right)P \\ &+\left(\int_{\Omega_1}\eta(\nabla\phi\cdot\nabla\phi)dV\right)U^i + \left(\int_{\Omega_1}\eta(\hat{i}\cdot\nabla\phi)(\hat{j}\cdot\nabla\phi)dV\right)U^j = \\ &\int_{\partial\Omega_1} n\cdot\bar{\sigma}\cdot i\phi ds \end{aligned} \tag{3.31}$$

$$\begin{aligned} &\left(\int_{\Omega_1}\rho C_p\theta\theta^T dV\right)\frac{dT}{dt} + \left(\int_{\Omega_1}\rho C_p\theta u\cdot\nabla\theta^T dV\right)T + \\ &\left(\int_{\Omega_1} k\nabla\theta\cdot\nabla\theta^T dV\right)T = -\int_{\partial\Omega_1} q_T\theta ds \end{aligned} \tag{3.32}$$

Once the form of shape functions is specified, the integral defined in the above equations can be expressed by the matrix equation. The momentum and energy equations may be combined into a single global matrix equation,

$$\begin{bmatrix} \mathbf{M} & 0 & 0 \\ 0 & 0 & 0 \\ 0 & 0 & \mathbf{N}_T \end{bmatrix} \begin{bmatrix} \dot{\mathbf{U}} \\ \dot{\mathbf{P}} \\ \dot{\mathbf{T}} \end{bmatrix} + \begin{bmatrix} \mathbf{A(U)}+\mathbf{K} & -\mathbf{C} & \mathbf{B} \\ -\mathbf{C}^{\mathbf{T}} & 0 & 0 \\ 0 & 0 & \mathbf{D}_T\mathbf{(U)}+\mathbf{L}_T \end{bmatrix} \begin{bmatrix} \mathbf{U} \\ \mathbf{P} \\ \mathbf{T} \end{bmatrix} = \begin{bmatrix} \mathbf{F} \\ 0 \\ \mathbf{G}_T \end{bmatrix} \tag{3.33}$$

The coefficient matrices above are defined by

$$\mathbf{M}_p = \int_{\Omega_1} \psi\psi^T dV \; ; \qquad \mathbf{N}_T = \int_{\Omega_1} \rho C_p \theta\theta^T dV$$

$$\mathbf{M} = \int_{\Omega_1} \phi\phi^T dV \; ; \qquad \mathbf{C}_j = \int_{\Omega_1} \hat{j} \cdot \nabla\phi\psi^T dV$$

$$\mathbf{L}_T = \int_{\Omega_1} k\nabla\theta \bullet \nabla\theta^T dV \; ; \qquad \mathbf{A(U)} = \int_{\Omega_1} \rho\phi\, \mathbf{u} \cdot \nabla\phi^T dV$$

$$\mathbf{D}_T\mathbf{(U)} = \int_{\Omega_1} \rho C_p \theta\, \mathbf{u} \bullet \nabla\theta^T dV \; ; \qquad \mathbf{B} = \int_{\partial\Omega_1} \frac{\partial\gamma}{\partial T} \mathbf{t} \cdot \nabla\theta^T dS$$

$$\mathbf{G}_T = -\int_{\partial\Omega_1} q_T \theta \, ds \; ; \qquad \mathbf{F} = \int_{\partial\Omega_1} \phi\tau \cdot \mathbf{n} \, ds$$

$$\mathbf{K}_{ij} = (\int_{\Omega_1} \eta\nabla\phi \cdot \nabla\phi^T dV)\delta_{ij} + \int_{\Omega_1} \eta(\hat{i} \cdot \nabla\phi)(\hat{j} \cdot \nabla\phi^T) dV$$

where j=1, 2, 3. Note also that matrix B represents the surface tension effects on the fluid motion. The assembled global matrix equations are stored in the skyline form and solved using the Gaussian elimination method. The transient term is set to zero for steady-state calculations, however.

3.3.2 Computation of thermal and fluid flow fields in a droplet of immiscible liquid metals

The computation of thermal and fluid flow fields in the droplet of immiscible liquid metals is very similar to that in the single-phrase droplet in section 3.3.1 except that the calculation is carried out in two kinds of immiscible liquid metals. It is also necessary to take account the effect of the surface tension on the surface between the immiscible liquid metals, as presented by Eqs. (2.30-2.33). With each dependent variable **u**, P and T in elements interpolated by the shape functions, ϕ, ψ and θ, The matrix form of the finite element discretized equations for the thermal and fluid flow model may be written as follows,

$$\begin{bmatrix} \mathbf{M} & \mathbf{0} & \mathbf{0} \\ \mathbf{0} & \mathbf{0} & \mathbf{0} \\ \mathbf{0} & \mathbf{0} & \mathbf{N}_T \end{bmatrix} \begin{bmatrix} \dot{\mathbf{U}} \\ \dot{\mathbf{P}} \\ \dot{\mathbf{T}} \end{bmatrix} + \begin{bmatrix} \mathbf{A(U)+K} & \mathbf{-C} & \mathbf{0} \\ \mathbf{-C^T} & \mathbf{0} & \mathbf{0} \\ \mathbf{0} & \mathbf{0} & \mathbf{D}_T\mathbf{(U)+L}_T \end{bmatrix} \begin{bmatrix} \mathbf{U} \\ \mathbf{P} \\ \mathbf{T} \end{bmatrix} = \begin{bmatrix} \mathbf{F} \\ \mathbf{0} \\ \mathbf{G}_T \end{bmatrix} \tag{3.34}$$

The coefficient matrices above are defined by

$$\mathbf{M} = \int_{\Omega_m} \phi\phi^T dV \; ; \qquad \mathbf{N}_T = \int_{\Omega_m} \rho C_p \theta\theta^T dV$$

$$\mathbf{L}_T = \int_{\Omega_m} k\nabla\theta \cdot \nabla\theta^T dV \; ; \qquad \mathbf{A(U)} = \int_{\Omega_m} \rho\phi\, \mathbf{u}_m \cdot \nabla\phi^T dV$$

$$\mathbf{D}_T\mathbf{(U)} = \int_{\Omega_m} \rho C_p \theta\, \mathbf{u}_k \cdot \nabla\theta^T dV \; ; \qquad \mathbf{G}_T = -\int_{\partial\Omega_1 \cap \partial\Omega_2} q_T \theta\, ds \; ;$$

$$\mathbf{C}_j = \int_{\Omega_m} \hat{j} \cdot \nabla\phi\psi^T dV$$

$$\mathbf{F}_j = \int_{\partial\Omega_1 \cap \partial\Omega_2} \hat{j} \cdot \overline{\sigma}_1 \cdot \mathbf{n}\, \phi ds + \int_{\partial\Omega_1 \cap \partial\Omega_3} \hat{j} \cdot (\overline{\sigma}_3 - \overline{\sigma}_1) \cdot \mathbf{n}\, \phi\, ds$$

$$\mathbf{K}_{ij} = (\int_{\Omega_m} \eta \nabla\phi \cdot \nabla\phi^T dV)\,\delta_{ij} + \int_{\Omega_m} \eta(\hat{i} \cdot \nabla\phi)(\hat{j} \cdot \nabla\phi^T)\, dV$$

where *m*=1, 3. The assembled global matrix equations are stored in the skyline form and solved using the Gaussian elimination method [Huo, 2004a]. The transient term is set to zero for steady-state calculations, however.

3.3.3 Computation of mass transfer into a single-phrase droplet

With the thermal and fluid flow fields known, the equation governing the mass transfer (Eq. (2.15)) is solved for the transient concentration distribution in the droplet [Huo, 2005a]. By the Galerkin finite element method, the variable *C* is interpolated by shape function ξ,

$$C(x,t) = \xi^T \mathbf{C}(t) \tag{3.35}$$

where the **C**(t) is column vectors of element nodal point unknowns. The matrix form of the finite element discretized equation for the concentration field may be written as follows,

$$\mathbf{N}_C \dot{C} + (\mathbf{D}_C(\mathbf{U}) + \mathbf{L}_C)\, C = 0 \tag{3.36}$$

The coefficient matrices above are defined by

$$\mathbf{N}_C = \int_{\Omega_1} \xi\xi^T dV \; ; \quad \mathbf{D}_C(\mathbf{U}) = \int_{\Omega_1} \xi\, \mathbf{u}\cdot\nabla\xi^T dV \; ; \quad \mathbf{L}_C = \int_{\Omega_1} \varphi_{AB}\nabla\xi\cdot\nabla\xi^T dV$$

Like the thermal and fluid flow calculations, the assembled global matrix equations are stored in the skyline form and solved using the Gaussian elimination method [Huo, 2005a]. For this study, the implicit scheme is used to carry out the time matching calculations.

3.3.4 Computational aspects in the thermal and fluid flow calculations

Modeling of 3-D surface tension driven flows on a curvilinear surface within the framework of finite elements requires some tedious geometric treatment that involves differential geometry operations and rotation of matrix in local coordinates at the surface for the purpose of appropriately imposing velocity and surface stress boundary conditions (Eqs.(2.10) and (2.12)). While treatment may vary depending on specific problems, our approach to model the surface driven flow makes use of local surface coordinates and of sharp edges with specified local coordinate system as well as consistent surface normals. With reference to Fig. 3.1, a local coordinate system (η,ζ,n) is defined at a point on the surface. Note that during calculations this local system may be (although not required) chosen conveniently such that they are coincident with the normalized coordinate systems for isoparemetric calculations at the element level. The xyz and $\eta\zeta$n coordinate systems are related by the following coordinate transformation,

$$\begin{pmatrix} \dfrac{\partial}{\partial \eta} \\ \dfrac{\partial}{\partial \zeta} \\ \dfrac{\partial}{\partial n} \end{pmatrix} = [J] \begin{pmatrix} \dfrac{\partial}{\partial x} \\ \dfrac{\partial}{\partial y} \\ \dfrac{\partial}{\partial z} \end{pmatrix} = \begin{bmatrix} x_{,\eta} & y_{,\eta} & z_{,\eta} \\ x_{,\zeta} & y_{,\zeta} & z_{,\zeta} \\ x_{,n} & y_{,n} & z_{,n} \end{bmatrix} \begin{pmatrix} \dfrac{\partial}{\partial x} \\ \dfrac{\partial}{\partial y} \\ \dfrac{\partial}{\partial z} \end{pmatrix} \tag{3.37}$$

In constructing the Jacobian matrix, use has been made of the following differential geometry relations,

$$\mathbf{r}_1 = x_{,\eta}\,\hat{i} + y_{,\eta}\,\hat{j} + z_{,\eta}\,\hat{k}, \qquad \mathbf{r}_2 = x_{,\zeta}\,\hat{i} + y_{,\zeta}\,\hat{j} + z_{,\zeta}\,\hat{k}$$

$$\mathbf{r}_n = \mathbf{r}_1 \times \mathbf{r}_2 = x_{,n}\,\hat{i} + y_{,n}\,\hat{j} + z_{,n}\,\hat{k} = \left(y_{,\eta}z_{,\zeta} - z_{,\eta}y_{,\zeta}\right)\hat{i} - \left(x_{,\eta}z_{,\zeta} - z_{,\eta}x_{,\zeta}\right)\hat{j} + \left(x_{,\eta}y_{,\zeta} - y_{,\eta}x_{,\zeta}\right)\hat{k}$$

The Jacobian matrix may be inverted analytically with the follow result,

$$[J]^{-1} = \frac{1}{|J|}\begin{bmatrix} y_{,\zeta}z_{,n} - z_{,\zeta}y_{,n} & -(y_{,\eta}z_{,n} - z_{,\eta}y_{,n}) & y_{,\eta}z_{,\zeta} - z_{,\eta}y_{,\zeta} \\ -(x_{,\zeta}z_{,n} - z_{,\zeta}x_{,n}) & x_{,\eta}z_{,n} - z_{,\eta}x_{,n} & x_{,\eta}z_{,\zeta} - z_{,\eta}x_{,\zeta} \\ x_{,\zeta}y_{,n} - y_{,\zeta}x_{,n} & -(x_{,\eta}y_{,n} - y_{,\eta}x_{,n}) & x_{,\eta}y_{,\zeta} - y_{,\eta}x_{,\zeta} \end{bmatrix} \tag{3.38}$$

Furthermore, a shape (or any) function $f(\eta,\zeta)$ defined over the surface is a function of (η,ζ) only and hence $\partial f(\eta,\zeta)/\partial n = 0$. With these relations, one may then relate the volume differential operator to the surface operator,

$$\begin{pmatrix} \frac{\partial}{\partial x} \\ \frac{\partial}{\partial y} \\ \frac{\partial}{\partial z} \end{pmatrix} = [J]^{-1} \begin{pmatrix} \frac{\partial}{\partial \eta} \\ \frac{\partial}{\partial \zeta} \\ \frac{\partial}{\partial n} \end{pmatrix} \tag{3.39}$$

which may be written in the terminology of differential geometry [Weatherburn, 1930],

$$\nabla = \frac{\partial}{\partial x}\hat{i} + \frac{\partial}{\partial x}\hat{j} + \frac{\partial}{\partial x}\hat{k} = \frac{1}{H^2}\mathbf{r}_1\left(G\frac{\partial}{\partial \eta} - F\frac{\partial}{\partial \zeta}\right) + \frac{1}{H^2}\mathbf{r}_1\left(E\frac{\partial}{\partial \zeta} - F\frac{\partial}{\partial \eta}\right) \tag{3.40}$$

with $E = \mathbf{r}_1^2 = x_{,\eta}^2 + y_{,\eta}^2 + z_{,\eta}^2$, $G = \mathbf{r}_2^2 = x_{,\zeta}^2 + y_{,\zeta}^2 + z_{,\zeta}^2$, $F = \mathbf{r}_1 \cdot \mathbf{r}_2 = x_{,\eta}x_{,\zeta} + y_{,\eta}y_{,\zeta} + z_{,\eta}z_{,\zeta}$ and $H^2 = EG - F^2$. It is stressed that in Eq. (3.40), (ζ, η) is not necessarily orthogonal so long as they are not collinear. This is important in that irregular quadrilateral surface elements can be readily handled in 3-D finite element calculations presented here.

To perform the calculations, the consistent normal of the surface at node i is required, which must satisfy the continuity equation [Engelman, 1982],

$$n_x^i = \frac{1}{n_i}\int_{\Omega_1} \frac{\partial \phi_i}{\partial x} dV \,,\; n_y^i = \frac{1}{n_i}\int_{\Omega_1} \frac{\partial \phi_i}{\partial y} dV \,,\; n_z^i = \frac{1}{n_i}\int_{\Omega_1} \frac{\partial \phi_i}{\partial z} dV \tag{3.41}$$

where

$$n_i = \left[\left(\int_{\Omega_1} \frac{\partial \phi_i}{\partial x} dV\right)^2 + \left(\int_{\Omega_1} \frac{\partial \phi_i}{\partial y} dV\right)^2 + \left(\int_{\Omega_1} \frac{\partial \phi_i}{\partial z}\right)^2\right]$$

Note that the integration is carried over all the elements sharing node i. Once the normal is known, the two tangential directions $\mathbf{t}_1=(t_x^1,t_y^1,t_z^1)$ and $\mathbf{t}_2=(t_x^2,t_y^2,t_z^2)$ can be easily calculated using the cross product relations, $\mathbf{t}_1=\mathbf{b}\times\mathbf{n}$, which **b** is an arbitrary space vector such that $\mathbf{b}\times\mathbf{n}\neq\mathbf{0}$, and $\mathbf{t}_2=\mathbf{n}\times\mathbf{b}$. This ensures that the local coordinate system defined by $\mathbf{t}_1\times\mathbf{t}_2\times\mathbf{n}$ forms an orthogonal triplet at any node (e.g. node i), a strict condition different from that imposed on (η,ζ,n). The velocities defined in the $\mathbf{t}_1\times\mathbf{t}_2\times\mathbf{n}$ system is now related to those in the xyz system through the following transformation,

$$\begin{pmatrix} U_{t2} \\ U_{t1} \\ U_n \end{pmatrix} = \begin{bmatrix} t_x^1 & t_y^1 & t_z^1 \\ t_x^2 & t_y^2 & t_z^2 \\ n_x & n_y & n_z \end{bmatrix} \begin{pmatrix} U_x \\ U_y \\ U_z \end{pmatrix} \tag{3.42}$$

Note that the above transformation also applies to force vectors.

To calculate the surface tension contributions, the integration of ∇ term is first calculated using the relation (Eq. (3.40)), followed by the above relation to transform the velocities defined in the xyz coordinates to those in the $\mathbf{t}_1\times\mathbf{t}_2\times\mathbf{n}$ system. For the flows under consideration, the normal component of the velocity is zero and the condition can be imposed after the transformation. On the sharp edges formed by the intersection of two surfaces, however, the $\mathbf{t}_1\times\mathbf{t}_2\times\mathbf{n}$ system is not uniquely defined by the above computational procedure. This causes difficulty when appropriate velocity and stress boundary conditions are specified along the edge. To overcome the problem, the normal of the edge is taken to be that associated with one of the two joining surfaces and an additional constraint is imposed such that the $\mathbf{t}_1$ is along the edge.

The above treatment in general will give rise to the submatrix **B**, which, when assembled following standard procedure [Huo, 2004a], results in a significant number of unfills in the final global finite element matrix. These unfills may be occupied during LU decomposition and therefore drastically slow down the computations [Duff, 1996]. To reduce these unfills associated with 3-D Marangoni flow computations, the finite element matrix is desectioned such that the terms associated with **B** matrix is moved to the right-hand side. As such the matrix $\mathbf{D}_T+\mathbf{A}_L(\mathbf{U})$ may be solved independent of the matrix describing the flow and velocity. Further, making use of the penalty formulation to treat the pressure term eliminates the pressure field. This re-shuffling of the final global matrix elements and unknowns results in savings in both storage space and CPU time required for simulations. Numerical tests show that approximately a factor of 2 to 4 savings in computational time is achieved in the present study, depending on the number of finite elements used.

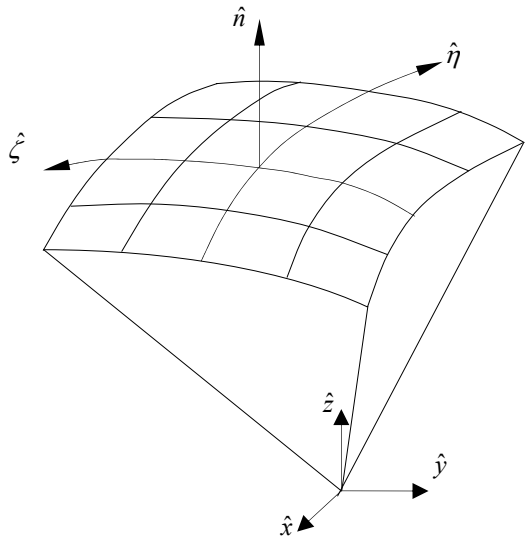

Figure 3.1 Transformation between local curvilinear and global Cartesian coordinate systems

3.4 Computation of the Stability of the Droplet in the Magnetic Fields

The 3-D electromagnetic field may be solved using the edge finite element method [Huo, 2004c, 2005b]. The edge-based elements are necessary to satisfy the divergence-free constraint, $\nabla \cdot \mathbf{E}=0$ [Johns, 1971]. However, the huge sparse matrix produced by the FEM appears to be a major setback to finding an efficient numerical solution to a large scale problem. Our experience shows that this remains true even with various efficient solvers designed specifically for the solution of a large sparse system of linear algebraic equations to improve the computational efficiency. To alleviate the disadvantage of the finite element method, a hybrid finite element-boundary method is employed instead. Using this approach, finite elements are used in the conducting droplet where power density is needed and material properties may be a function of temperature, while boundary elements are used elsewhere. The FEM and the BEM are coupled through the interface boundary conditions. This idea is shown in Figure 3.2

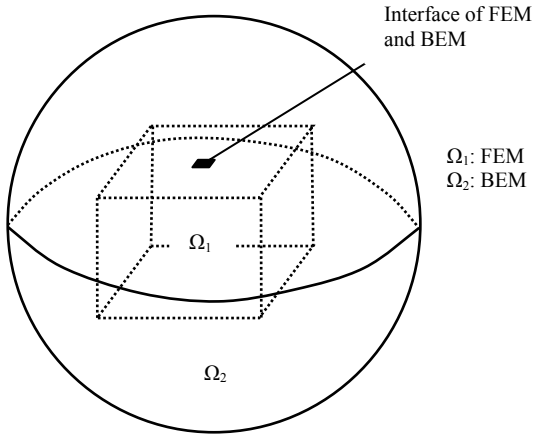

Figure 3.2 Schematic representation of the coupling of the finite element and boundary element

3.4.1 Finite element formulation

To develop a finite element formulation in the conducting droplet, the wave equation (2.51) is integrated with respect to a vector testing function $\delta\mathbf{E}$ [Akarapu, accepted].

$$\iiint_V \delta\mathbf{E} \cdot \left(\nabla \times \frac{1}{\mu_r} \nabla \times \mathbf{E} - \omega^2 \mu \varepsilon_c \mathbf{E} \right) dV = -\iiint_V j\omega\mu \mathbf{J}_i \cdot \delta\mathbf{E} dV \tag{3.43}$$

Integration by parts gives rise to the surface integral term,

$$\begin{aligned} \iiint_V \frac{1}{\mu_r} \nabla \times \mathbf{E} \cdot \nabla \times \delta\mathbf{E}\, dV - \iiint_V \omega^2 \mu \varepsilon_c \delta\mathbf{E} \cdot \mathbf{E}\, dV = \\ \oiint_S \frac{1}{\mu_r} (\delta\mathbf{E} \times \nabla \times \mathbf{E}) \cdot \mathbf{n}\, dS - \iiint_V j\omega\mu \delta\mathbf{E} \cdot \mathbf{J}_i dV \end{aligned} \tag{3.44}$$

Making use of the vector identity

$$(\delta\mathbf{E} \times \nabla \times \mathbf{E}) \cdot \hat{\mathbf{n}} = -(\hat{\mathbf{n}} \times \nabla \times \mathbf{E}) \cdot \delta\mathbf{E} \tag{3.45}$$

and also the boundary conditions, the final integral formulation is obtained,

$$\iiint_V \left(\frac{1}{\mu_r} \nabla \times \mathbf{E} \cdot \nabla \times \delta\mathbf{E} - \omega^2 \mu \varepsilon_c \delta\mathbf{E} \cdot \mathbf{E} \right) dV = - \oiint_S [\delta\mathbf{E} \cdot \mathbf{U}] dS - \iiint_V j\omega\mu\delta\mathbf{E} \cdot \mathbf{J}_i dV \tag{3.46}$$

With appropriate finite element discretization and necessary elemental calculations followed by assembly, one has the matrix representation of equation (3.46),

$$\mathbf{[K]\{E\} + [B]\{U\} = \{F\}} \tag{3.47}$$

where the matrix elements are calculated using the following expressions,

$$K_{ij} = \iiint_V \left(\frac{1}{\mu_r} \nabla \times \mathbf{N}_i \cdot \nabla \times \mathbf{N}_j - \omega^2 \mu \varepsilon_c \mathbf{N}_i \cdot \mathbf{N}_j \right) dV$$

$$B_{ij} = \oiint_S \mathbf{N}_i \cdot \mathbf{S}_j \, dS$$

$$F_i = -\iiint_V j\varpi\mu \mathbf{N_i} \cdot \mathbf{J_i} dV$$

Note that here $\mathbf{N}_i$ and $\mathbf{S}_i$ are edge-based vector shape functions and their derivatives.

3.4.2 Boundary element formulation using the dyadic Green function

The basic idea of the hybrid FE/BE method was first introduced for the study of electromagnetics by Silvester and Hsieh (1971) and McDonald and Wexler (1972) for solving exterior or unbounded field problems. Later, the method was applied to solve

two- and three-dimensional antenna and scattering problems. Here, it is applied to solve the electromagnetic field in a microwave system, and the formulation is based on Green's theorem involving the dyadic Green function,

$$\begin{aligned}\iiint_V \left(\mathbf{E}\cdot\nabla\times\nabla\times\overline{\overline{G}} - \overline{\overline{G}}\cdot\nabla\times\nabla\times\mathbf{E}\right)dV \\ = \oiint_S \left(\overline{\overline{G}}\times\nabla\times\mathbf{E} - \mathbf{E}\times\nabla\times\overline{\overline{G}}\right)\cdot\hat{\mathbf{n}}\,dS \\ = \oiint_S \left((\hat{\mathbf{n}}\times\mathbf{E})\cdot\nabla\times\overline{\overline{G}} + (\hat{\mathbf{n}}\times\nabla\times\mathbf{E})\cdot\overline{\overline{G}}\right)dS\end{aligned} \tag{3.48}$$

Now, substituting into the above equation the following wave equations and the equations for the dyadic Green function,

$$\nabla\times\nabla\times\mathbf{E} - k_0^2\mathbf{E} = -j\omega\mu\mathbf{J}_i \tag{3.49}$$

$$\nabla\times\nabla\times\overline{\overline{G}} - k_0^2\overline{\overline{G}} = \bar{\bar{I}}\delta(\mathbf{r}-\mathbf{r}') \tag{3.50}$$

and carrying out the necessary integration, we can get,

$$\begin{aligned}\mathbf{E}(\mathbf{r}) = -jk_0Z_0\iiint_V \mathbf{J}(\mathbf{r}')\cdot\overline{\overline{G}}_0(\mathbf{r},\mathbf{r}')dV' - \\ \oiint_S\{[\hat{\mathbf{n}}'\times\mathbf{E}(\mathbf{r}')]\cdot[\nabla'\times\overline{\overline{G}}_0(\mathbf{r},\mathbf{r}')] + \\ [\hat{\mathbf{n}}'\times\nabla'\times\mathbf{E}(\mathbf{r}')]\cdot\overline{\overline{G}}_0(\mathbf{r},\mathbf{r}')\}dS'\end{aligned} \tag{3.51}$$

The surface's unit normal direction points outward from the region Ω_2. In equation (3.51) the first term on the right-hand side is the field radiated by **J** in the free-space environment, thus denoted as $\mathbf{E}_{inc}$. With the following relation,

$$\nabla' \times \overline{\overline{G}} = \nabla' G_0(\mathbf{r},\mathbf{r}') \times \bar{\bar{I}} \tag{3.52}$$

and the surface divergence theorem, equation(3.51) can be further simplified as

$$\begin{aligned}\mathbf{E}(\mathbf{r}) &= \mathbf{E}_{inc}(\mathbf{r}) - \\ &\oiint_S \left(\hat{\mathbf{n}}'\times\mathbf{E}(\mathbf{r}')\times\nabla' G(\mathbf{r},\mathbf{r}') + \left(\hat{\mathbf{n}}'\times\nabla'\times\mathbf{E}(\mathbf{r}')\right)G(\mathbf{r},\mathbf{r}')\right)dS(\mathbf{r}') \\ &-\frac{1}{k_0^2}\oiint_S \nabla G(\mathbf{r},\mathbf{r}')\nabla'\cdot\left(\hat{\mathbf{n}}'\times\nabla\times\mathbf{E}(\mathbf{r}')\right)dS(\mathbf{r}')\end{aligned} \tag{3.53}$$

Taking the cross product of equation (3.53) with surface normal $\hat{\mathbf{n}}$ yields

$$\begin{aligned}\hat{\mathbf{n}}\times\mathbf{E}(\mathbf{r}) &= \hat{\mathbf{n}}\times\mathbf{E}_{inc}(\mathbf{r}) - \\ &\hat{\mathbf{n}}\times\oiint_S \left(\hat{\mathbf{n}}'\times\mathbf{E}(\mathbf{r}')\times\nabla' G(\mathbf{r},\mathbf{r}') + \left(\hat{\mathbf{n}}'\times\nabla'\times\mathbf{E}(\mathbf{r}')\right)G(\mathbf{r},\mathbf{r}')\right)dS(\mathbf{r}') \\ &-\frac{1}{k^2}\hat{\mathbf{n}}\times\oiint_S \nabla G(\mathbf{r},\mathbf{r}')\nabla'\cdot\left(\hat{\mathbf{n}}'\times\nabla\times\mathbf{E}(\mathbf{r}')\right)dS(\mathbf{r}')\end{aligned} \tag{3.54}$$

After the BE discretization using edge boundary elements, followed by calculations at the element level, equation (3.54) may be represented in the following matrix form,

$$[\mathbf{B^{ss}}]\{\mathbf{E^s}\} = \{\mathbf{b^s}\} - \sum_{\mathbf{t}}^{\mathbf{M_t}} [\mathbf{P^{st}}]\{\mathbf{E^t}\} - \sum_{\mathbf{t}}^{\mathbf{M_t}} [\mathbf{Q^{st}}][\{\mathbf{U^t}\} \tag{3.55}$$

where the matrix elements are calculated by

$$\left[\mathbf{B^{ss}}\right] = -\iint_{S^s} \{\mathbf{N}^s\} \cdot \{\mathbf{S}^s\}^T \, dS(\mathbf{r})$$

$$\{\mathbf{b^s}\} = \iint_{S^s} \{\mathbf{S}^s\} \cdot \mathbf{E}_{inc}(\mathbf{r}) \, dS(\mathbf{r})$$

$$\left[\mathbf{P^{st}}\right] = \iint_{S^s} \left\{ \{\mathbf{S}^s\} \cdot \iint_{S^t} \{\mathbf{S}^t\}^T \times \nabla' G(\mathbf{r}, \mathbf{r}') dS(\mathbf{r}') \right\} dS(\mathbf{r})$$

$$\left[\mathbf{Q^{st}}\right] = \iint_{S^s} \left\{ \{\mathbf{S}^s\} \cdot \iint_{S^t} \{\mathbf{S}^t\}^T G(\mathbf{r}, \mathbf{r}') dS(\mathbf{r}') \right\} dS(\mathbf{r})$$

$$- k^{-2} \iint_{S^s} \left\{ (\nabla \cdot \mathbf{S}^s) \iint_{S^t} \nabla' \cdot \{\mathbf{S}^t\}^T G(\mathbf{r}, \mathbf{r}') dS(\mathbf{r}') \right\} dS(\mathbf{r})$$

With some matrix algebra, equation (3.55) is written more conveniently in the following form,

$$[\mathbf{B}_2]\{\mathbf{U}_2\} = \{\mathbf{F}_2\} + [\mathbf{K}_2]\{\mathbf{E}_2\} \tag{3.56}$$

where $\mathbf{B}_2$ is the boundary element matrix associated with the unknowns.

3.4.3 Coupling of boundary and finite elements

The boundary and finite element formulations for the solution of electric field distribution are coupled through the interface conditions along the boundary of Ω_1 and the boundary of Ω_2,

$$\frac{1}{\mu_{r1}}\hat{\mathbf{n}}\times\nabla\times\mathbf{E}_1=\frac{1}{\mu_{r2}}\hat{\mathbf{n}}\times\nabla\times\mathbf{E}_2 \tag{3.57}$$

$$\hat{\mathbf{n}}\times\mathbf{E}_1=\hat{\mathbf{n}}\times\mathbf{E}_2 \tag{3.58}$$

There are two ways to obtain a coupled solution of equations (3.47) and (3.56) with the use of the above interface conditions. One way is to use direct coupling, by which the entire boundary element region is treated as a macro element, and the boundary element global matrix is then incorporated into equation (3.47). This approach works efficiently for 2-D and moderately sized 3-D problems [Li, in print]. However, it becomes inefficient for large 3-D problems such as the one under consideration because it substantially increases the resultant edge finite element matrix bandwidth and hence the CPU times. Another approach is iterative [Huo, 2004c, 2005b]. By this approach, equation (3.56) is solved for $\{\mathbf{U}_2\}$ with an assumed $\{\mathbf{E}_2\}$ on the interface. The standard LU-decomposition for complex matrix can be used for the solution. Then $\{\mathbf{E}_1\}$ is solved using equation (3.47) with known $\{\mathbf{U}_2\}$. The convergence on $|\{\mathbf{E}_2\}-\{\mathbf{E}_1\}|<\varepsilon$, where ε is the convergence criterion, is checked. If convergence is not achieved, $\{\mathbf{E}_2\}=\{\mathbf{E}_1\}$ along the interface is used to predict an updated $\{\mathbf{U}_2\}$ using equation (19) and then $\{\mathbf{E}_1\}$ is updated using equation (3.47). The process is repeated until the convergence is achieved.

It is worth noting here that for either of the two approaches, the matrix $\mathbf{B}_2$ requires an LU-decomposition only once and the decomposed matrices are stored in the memory for subsequent back substitutions when needed. In the case of the iterative procedure, this means that subsequent iteration between FE and BE requires only a back substitution procedure, thereby leading to a significant increase in computational speed.

3.5 Computation of the Oscillation of the Droplets in the Electrostatic Levitation Mechanism

For the oscillation calculations, the electric and droplet deformation calculations must be coupled with the fluid calculations. To incorporate the free surface boundary condition, the front track technique is applied. Thus applying the weighted residuals method to Eq. (2.37) results in the following matrix equations for the free surface boundary coordinates,

$$\mathbf{M}\dot{\mathbf{X}} + \mathbf{K}\mathbf{X} = \mathbf{0} \tag{3.59}$$

Because the nodes are allowed to move, these movements must be superimposed on the velocity at the nodal points and therefore the convection term in Eq. (2.3) must be modified accordingly, that is, $\rho\mathbf{u}\cdot\nabla\mathbf{u}$ is replaced by $\rho(\mathbf{v}+\mathbf{u})\cdot\nabla\mathbf{u}$ where $\mathbf{v}$ is the nodal velocity due to the free surface movement.

The oscillation calculations are solved iteratively with the time differentials approximated by the implicit time differencing scheme. The iteration for the problem starts the computation of the electric potential with an initial guess for the free surface,

then calculates fluid flow field, and then calculates the updated free surface boundary. The updated boundary is used to start another set of calculation for the updated vector potential and iteration continues till all the variables converge within a preset tolerance.

CHAPTER 4

3-D SIMULATION OF THE FREE SURFACE DEFORMATION AND THERMAL CONVECTION IN THE ELECTROSTATICALLY LEVITATED, SINGLE-PHRASE DROPLET

4.1 Introduction

In this chapter, a numerical study of steady state and transient 3-D Marangoni convection and heat transfer in electrostatically levitated droplets. The analysis is based on the Galerkin finite element solution of the Navier-Stokes and energy equations. Numerical aspects for the computation of surface driven flows in general curvilinear coordinate system are discussed within the framework of finite elements and differential geometry. Results show that for practical microgravity conditions under which the deformation is small, the single and double beam heating arrangements, when placed at the poles or equator plane, produce an approximately axisymmetric flow profile and temperature distribution with the axis of symmetry defined by the line passing through the centers of the laser beam and the droplet. Thus, an axisymmetric model could provide a reasonably good description, and an exact one when the laser beam is placed at a pole or one beam is placed at both poles. When a tetrahedral or octahedral heating arrangement is applied, complex 3-D flow structures occur, which result from interaction of flow motions associated with each laser beam. For the case studied, the tetrahedral heating arrangement does not seem to produce a significant reduction in internal velocity, in contrast to perception, but the temperature is more uniform. This phenomenon is explained by the

fact that the 2-beam and 4-beam arrangements result in a surface temperature gradient of approximately the same magnitude. The six-beam heating placement produces, however, a much more significant reduction in both velocity and temperature non-uniformity. The transient decaying during cooling is characterized by the evolution of both temperature and velocity fields evolve in a rather complex fashion, with the initial stage dominated by the pronounced thermal and flow mixing on the surface layer of a droplet. The strong surface mixing quickly brings out a surface temperature distribution of axisymmetry, while a 3-D structure still prevails inside until much later. The flow reversal is also observed in the droplets that have been heated by 4- or 6-beam lasers during the decay, and there is a spike in velocity and temperature at the time when the flow reversal occurs.

4.2 Result and discussion

The computational models described in chapter 3 may be employed to predict the electric field distribution, electric pressure distribution along the surface of a droplet, droplet shapes, transient full-3D temperature distribution and internal convection in the droplets driven by surface tension force. Extensive numerical simulations have been carried out for various heating conditions. A selection of computed results is given below. The thermophysical properties used for calculations are tabulated in Table 4.1. The criterion for the convergence of nonlinear iteration is set to 1×10^{-4} (norm-2 relative error).

Parameters	Values
T_{melt} (K)	1940
Q_0 (W/m^2)	1.3×10^6
a_d (mm)	2.5
ρ (kg/m^3)	4110
μ (kg/m-s)	$5.2\ x10^{-3}$
γ (N/m)	0.864
$d\gamma/dT$(N/m-K)	$-2.6\ x10^{-4}$
K (W/m-K)	21.6
C_P (J/kg-K)	700
E (V/m)	$3.3\ x10^6$
Emisivity ε_0	0.3
β (K^{-1})	$6.5\ x10^{-6}$
Pr	$1.685\ x10^{-1}$
a_l (mm)	2.05

Table 4.1 Parameters used in calculations of the thermal and fluid flow

4.2.1 Mesh selection and mesh independency test

Numerical tests show a total of 48 linear boundary elements were adequate for the electric field calculations and 24 quadratic boundary elements for the computation of free surface deformations. The thermal and fluid flow calculations used 8-node hexahedral elements. Special treatment is made to generate the hexahedral elements neat the pole. Mesh independence tests for flow and thermal simulations were conducted such that the numerical error in two consecutive mesh refinements is smaller than 0.1% in maximum velocities calculated. From these tests, a mesh of 2900 8-node elements was used for an octant model for the results presented below, which is used to simulate 2 laser beams and four laser beams, while that of 3680 8-node elements for a one-third model, to take

advantage of symmetry associated with the heating arrangement. Other meshes were also used and tested for mesh independence for other laser heating conditions. Some typical meshes used for 3-D thermal and fluid flow calculations are shown in Figure 4.2. Mesh for 2-D droplet deformation is given in Figure 4.1.

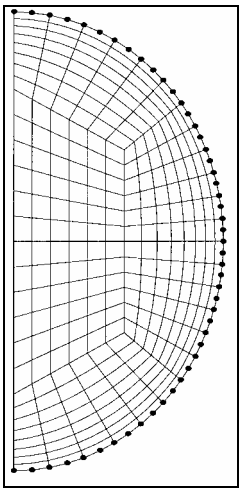

Figure 4.1 Boundary element mesh of calculating deformation

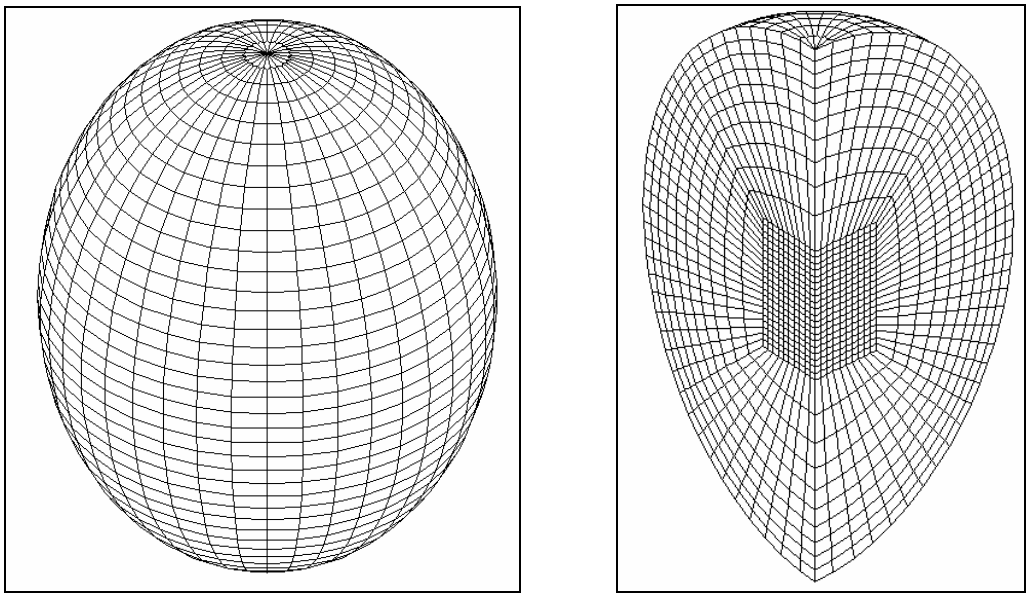

Figure 4.2 Finite element meshes for 3-D computations

4.2.2 Droplet deformation

For a majority of microgravity experiments, the droplet deformation is determined primarily by the balance of the surface tension and electric stresses along the surface, and the contribution of the hydrodynamic and viscous stresses is negligible, typically on the order of 1% [Song, 2000b, 2001]. Thus, for these cases, the computation of the droplet deformation can be decoupled from the fluid flow calculations. Also, experiments show that under normal conditions considered for space applications, the droplet deformation is axisymmetric.

In microgravity, the electric forces are designed to position the droplet in a designated location. As a net lifting force is not needed, the total net charge is equal to zero. However, as the droplet is placed in the electric field, the perturbed field induces surface charges on the droplet. These induced surface charges interact with the imposed electric field to ensure that the electric field inside the droplet is zero and that the entire droplet is kept at a constant potential. While the net force is zero, the local electric force along the surface is not, which must be balanced by the surface tension force, thereby defining the free surface profile for the droplet. Figure 4.3 shows the result of surface deformation obtained from the hybrid finite/boundary model. Because the surface charges are negative on the lower half surface and positive on the upper half surface, they combine with an upward electric field to produce a force that pulls the surface outward from the center. Moreover, the surface charges are symmetrically distributed due to the symmetry of the applied electric field, which causes the droplet to deform symmetrically.

To satisfy the mass conservation, the droplet is squeezed at the equator, resulting in the shape as shown.

It is noteworthy that an electrostatic field in general produces a potential apex that is intrinsically unstable for the purpose of levitation. As a result, delicate dynamic control system is required to make the levitation operation feasible. This is in contrast with induction principle, which produces a potential wall for intrinsically stable electromagnetic levitation.

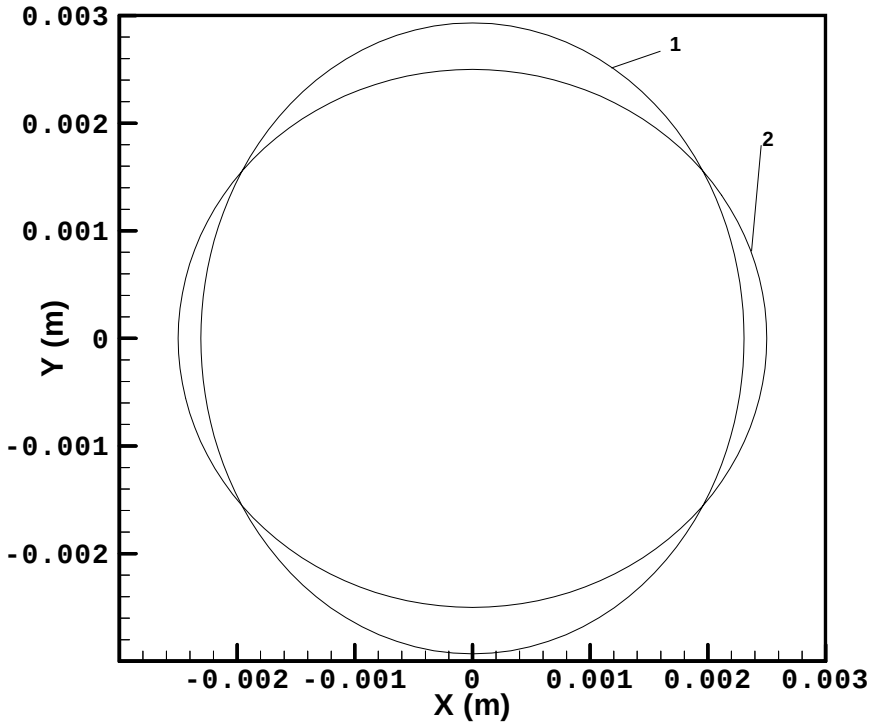

Figure 4.3 Comparison of free surface profiles of an electrically conducting droplet in normal and microgravity: (1) E_0=3.3 x 10^6 V/m and Q=0 C, and (2) un-deformed liquid sphere.

4.2.3 Steady state fluid flow and temperature distribution

As stated before, the only non-zero Maxwell stress component on an electrically conducting droplet is normal to the droplet surface in the natural coordinate, which contributes to droplet deformation only. Therefore, the fluid flow in the droplet is caused by the surface tension variation along the surface only, which in turn stems from a non-uniform temperature distribution created by laser heating. While any types of heating arrangements can be simulated with the numerical model described above, we consider below four different types that are either used in practice or being considered for use in the near future. These heating arrangements give rise to a complex 3-D flow structure, except an axisymmetric placement of heating lasers.

(a) One laser beam on a pole or equator

Early practice of heating the sample in an electrostatic levitator is to apply one laser beam at either the equator or one of the poles. When the laser beam is directed at the pole, the flow field and temperature distribution are axisymmetric and thus a 2-D model is sufficient to describe the transport phenomena. This 2-D model was reported in early studies [Song, 2000b, 2001] and here it serves as a check on the 3-D model. The 3-D model uses a quarter model consisting of a slice cut by two planes intersecting long the z-axis. The comparison of the previous 2-D model and the present 3-D model results indicates that the two produce the same flow pattern and agree within 0.1% (relative error) in maximum velocities calculated, verifying that the 3-D model indeed reproduces

the asymmetric model results (see Fig. 4.4 (a,b)). Other meshes, such as whole sphere and half sphere were also used for additional testing and the same conclusions were held.

When the laser is directed at the equator, however, the flow and temperature distributions are no longer strictly axisymmetric. This is because the sample, after deformation, does not possess a rotational symmetry with respect to either the x or y axis. However, the fields are of four-fold symmetry with respect to the y-x plane and x-z planes. This symmetry condition permits the use of another quarter model, which is a quadrant formed by the y-x plane and x-z planes, when the laser beam is applied along the x-axis. The calculated results of the steady state thermal and fluid flow fields are shown in Fig. 4.4 (c, d). Inspection of the results suggests that the flow and temperature distributions head at the pole and equator are very similar. And even the temperature difference and velocity are nearly the same (with <0.1%). Thus, for one-beam heating configuration, the thermal and flow fields are not strongly affected by the placement of the laser heating source, and flow is characterized by a single recirculating loop in a plane cutting through the x-axis. Further simulations show that unless the deformation is large, this conclusion remains true.

These simple flows are also illustrative of the underlying physical principles governing the Marangoni flow in the droplet. As the droplet is heated up, the temperature is higher within the laser beam coverage and decreases away from the heating center. The steady state thermal field is established eventually when the radiation and heating are balanced. This non-uniform temperature distribution causes a change in surface tension so as to establish a surface force gradient on the droplet. For the case under study, the surface tension force increases with decreasing temperature. Consequently, the higher

force pulls the fluid particles away from the low force region and moves them along the surface from high to low temperature region, where flow moves inward to form a recirculating loop in compliance with the mass continuity requirement.

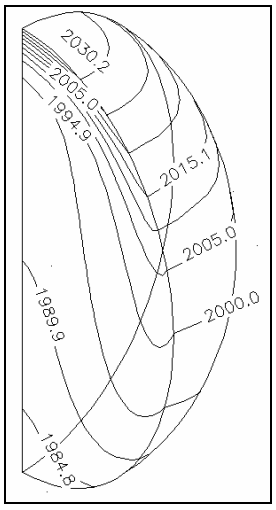

(a)

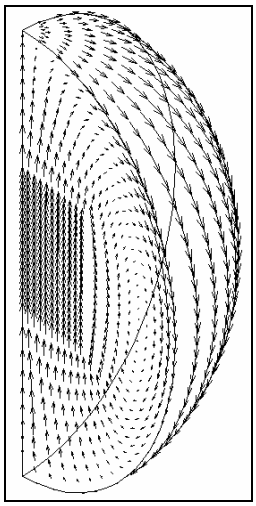

(b)

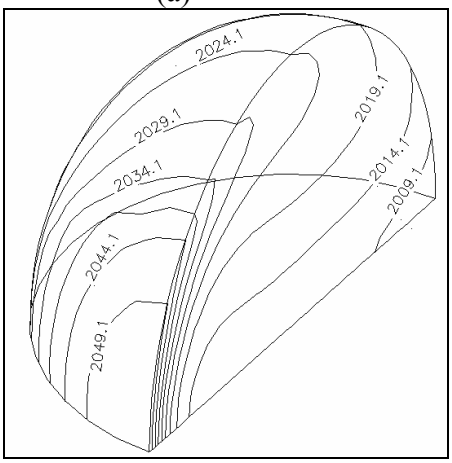

(c)

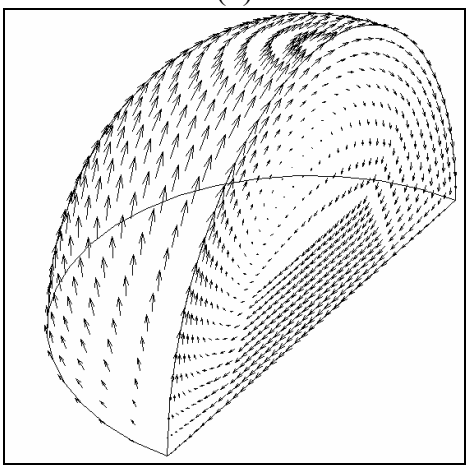

(d)

Figure 4.4 Temperature distribution and internal fluid flow in an electrostatically deformed droplet under mcirogravity with a single beam heating laser: (a)-(b) for single beam placed at the north pole -- Umax=14.64 (cm/s) and (c)-(d) for single beam placed at the equator – Umax=14.43 (cm/s). Heat flux $Q_0=2.6\times10^6$ (W/m^2).

(b) Two laser beams on the poles or equator

The use of two laser beams to heat the sample is also practiced. The two possible laser beam arrangements are such that the beams are either applied at the two poles, which give rise to a symmetric field distribution, or at the two opposite side of the equator. For the former, a 2-D model is adequate [Song, 2000b], and thus provides once again a checkpoint against which the 3-D model is tested. Computed results confirm that the 2-D and 3-D model predictions are indeed in perfect agreement when the laser beams are applied at the two poles. A 3-D view of the thermal and flow fields is presented in Fig. 4.5 (a, b). The two dimensional, axisymmetric flow structure is well predicted by the 3-D model, as is expected. The temperature is higher at the poles and decreases towards the equator. This establishes a surface force gradient by which the fluid particles are pulled towards the equator at low temperature from the two poles that are at higher temperatures. This, combined with the requirement of mass conservation, generates the double toroidal recirculating flow loops.

To compare, two laser beams are applied symmetrically on the equator. The radius of the laser beams is the same in the two cases. Strictly speaking, surface

deformation precludes the use of the rotational symmetry condition; but the 8-fold symmetry is still applicable. As a result, only an octant is required for the calculations. The computed results, showing the temperature and fluid flow distributions both on the surface of and inside the droplet, are presented in Fig. 4.5 (c-f).

Comparison of the results in Fig. 4.5 reveals that the flow structures and temperature distributions are similar for both cases. Detailed analyses, however, uncovers that the rotational flow loop is only approximately symmetric around the axis formed by connecting two heating sources applied at the equator, which is consistent with the geometric constraint. Further numerical simulations show that a rotational symmetric flow field is obtained if a droplet of perfect sphericity is heated with the two heating sources placed at the two opposite sides of the equator. From Fig. 4.5, it is seen also that the internal convection has a strong effect on the temperature distribution, which is suggested by the distorted isothermal contour lines. For these two cases, the temperature difference is 28.8 and the maximum velocity is 10.978 in the case of pole heating, which compares 37.4 and 11.592, respectively, for the equator heating. Further simulations show that with the same Q_o and same radius of laser beams applied at the equator, the average temperature is about 20K higher than heating at the poles, but the temperature difference and hence the maximum velocity is roughly the same as those in Figs. 4.5 (a, b).

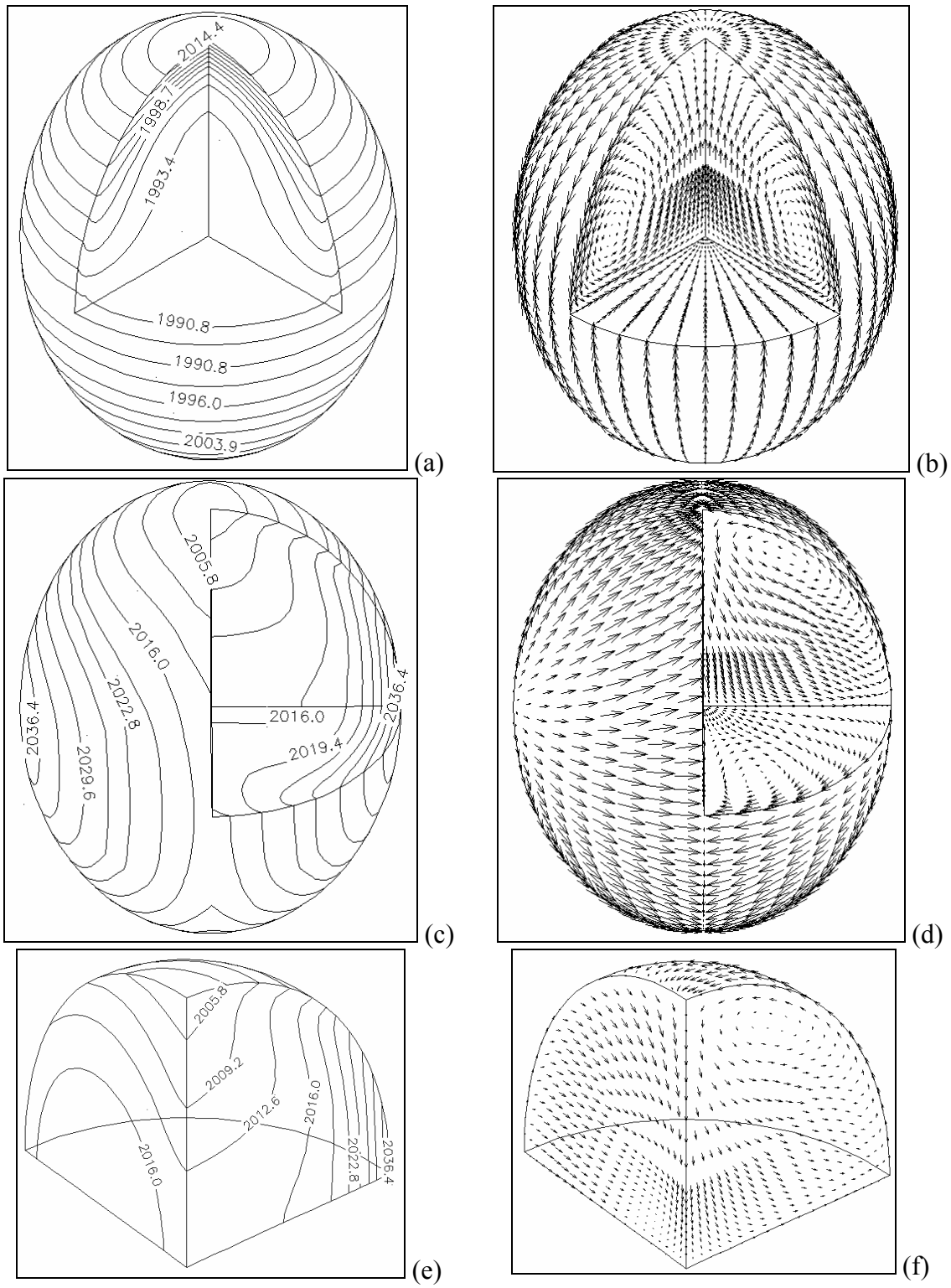

Figure 4.5 Temperature distribution and internal fluid flow in an electrostatically deformed droplet under mcirogravity with heating by dual lasers: (a) and (b) for beams

placed at north pole -- Umax=10.98 (cm/s) and (c)-(f) for beams placed at the equator – Umax= 11.59 (cm./s). Heat flux Q= 1.3×10^6 (W/m^2).

(c) Tetrahedral heating by four laser beams

Recently, there have been strong advocates in the droplet levitation community for the use of a tetrahedral laser beam heating arrangement as a potential means to reduce the temperature gradient in the droplet, thereby reducing the internal convection. In this arrangement, four parts of the droplet surface are heated by lasers beams that are emitted from the four corners of a tetrahedron whose geometric center is coincident with that of the droplet. This design concept may be explored using the 3-D model before expensive instrumentation is put in place, which in essence is the usefulness of a numerical model. Because of the tetrahedral arrangement, symmetry conditions can be applied on the plane that cuts through the two poles and the center of a laser beam placed around the droplet. Thus a 1/3 model is sufficient to represent the complex flow and temperature field in the droplet. The model used 3600 8-node finite element elements.

The calculated results are depicted in Figure 4.6. Clearly, tetrahedral heating creates a rather complex flow structure, with fluid moving from four high temperature regions to the low temperature regions (see Fig. 4.6 (a, c)). The complexity of fluid motion is further revealed by the internal flows shown in Fig. 4.6(b, d). The four hot spots are apparently associated with the laser heating and flows emerge from these hot spots to find their ways to the regions where temperatures are low, as a result of surface forces increasing with a decrease in temperature. Again, the internal flow recirculation

produce a strong effect on the temperature distribution, as is evident in the isothermal contour plots viewed in slice cuts (Figs. 4.6 (a) and (c)).

Comparison of Figs. 4.5 and 4.6 exhibits that a tetrahedral heating arrangement, though produces a more complex internal flow field, indeed gives much more uniform temperature distribution inside the droplet: a temperature difference of 22.9 for tetrahedral heating vs. that of 28.8 for dual laser heating. In sharp contrast with the common perception, the maximum velocity generated by the tetrahedral heating is not reduced significantly in accordance with the temperature reduction. In fact, only a small reduction of velocity (11 %) is observed. This result, which is contradictory to what is anticipated by four-beam advocates, may be explained as follows. While the temperature difference indeed is much smaller with four laser beams than with two beams, the temperature gradient along the surface is not as much different between the two cases, thereby resulting in a reduction of velocity only by 11%. For example, detailed analyses show that for the two beam cases, the temperature gradient between the hottest and coldest spots on the surface is 7.334×10^3, which compares with 7.143×10^3 for four beam lasers.

For surface tension driven flows, Marangoni number is often used as an indicator of flow intensity. For electrostatically levitated droplets under consideration, however, one can not use the Marangoni number based on a single characteristic length (say, radius) to interpret the flows resulting from different heating arrangements for levitated droplets, though it is legitimate for the same heating configuration. This is because the length scales are different for different heating configurations, as discussed in the

paragraph above. A correct use of Marangoni numbers to characterize the flows must take into the consideration the length scale changes for different heating arrangements.

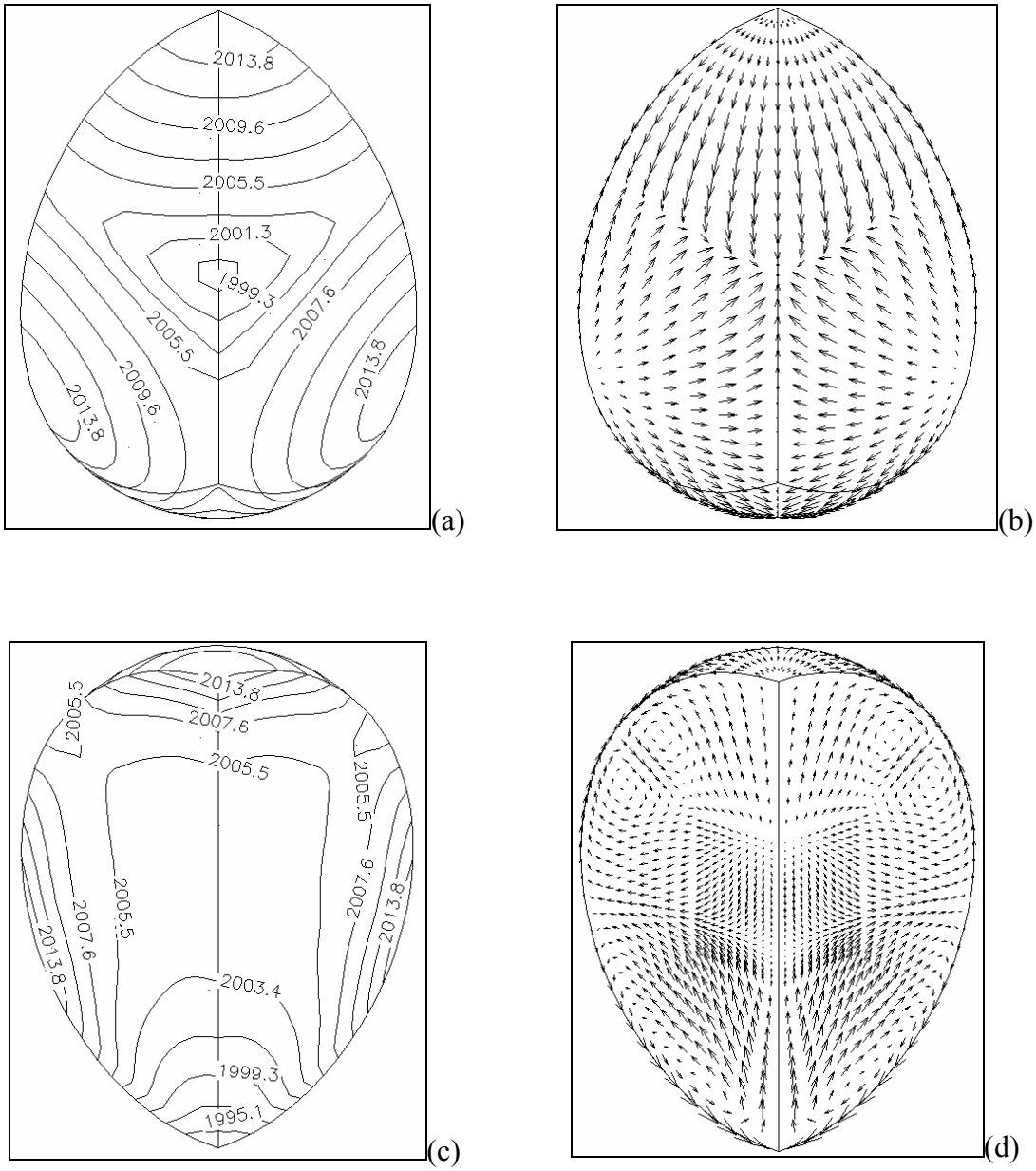

Figure 4.6 Steady state thermal and velocity fields in an electrostatically deformed droplet under microgravity with tetrahedral heating arrangement: Umax=9.728 (cm/s). Q= 0.65×10^6 (W/m^2).

(d). Heating by six laser beams

Besides the dual and tetrahedral laser beam arrangements, other heating placements can also be investigated using the numerical model described above. One of the viable arrangements would be to use a 6-beam laser heating arrangement, symmetrically placed with respect to the center of the droplet, for the purpose of further reducing the temperature non-uniformity and a hope for a smaller flow velocity. One possible arrangement is to slip the laser heating source into six laser beams, which will allow heating to be applied equally on octahedrons of a droplet.

One such calculation is given in Fig. 4.7, where the 6 laser beams are arranged such that two are at the poles and 4 beams are placed around the equator plane with equal spacing, which are distributed at the 8 corners on the octahedron. Compared with the two laser beams' case, the calculated results indicate that the temperature gradient is reduced about 50% and so is the internal velocity with this arrangement. A detailed inspection of these flow structures, although very complex, seems to suggest that these complex flow structures are a result of interaction of the Marangoni flow cells associated with each laser beams.

A summary of major results calculated for different heating arrangements is given in Table 4.2.

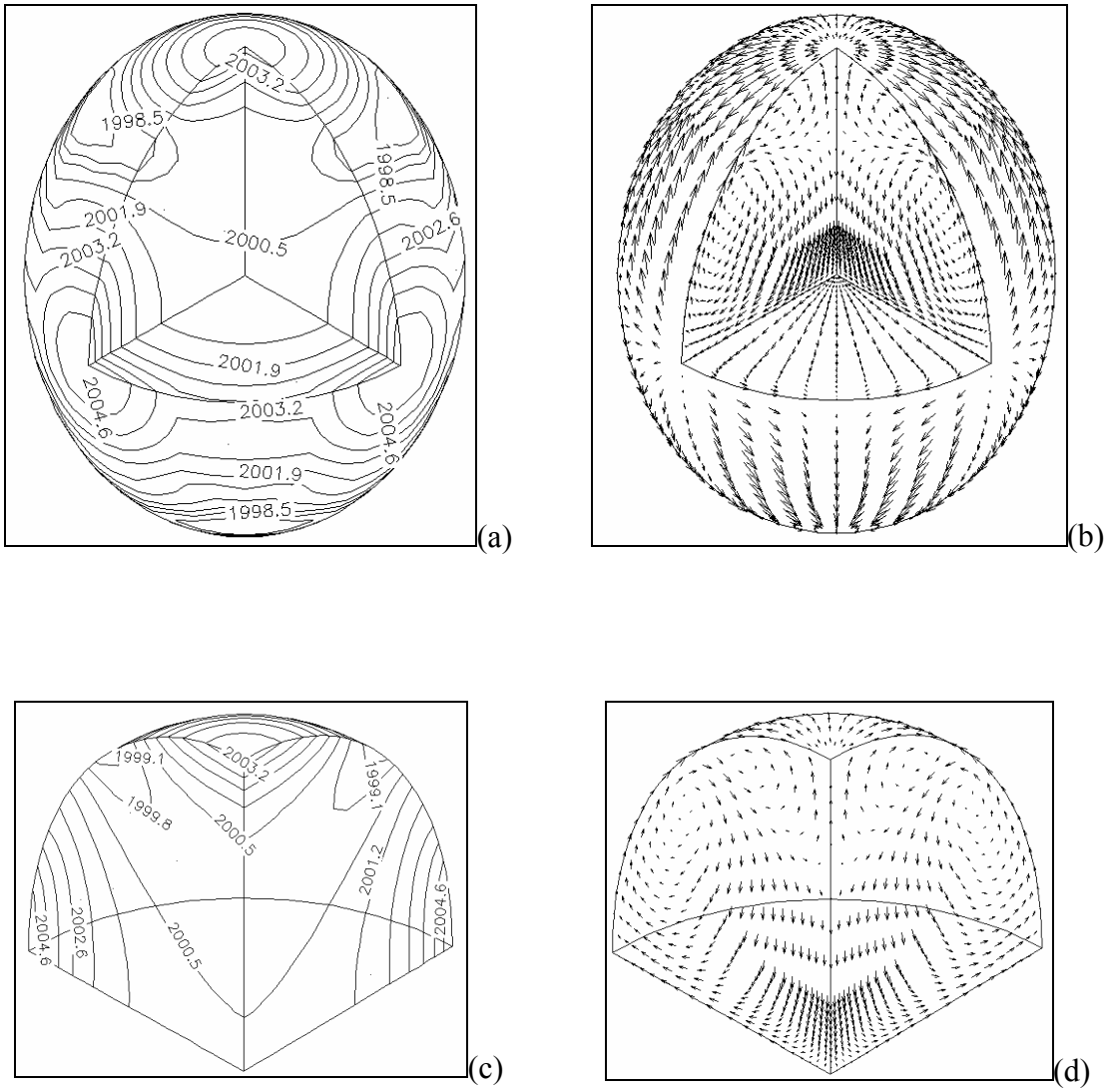

Figure 4.7 Steady state thermal and velocity fields in an electrostatically deformed droplet under microgravity with octahedral heating arrangement: Umax=5.321 (cm/s). Q= $1.3\times10^{6}/3$ (W/m^{2}).

Case	T_{high} (K)	T_{low} (K)	$T_{average}$ (K)	ΔT (K)	U_{max} (cm/s)	**Re**
Two laser heating at two poles	2017.0	1988.2	2002.6	28.8	10.978	216.92
Two laser heating on the equator	2039.8	2002.4	2021.1	37.4	11.592	229.05
One laser heating on northern pole	2035.3	1979.8	2007.55	55.5	14.64	289.28
One laser heating around the equator	2054.1	1999.2	2026.65	54.9	14.43	285.13
Four laser heating on the tetrahedron	2015.9	1993.0	2004.45	22.9	9.728	192.22
Six laser heating on the octahedron	2005.3	1997.8	2001.55	7.5	5.321	105.14

Table 4.2 Effects of heat source arrangement on temperature difference and maximum velocity in an electrostatically levitated Titanium droplet

4.2.4 Transient development of flow and thermal fields

For undercooling studies using the levitated droplets, knowledge of transient flow and thermal fields when heating is turned off is also important. The present 3-D model, like

its 2-D counterpart [Song, 2001b], is also capable of describing the transient development of both 3-D fluid flow and temperature distribution in an electrostatically levitated droplet. Figs. 4.8 and 4.9 show the time development of 3-D fluid flow and thermal fields in droplets heated by 4-beam and 6-beam arrangements, respectively. Apparently, the transient fluid flow structure evolves in time differently for the two cases. The transient simulations of axisymmetric thermal and fluid flow fields induced by single and double beams were discussed in a previous paper on 2-D models.

Inspection of Figs. 4.6 and 4.8 shows that in the case of the 4-laser beam arrangement, the temperature field changes very rapidly when the heating is turned off, which causes a flow reversal near the north pole region and a change in flow structure in the droplet. At time t=0.28 seconds after the laser beams are switched off, the surface temperature is largely smeared out due to both convection and radiation such that the temperatures at the north pole is reduced below everywhere, a manifestation of high heat lose there. In three other heating regions, however, the temperature remains relatively higher. This is explained by the fact that for the same laser beam diameter, the surface areas form which heat loss occurs are much smaller because of a much larger surface curvature radius in these regions. Note also that there exists considerable thermal mixing along the azimuthal direction, which brings the temperature into an axisymmetric field. The consequence of this change in thermal fields is that one smaller toroidal loop near the north pool is engulfed by the loop associated with the side heating source. This phenomenon is consistent with the underlying physics governing the surface tension driven flows discussed in the above section (c).

Turning to the time evolution of the thermal and fluid flow fields induced by the 6-beam heating arrangement, one can see that the similar phenomena are observed in that a lower temperature occurs in the pole regions and the temperature is smeared considerably along the azimuthal direction. This is accompanied by the flow change such that the complex flow structure characterized by several recirculating regions is now replaced by basically two large toroidal flow loops recirculating above and below the equatorial plane, as shown in Fig. 4.9.

To further assess the dynamics of the transient thermal and flow fields, information on the history of velocity and temperature at some specific locations is obtained. Fig. 4.10 shows the decay of maximum velocities and the maximum and minimum temperature differences in the droplet heated by 4- and 6-beams after heating sources are turned off. It is seen that during the first 0.5 seconds after lasers are shut off, both velocities and temperature differences experience dramatic change and then decay gradually afterwards. After an elapse of 3 seconds, the maximum velocities reach essentially the same level in the droplet heated initially by either 4- or 6-beams. The maximum velocity changes in accordance with the temperature differences, in compliance with the basic principle of surface tension driven flows. Examination of these transient results along with 3-D views of flow visualization illustrates that the time at which the velocity and temperature spikes up (t~0.3 sec) corresponds to the time when the internal flow starts to reverse its flow pattern in certain regions, as shown in Figs. 4.8 and 4.9.

Although the temperature differences undergo drastic changes, the temperatures at specific locations do not necessarily do so. Typical time change in temperature and

velocity at specific locations are compared in Fig. 4.11 for the droplets heated by 4- and 6-beams. Compared with Fig. 4.10, these results show that the temperature at the specific point decays more smoothly, although the maximum and minimum temperature differences vary more drastically during the initial transient period. The temperature at this point decreases by about 260K below the steady temperature or 200 K below the melting temperature. The velocity at the point where the highest steady-state temperature is attained decays very quickly initially and remains approximately constant afterwards.

The evolution of temperature distributions along a line emitting from the center to a point on the droplet surface is plotted in Figs. 4.12 (a) and (b) for 4-beam and 6-beam heating arrangements, respectively. These results show that the steady state temperature distribution is rather uniform and as temperature drops, the temperature distribution changes more rapidly. The largest change occurs at around t~0.25 seconds. Note that for clarity of the plots, different scales are used for the temperature distribution at t=3 seconds, at which time a temperature difference between the center and the surface is ~7K is obtained for the 4-beam case and ~5K for the 6-beam case.

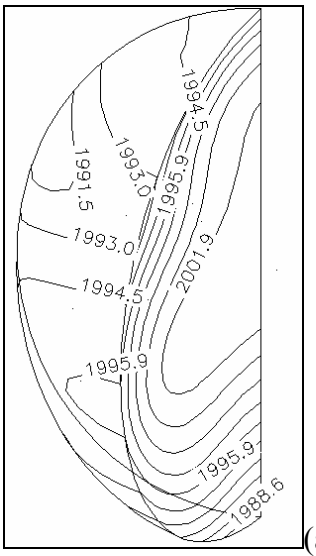

(a)

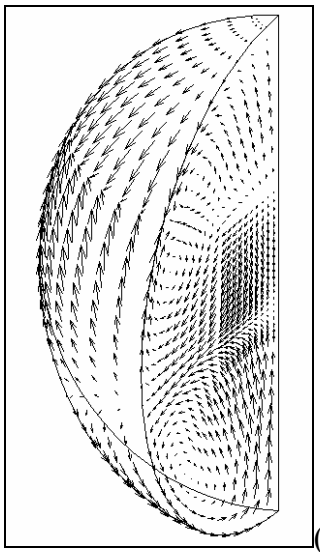
(b)

Temperature and flow at 0.07 second

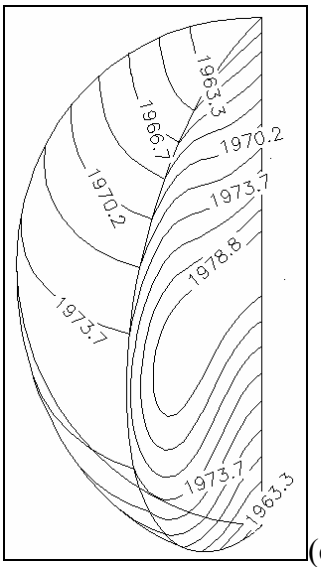

(c)

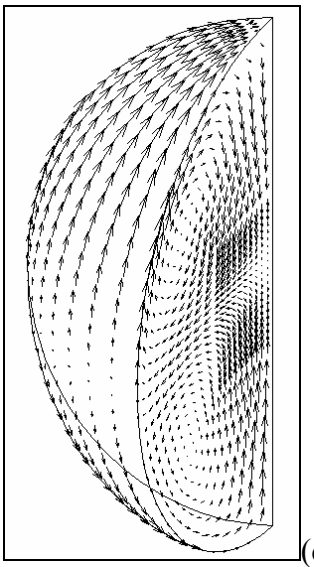
(d)

Temperature and flow at 0.28 second

Figure 4.8 Snapshots of thermal and melt flow fields during their decay as heating lasers are turned off: (a) temperature distribution and (b) velocity field (Umax=4.376 (cm/s)) at t=0.07 sec., and (c) thermal field and (d) velocity profile (Umax=6.941 (cm/s)) at t=0.28 sec. The initial conditions for the calculations are given in Fig. 4.6.

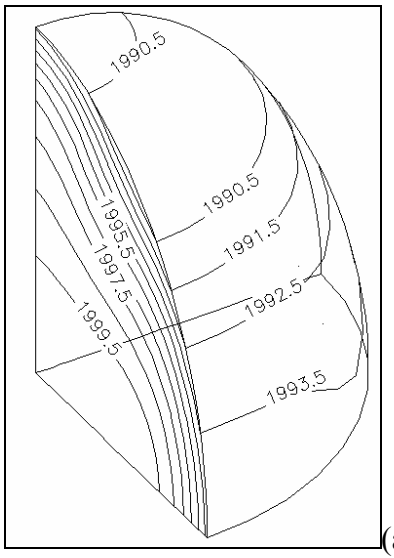

(a)

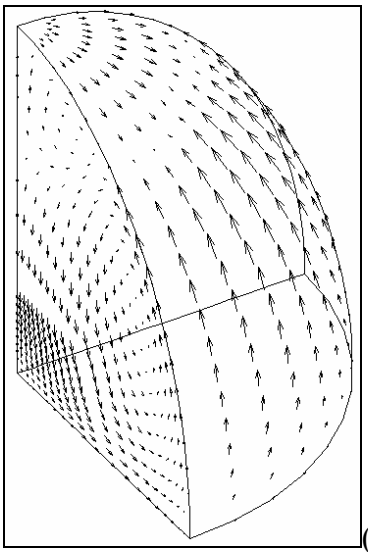
(b)

Temperature and flow at 0.04 second

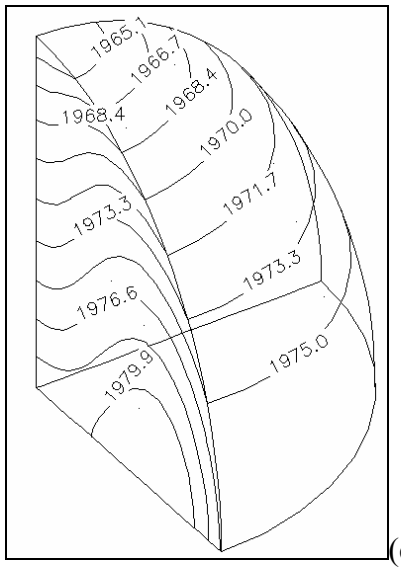

(c)

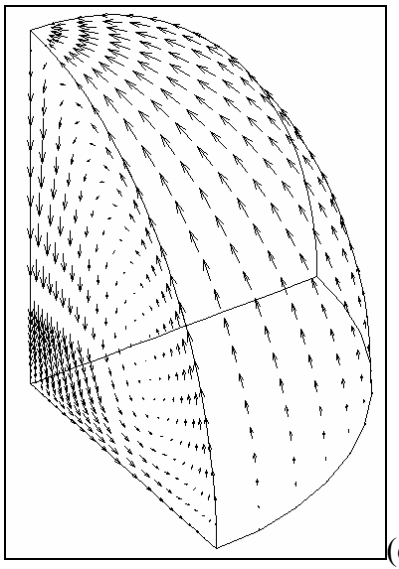
(d)

Temperature and flow at 0.22 second

Figure 4.9 Snapshots of thermal and melt flow fields during their decay as heating lasers are turned off: (a) temperature distribution and (b) velocity field (Umax=3.812 (cm/s)) at t=0.04 sec., and (c) thermal field and (d) velocity profile (Umax =6.561 (cm/s)) at t=0.22 sec. The initial conditions for the calculations are given in Fig. 4.7.

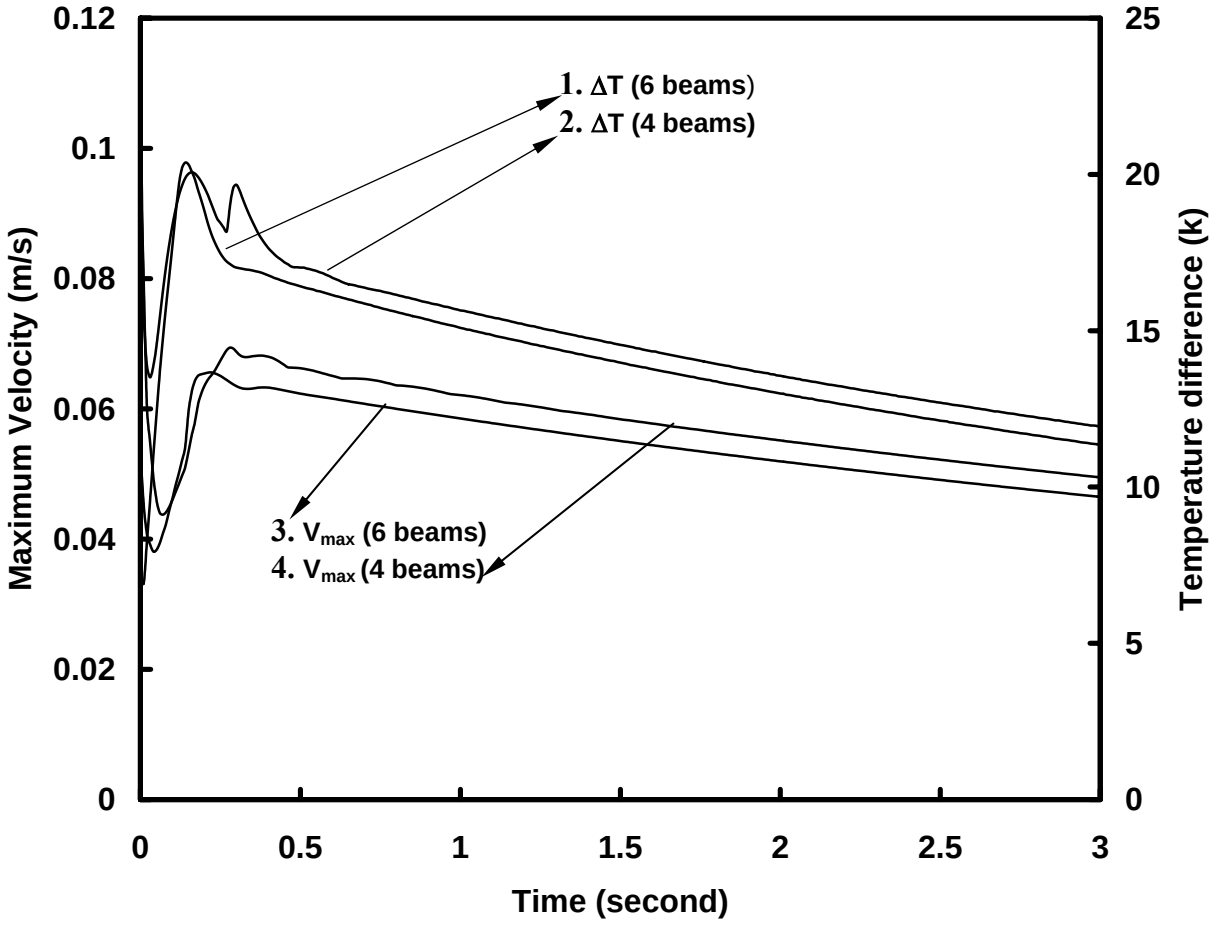

Figure 4.10 Decaying history of maximum velocities and the maximum and minimum temperature differences in the droplets heated by 4-beam and 6-beam heating lasers, after heating is switched off.

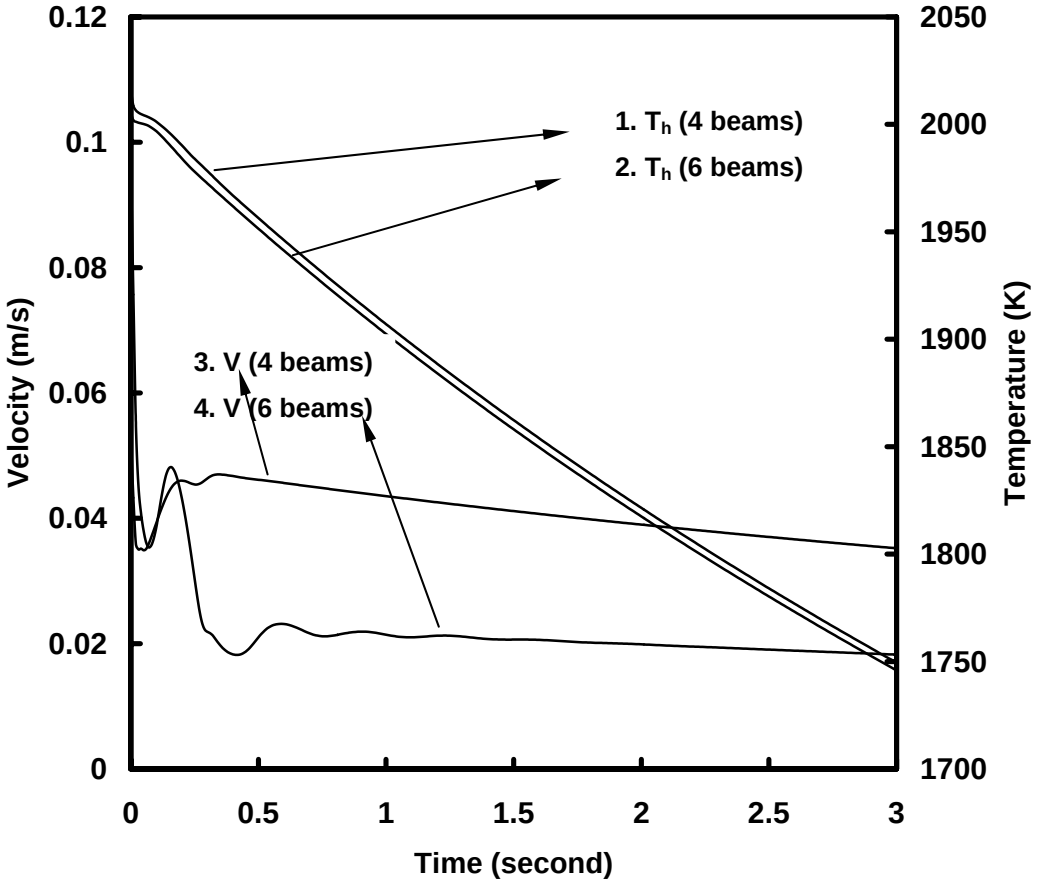

Figure 4.11 Transient development of velocities and temperatures at specific points in the droplets heated by 4-beam and 6-beam heating lasers, after heating is switched off. The velocities are monitored at ($x=9.3106\times10^{-4}, y=5.3755\times10^{-4}, z=-2.5955\times10^{-3}$ all in meters) for 4-beam and at (-2.9974×10^{-4}, $1.8925\times10^{-3}, 1.6365\times10^{-3}$) for 6-beam where the maximum steady state velocities are attained. The temperatures are monitored at ($1.8425\times10^{-3}, 1.0638\times10^{-3}, -1.1372\times10^{-3}$ for 4-beam and at ($0, 2.3075\times10^{-3}, 0$) for 6-beam where the maximum steady state temperatures occur in the droplets.

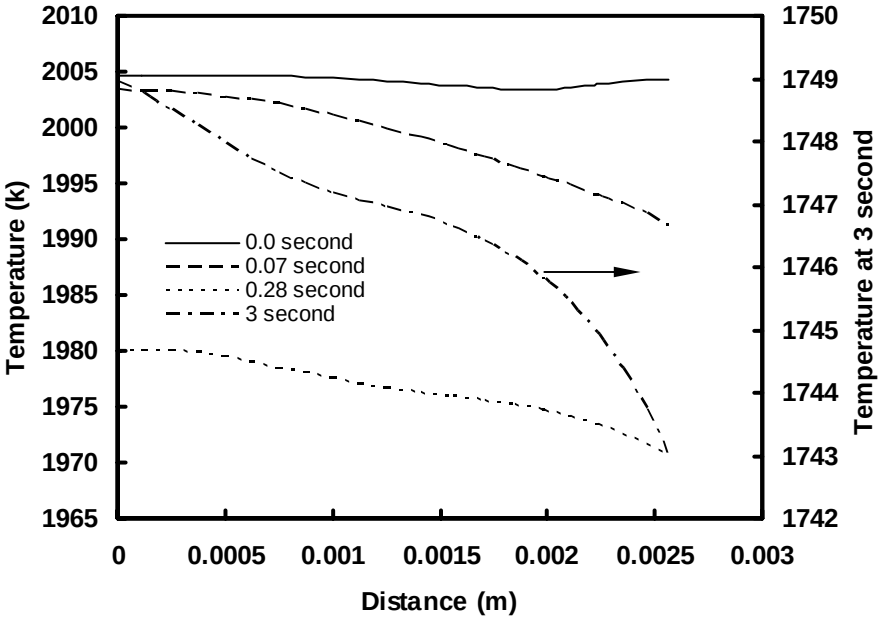

(a)

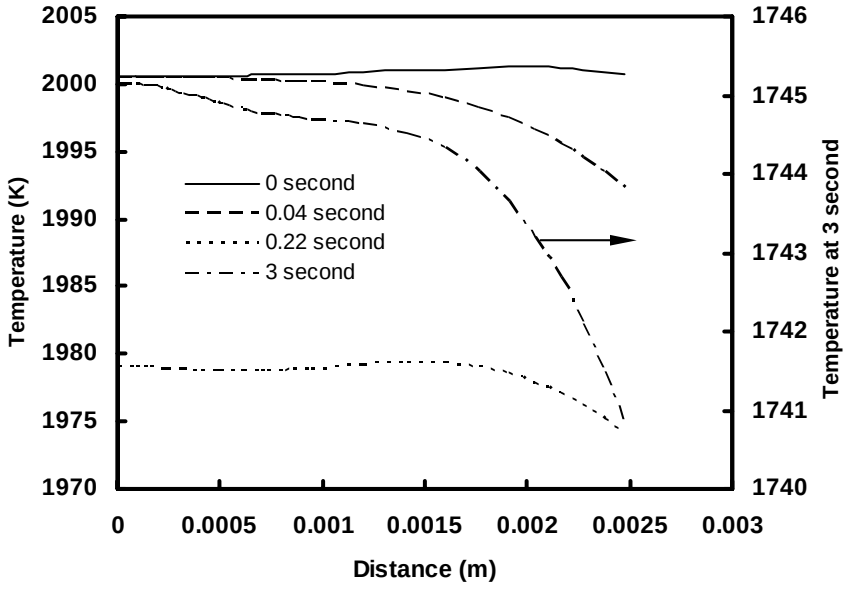

(b)

Figure 4.12 Evolution of temperature distributions along the line emitted from the center of the droplet to (0,1,1) on the surface for (a) tetrahedral and (b) octahedral heating arrangements. The curve at t=3 seconds refers to the vertical axis at right.

4.3 **Concluding Remarks**

This chapter has presented a numerical model for steady-state and transient 3-D Marangoni convection and heat transfer in electrostatically levitated droplets. The numerical model development is based on the Galerkin finite element solution of the Navier-Stokes and energy equations. Numerical aspects for the computation of surface driven flows in general curvilinear coordinate system have been discussed within the framework of finite elements and differential geometry. Results of droplet deformation by electrostatic forces and both steady-state and transient 3-D Marangoni flows in droplets heated by a variety of heating source arrangements have been presented. For practical microgravity conditions under which the deformation is small, the single and double beam heating arrangements, when placed at the poles (or equator plane), produce exactly (or approximately) axisymmetric flow profile and temperature distribution with the axis of symmetry defined by the line passing through the centers of the laser beam and the droplet. As such a 2-D axisymmetric model could provide a reasonably good description, and an exact one when placed at the poles. Complex 3-D flow structure emerges when a tetrahedral or octahedral heating arrangement is applied. These complex flow structures result from the interaction of melt flows associated with each laser beam. For the case studied, the tetrahedral heating arrangement does not seem to produce a significant reduction in internal velocity, in contrast to perception, while the temperature is more uniform. This is attributed to the fact that the 2-beam and 4-beam arrangements result in a surface temperature gradient of approximately the same magnitude. While the Marangoni numbers are able to characterize the flow for a same heating arrangement, a

correct use of them needs to factor in the different length scales associated with different heating placements. The six-beam heating placement produces, however, a much more significant reduction in both velocity and temperature non-uniformity. During the transient decaying, both temperature and velocity fields evolve in a complex fashion with the initial stage dominated by the thermal and flow mixing on the surface of a droplet that has been heated by 4- or 6-beam lasers. The flow reversal is also observed in the droplets during the decay, and a spike in velocity and temperature is found at the time when the flow reversal is taken place. The strong surface mixing quickly brings out a surface temperature distribution of axisymmetry, while inside the droplet the 3-D structure still persists until much later.

CHAPTER 5

3-D SIMULATION OF MASS TRANSFER IN THE ELECTROSTATICALLY LEVITATED, SINGLE-PHRASE DROPLET

5.1 Introduction

In this chapter, a mathematical model is developed for the solute transport phenomena in electrostatically levitated droplets under microgravity, based on the computational results of the free surface deformation, full 3-D Marangoni convection in chapter 4. The thermal transport in the droplet is conduction-dominant for the cases studied. In general, the convection is stronger with higher melting point melts. The internal convection has a strong effect on the concentration distribution in the droplet. For melts with high viscosities, a significant reduction in velocity can be achieved with an appropriate laser beam arrangement, thereby permitting a diffusion-controlled condition to be developed.

5.2 Results and Discussion

Solute distribution in electrostatically positioned droplets is calculated using the numerical procedure as described in chapter 3. Numerical simulations were carried out and a selection of computed results is presented below. The physical properties used for calculations are listed in Table 5.1. The mesh independence testing procedure for droplet deformation and internal convection computations has been discussed in the chapter 4. Because of the small magnitude of mass diffusion coefficient (D) (See Table 5.3), a

denser mesh is needed to obtain mesh independent results. Therefore, the simulation of mass transfer used 8,036 8-node elements for the two- and six-beam cases and 9,184 8-node elements for the four-beam case, respectively. The velocity fields are interpolated from the coarse mesh to the dense mesh. Numerical simulations were also made for selected cases using the dense meshes to ensure no loss in accuracy due to interpolation. The meshes used for shape deformation calculations and for the mass diffusion are illustrated in Fig. 5.1. The mesh distribution for the thermal and flow calculations is similar to chapter 4 and thus not shown. The convergent criterion of 1×10^{-4} (relative error) is set for the nonlinear iteration of the droplet shape coordinates and the temperature, velocity and concentration fields.

Let us turn our attention to the solute transport in the droplets. While the mathematical model described here has no limitations of where and when to add the solutal elements into the droplet, a special situation is considered here where a mass flux method is used to deposit a solutal element on the molten droplet when the flow reaches a quasi-steady state. The deposition rate is assumed such that the concentration on the droplet surface is maintained as a constant. As a first approximation, the surface tension is assumed to be the same as the pure material into which solutal elements are added. This assumption is thought to be reasonable so long as the concentration is dilute, say 5 to 10% [Johnson, 2002]. This allows the calculation of solute transport to be decoupled from the thermal and flow calculations. The effects of the mixture need to be considered if the concentration is high, however; and when this happens, the concentration distribution must be calculated together with the thermal and flow fields.

Figure 5.2 depicts a set of snap shots of concentration distributions in levitated droplets heated by two-beam, four-beam and six-beam arrangements. As a comparison, the concentration distribution under pure diffusion is also given in Figure 5.2 (g-h). Comparison of these results illustrates the significant effect of the internal convection on the concentration distribution in the liquid Al droplet. Clearly, for the droplet under consideration, the mass transport is convection dominant. This is also supported by the ratios of the diffusion velocity and the convection velocity is given in Table 5.3. It is noted that in the case of the six-beam heating arrangement the flow is less intensive and thus a longer time duration is selected to show the convection effects.

To further understand the mass transport phenomena in the droplet, the concentration distribution along several different radial directions originating from the center of the droplet to its surface is plotted at t = 0.5 second. The results are shown in Figure 5.3. The effects of convection on the concentration distribution are evident, confirming the conclusions drawn from the above 3-D contour distributions.

As discussed before, a more vigorous internal flow occurs in the droplets of higher melting point and thus should have a stronger effect on solute distribution. From Table 5.1, it is seen that there exists a much larger velocity in the molten Fe droplet, which results in a more pronounced effects on solute transport. This is further confirmed by the results given in Figure 5.4, where the Si and Ti concentrations at the center of the droplet reaches a quasi-steady state in the Fe droplet much more quickly than the Cu and Fe concentrations in the Al droplet. The 3-D view of the Si and Ti concentration contours, however, is similar to those given above.

One of the important applications of electrostatically levitated droplets is to develop a diffusion-dominating condition in a larger sample for both fundamental materials science studies and for physical property measurements, which would otherwise be difficult to obtain on Earth. To achieve this, the Magangoni convection in the droplet must be controlled below the diffusion velocity so that the concentration profile is predominant by diffusion mechanism. The present mathematical model should be useful to test the novel concepts developed along these lines. Many numerical simulations were conducted with the model. It is found that a logical approach would have to rely on an appropriate choice of materials and the heating source configurations.

One case study is given here, which is concerned with measuring diffusion coefficients of Cu in a glass forming metal using an electrostatically-positioned droplet under microgravity, which is described in [Johnson, 2002]. The parameters used for calculations are given in the third column of Table 5.1. Computations follow the same procedures as described above, that is, the droplet deformation calculation is followed by the thermal and fluid flow and mass transfer calculations. While the flow patterns are very similar to those described above, the flow intensity is drastically reduced because of a much higher viscosity of this material (see Table 5.2). Figure 5.5 displays the concentration distributions in this droplet being heated by three different heating arrangements. The pure-diffusion-controlled concentration contour is also plotted as a comparison. Examination of these results indicates that both two-beam and tetrahedral beam arrangements provide a distorted concentration profile, suggesting that for these two heating arrangements the Marangoni convection is still significant and the mass transfer is not diffusion-dominant. However, the six-beam arrangement gives a

concentration profile similar to that produced by pure diffusion. To further access the effect of convection on the solute transport in the droplet, concentration distributions along two directions are plotted in Figure 5.6 at t = 200 (secs). It transpires that the two-beam and tetrahedral heating arrangements produce concentration profiles significantly deviating from the diffusion controlled profiles, as suggested by the 3-D concentration contours and line plots. On the other hand, the six-beam heating configuration yields a concentration profile that matches with the diffusion profile very closely. Along the radial direction from the center to the south pole, where the largest velocity is detected, the largest error in concentration is about 5% (Figure 5.6a). However, the concentration profile obtained along the line connecting the centers of the droplet and a laser spot at the equator matches almost exactly with that produced by diffusion controlled process, the largest error being on the order of 0.1% (Figure 5.6b). This suggests that a diffusion-dominant condition is possible for this system.

5.3 Concluding Remarks

Complex 3-D internal flow structure results from the interaction of melt flows associated with each of the laser beams, when a tetrahedral or octahedral heating arrangement is applied. Convection is more intensified in high melt point melts. The thermal transport in the droplet is conduction-dominant for the cases studied. However, convection has a significant effect on the solute transport in the droplet of molten metals. Control of the Marangoni convection in the droplet can be achieved with different heating arrangements for different materials. A case study was also presented for the diffusion of Cu in a glass

forming metal alloy, which has a high viscosity. For this metal alloy, a significant reduction in velocity can be achieved and the concentration distribution along some directions matches well with the diffusion controlled profile, when a six laser-beam arrangement is used.

Table 5.1 Parameters used for calculations

Parameters	Al	Fe	Metallic glass forming liquid [4,21]
T_{melt} (K)	934	1809	
Q_0 (W/m^2)	0.97×10^5	1.1×10^6	6.0×10^4
a_d (mm)	2.5	2.5	5.0
a_l (mm)	2.0	2.0	7.0
ρ (kg/m^3)	2385	7015	6000 (Est.)
μ (kg/m-s)	1.3×10^{-3}	5.5×10^{-3}	5 (Est.)
γ (N/m)	0.914	1.872	1.2 (Est.)
$D\gamma/dT$(N/m-K)	-3.5×10^{-4}	-4.9×10^{-4}	-3.0×10^{-4} (Est.)
K (W/m-K)	95.37	78.2	20 (Est.)
C_P (J/kg-K)	1080	795	50 (Est.)
E (V/m)	2.5×10^6	3.3×10^6	2.5×10^6
Emisivity ε_0	0.3	0.3	0.3
Pr	1.472×10^{-2}	5.591×10^{-2}	12.5
T_{aver} (K)	996	1918	1080

Table 5.2 Maximum velocity and temperature difference in droplets

		Al			Fe			Metallic glass forming liquid		
V_{max}, ΔT, and Re at different laser heatings	Cases	2	4	6	2	4	6	2	4	6
	V_{max} (cm/s)	3.50	1.92	0.94	9.04	6.02	2.90	5.8×10^{-3}	1.1×10^{-3}	1.5×10^{-4}
	ΔT (K)	1.28	0.57	0.21	12.19	6.90	2.23	8.7	1.6	0.2
	Re	160	88	43	288	192	92.5	4.9×10^{-4}	9.2×10^{-5}	1.26×10^{-5}

Table 5.3 Diffusion coefficients and V_{max}/V_{diff} for cases studied

Materials	Al-Cu	Al-Fe	Fe-Si	Fe-Ti	Metallic glass forming liquids-liquid metal
Diffusion coefficient $D_o\times10^5$ (cm^2/sec)	7.2	1.4	11	32	1 (Est.)
Diffusion velocity $\times10^5$ (m/s)	1.22	1.22	1.22	1.22	1.22
V_{max}/V_{diff} (for 2 laser beams)	2.87×10^3	2.87×10^3	7.40×10^3	7.40×10^3	4.75
V_{max}/V_{diff} (for 4 laser beams)	1.57×10^3	1.57×10^3	4.93×10^3	4.93×10^3	0.90
V_{max}/V_{diff} (for 6 laser beams)	0.77×10^3	0.77×10^3	2.37×10^3	2.37×10^3	0.12

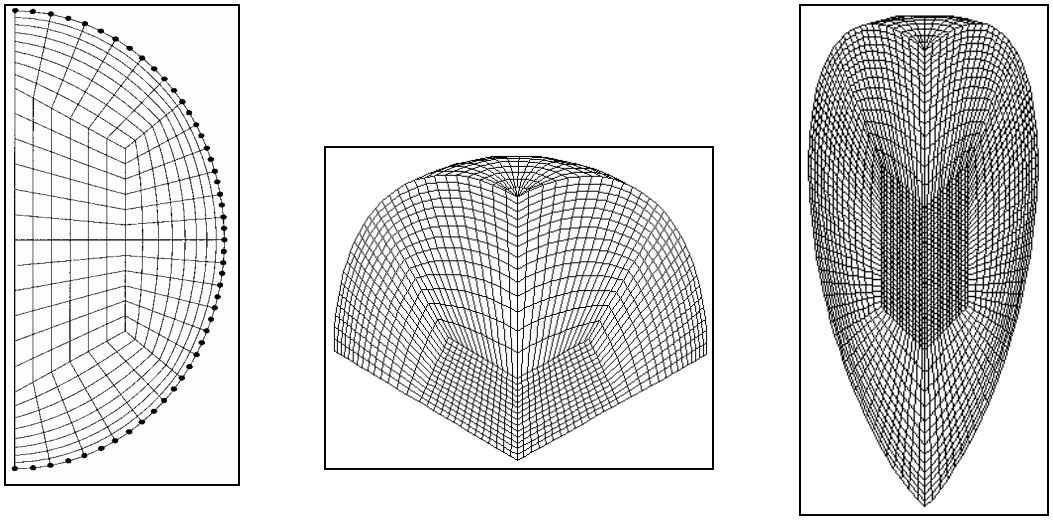

(a) 2-D axisymmetric model (b) octant model (c) one-sixth model

Figure 5.1 Meshes used for shape deformation calculations and the mass diffusion. Note that for the electric and droplet shape calculations, only the boundary elements marked by heavy dots are needed. The internal mesh is used for the axisymmetric Marangonic onvection calculations that used to check the 3-D model predictions for the two-beam arrangement

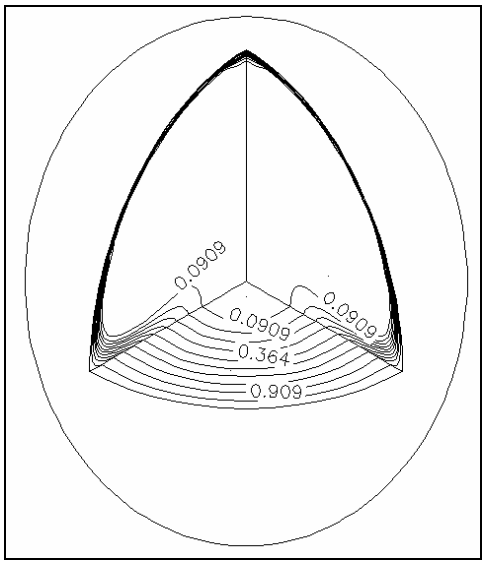

(a) t=0.1 sec

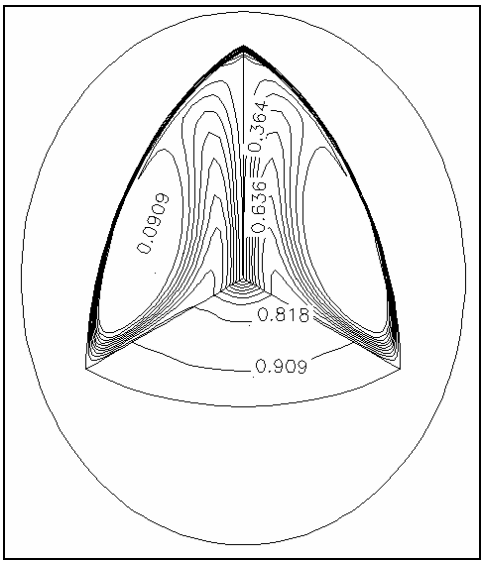

(b) t=0.3 sec

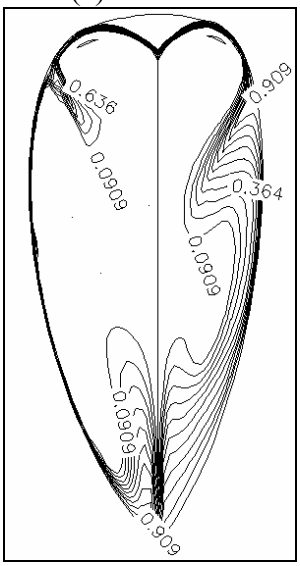

(c) t=0.2 sec

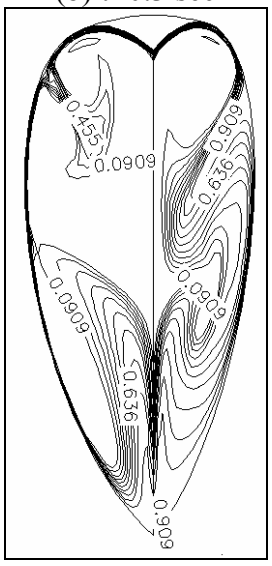

(d) t=0.4 sec

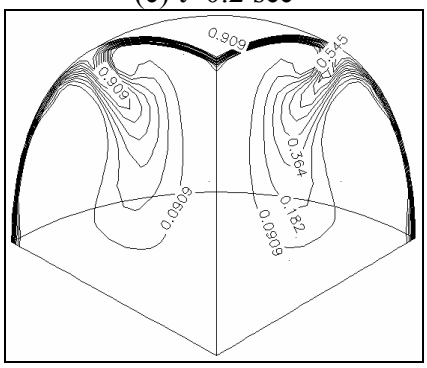

(e) t=0.6 sec

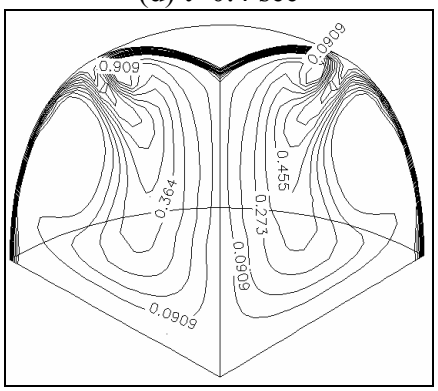

(f) t=0.8 sec

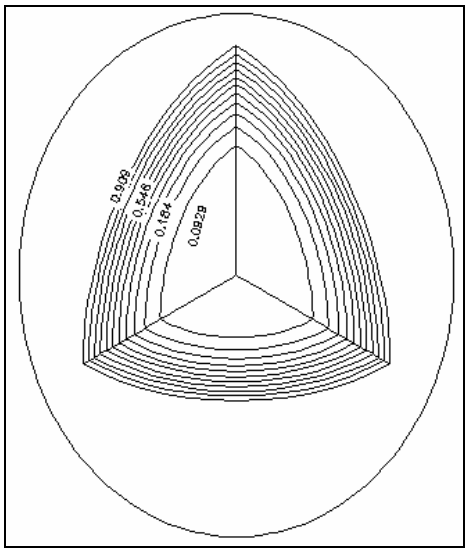

(g) t=25 sec

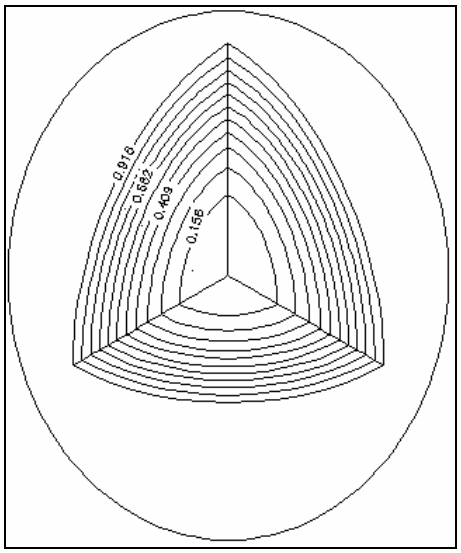

(h) t=50 sec

Figure 5.2 Snap shots of 3-D views of the Fe-concentration distributions in the Al droplet heated by different heating arrangements: (a-b) 2-laser beams, (c-d) 4-laser beams, (e-f) 6-laser beams, and (g-h) no convection

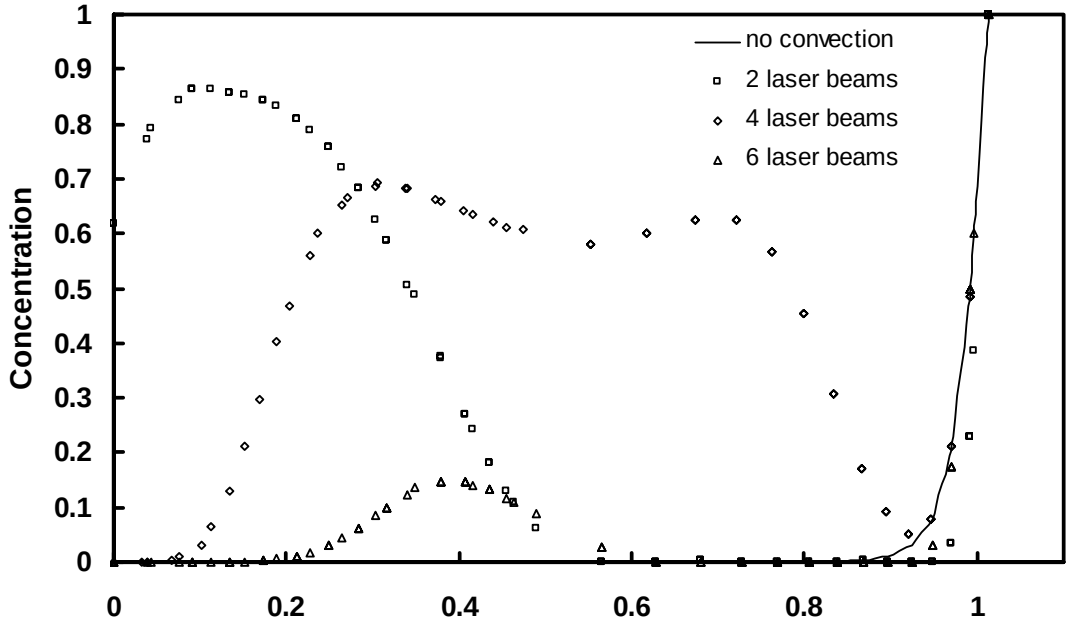

Figure 5.3 Concentration distribution along the line originating from the center (0, 0, 0) to the surface of the Al droplet at t = 0.5 second. The line has an angle of 45^0 above the equator plane (the unit vector of the line: $\hat{r} = \frac{1}{\sqrt{3}}\hat{i}_1 + \frac{1}{\sqrt{3}}\hat{i}_2 + \frac{1}{\sqrt{3}}\hat{i}_3$). The distance is non-dimensionalized by the radius of the droplet. The convection-dominant concentration profiles deviate drastically from the pure-diffusion profiles.

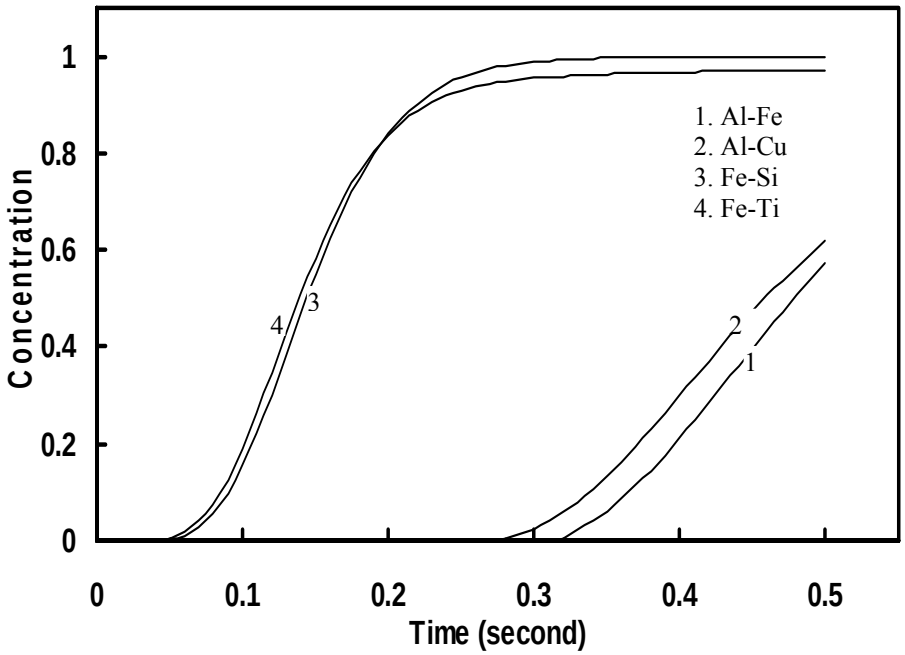

Figure 5.4 Time evolution of the Si and Ti concentrations at the center of the Fe droplet and the Cu and Fe concentrations at the center of the Al droplet. Strong flows in the Fe droplet quickly brings the solute from the surface to the center. The concentration is non-dimensionalized

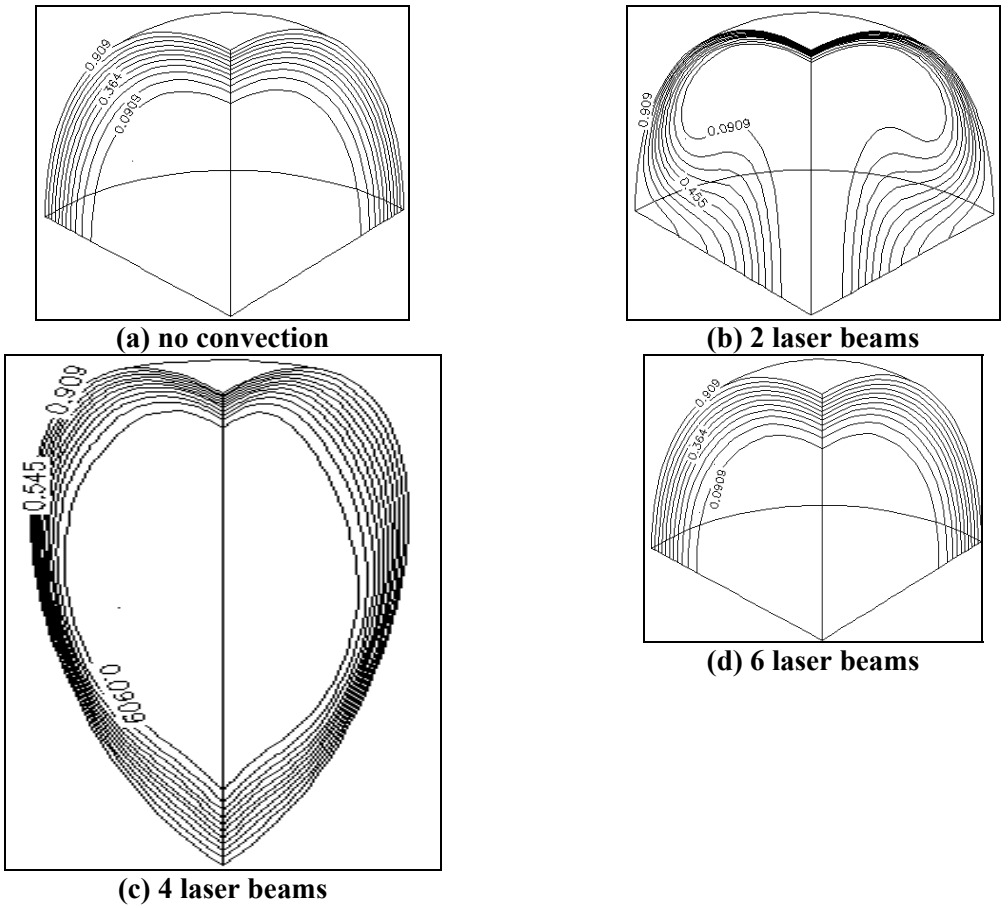

Figure 5.5 A 3-D view of concentration contours in the metallic glass forming droplet heated by different heating arrangements (t = 200 seconds): (a) no convection, (b) 2-laser beams, (c) 4-laser beams, and (d) 6 laser beams

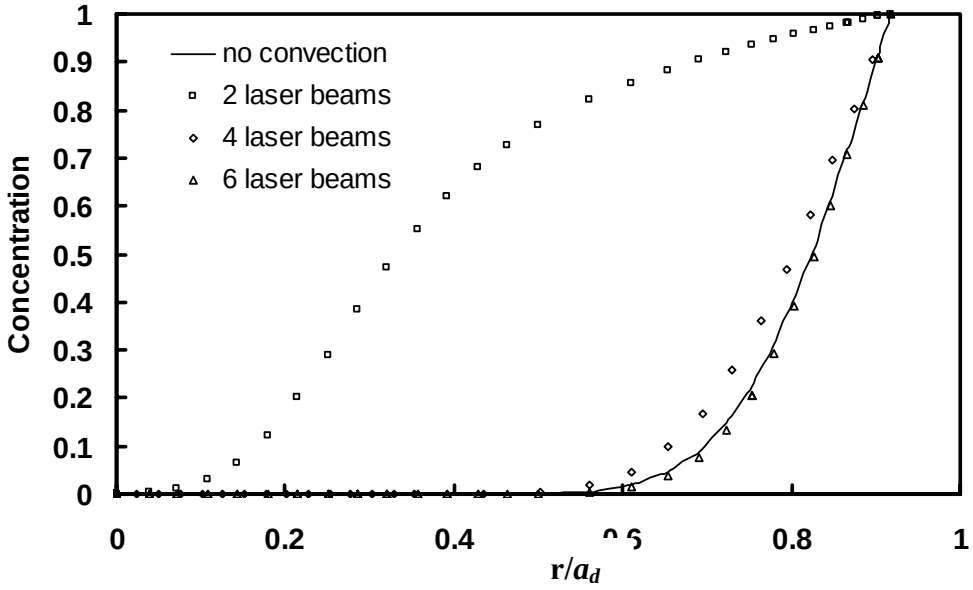

(a)

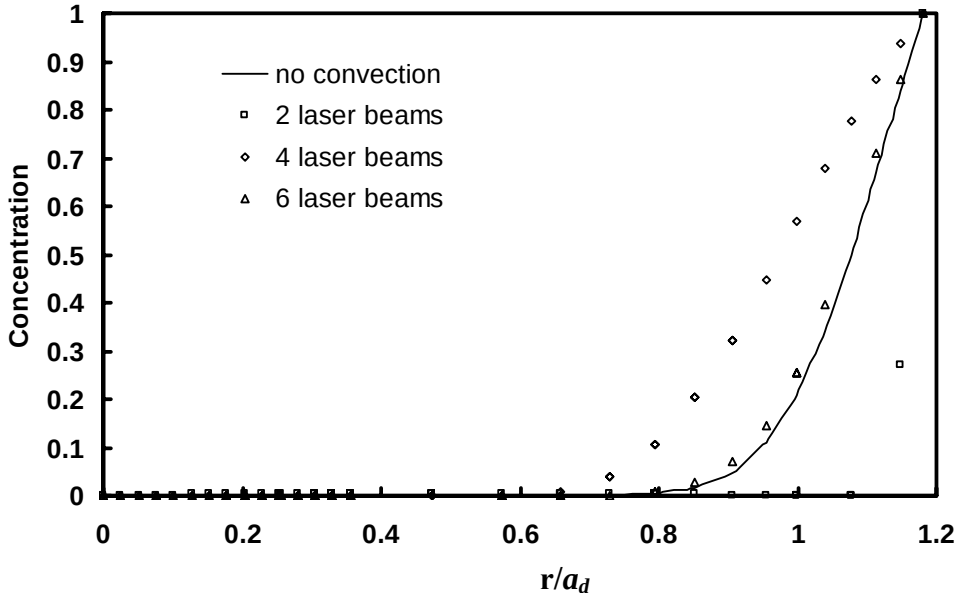

(b)

Figure 5.6 Concentration distributions along radial directions in the metallic glass forming liquid droplet. (a) along the line from center (0, 0, 0) to the equator surface and (b) along the line from center (0, 0, 0) the south pole (unit vector $\hat{r} = -\hat{i}_3$). The distance is non-dimensionalized by the radius of the undeformed droplet a_d

CHAPTER 6

2-D SIMULATION OF THE THERMAL CONVECTION IN THE ELECTROSTATICALLY LEVITATED DROPLET OF IMMISCIBLE LIQUID METALS

6.1 Introduction

In this chapter, a numerical study is presented of the free surface deformation and Marangoni convection in immiscible droplets positioned by an electrostatic field and heated by laser beams under microgravity. The boundary element and the weighted residuals methods are applied to iteratively solving the electric field distribution and the unknown free surface shapes. The Galerkin finite element method is employed to solve the thermal and fluid flow field in both the transient and steady states. Results show that the inner interface demarking the two immiscible fluids in an electrically conducting droplet is immune to the applied electrostatic field and maintains its sphericity in microgravity under steady state conditions. The free surface or, however, deforms into an oval shape in an electric field and its equilibrium shape is determined by the balance of the Maxwell stress and the surface tension. The deformation is attributed to the pulling action of the normal component of the Maxwell stress. The thermal and fluid flow distributions are rather complex in an immiscible droplet. The dominant mechanism for the thermal transport in the droplet is by conduction and convection plays only a minor role. The flow near the free surface is driven by the Marangoni forces, which cause the fluid particles to move from high to low temperature regions. The flow in the inner core

and near the immiscible interface, however, is driven by a competing mechanism between the thermally induced interfacial surface tension gradient and the inertia force in the outer fluid layer. During cooling into an undercooled state after the laser heating is switched off, surface radiation results in a reversal of the surface temperature gradients both along the free surface and along the immiscible interface. This change in the thermal gradients reverses the surface tension driven flow in the outer layer. The flow near the interfacial region is complex and is driven by a complimentary mechanism between the interfacial and the inertia forces during the time when the thermal gradient on the free surface is reversed and that on the interface is not. Before and after the completion of the interfacial thermal gradient reversal, however, the interfacial flows are determined by the competing mechanism between the interfacial and inertia forces.

6.2 Results and Discussion

The computational model developed above enables the prediction of the electric field distribution, the Maxwell stress distribution along the surface of a droplet, droplet shapes, temperature distribution and internal convection within the droplets driven by surface tension and buoyancy forces in normal gravity. A selection of computed results is presented for some immiscible droplets being considered for microgravity applications. Unless otherwise indicated, the computations used the physical properties and parameters in Table 6.1. It is noted that Q_c is the critical charge as predicted by Rayleigh's theory [Rayleigh, 1882], above which a charged drop becomes unstable and starts to break into smaller droplets. A total of 48 linear boundary elements were used for the electric

potential calculations and 24 quadratic boundary elements for free surface deformation calculations. For the problem under consideration, the use of the boundary integral formulation requires a discretization of the droplet boundary only and thus results in considerable computational savings, in comparison with the finite element method, which would have to discretize the entire free space outside the droplet. The thermal and fluid flow calculations used 264 9-node elements, with the penalty formulation for pressure, and the density of the mesh was increased near the free surface to ensure accuracy. A convergence criterion of 1×10^{-4} was set for relative error associated with unknowns for free surface shapes, temperature and velocity. Different meshes and different mesh distributions were also used to check the mesh dependency. The final mesh used for the computations is shown in Figure 6.1. It is determined such that any further refinement of the mesh produces an error smaller than 0.1% (relative to the final mesh).

Parameters	Al	ln	Fe	Pb	Co	Si
T_{melt} (K)	934	429.6	1809	600	1766	1685
ρ (kg/m^3)	2385	7023	7015	10678	7760	2510
$\mu \times 10^3$ (kg/m-s)	1.3	1.89	5.5	2.65	4.2	0.94
γ (N/m)	0.914	0.556	1.872	0.468	1.873	0.865
$d\gamma/dT \times 10^4$ (N/m-K)	-3.5	-0.9	-4.9	-1.3	-4.9	-1.3
K (W/m-K)	95.37	42	78.2	19.9	96.0	138.5
C_P (J/kg-K)	1080	259	795	135	590.0	1040
$Pr \times 10^2$	1.47	1.17	5.59	1.80	2.57	0.71
$\alpha \times 10^6$	37.03	23.09	14.02	13.80	20.97	53.06

Table 6.1 Thermophysical properties used for computations

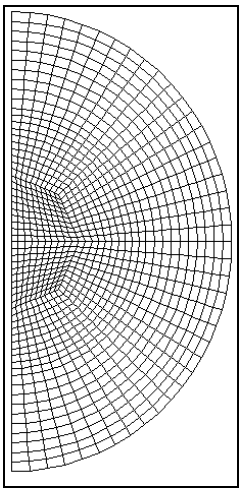

Figure 6.1 Boundary element and finite element mesh for numerical computation

6.2.1 Droplet deformation

There are two interfaces associated with an immiscible droplet. The outer surface is a free surface that separates the droplet from free space. The inner surface is an interface that demarks the two immiscible fluids. Analyses are made to understand the reaction of these interfaces to an imposed electric field, which is used to position the droplet under microgravity.

We first consider the behavior of the inner interface. It is known that when an electric conductor is placed in an electric field, electric charges are induced on its surface. These charges induce an electric field inside the droplet just opposite to the applied field so that the total inside field is identically zero. This is the renowned Gaussian law of electrostatics, which requires that the whole droplet be at the equal potential and the surface charges appear only on the free (or outer) surface of the droplet. This means that

the Maxwell stress along the immiscible interface is zero and the inner interface shape is completely determined by the balance of the hydrodynamic forces along the interface face, or the balance of the surface effect (surface tension times the curvature) by the pressure difference between the two liquids. Thus under microgravity and with the viscous forces neglected under practical conditions, the interface remains spherical and is immune to the electric field outside the droplet. This is illustrated by Curve *a* in Fig. 6.2. It is worthy noting that, form the above discussion, the electric effect will not enter even when the droplet is levitated electrostatically under normal gravity. Of course, when gravity is present, the interface shape should be determined by the balance of the interfacial surface tension and the buoyancy force on the inner fluid, which results from the density difference between the two fluids.

The behavior of the outer surface, on the other hand, is much different. Because of the induced surface charges, the normal component of the Maxwell stress, or the electric force, experiences a jump across the free surface. The force is non-uniformly distributed along the surface, which combines with the surface tension to determine the equilibrium shape of the free surface of the droplet. Two sets of shape deformation calculations are shown as Curves *c* and *d* in Fig. 6.2 for two different applied electric fields, along with the non-deformed free surface shape denoted by Curve *b*. Inspection of Curve *c* indicates that the droplet deforms into an oval shape under the combined action of an applied electric field and surface tension in microgravity. The surface charge density increases from the equator region to the two pole regions, with the positive charges on the upper half surface and the negative charges on the lower half. The charges interact with the applied, upward-point electric field to produce the electric forces that

tend to pull the droplet apart, thereby resulting in the oval shape. A stronger electric field induce stronger electric forces and hence a larger free surface deformation (see Curve d). It is marked here that the symmetric deformation is a consequence of microgravity. Though not shown, under normal gravity, the deformation is asymmetric and the gravity force will cause the droplet free surface to deform into a blob with the pointy portion aligned along the gravity direction. The electric field effect, however, remains the same as discussed above.

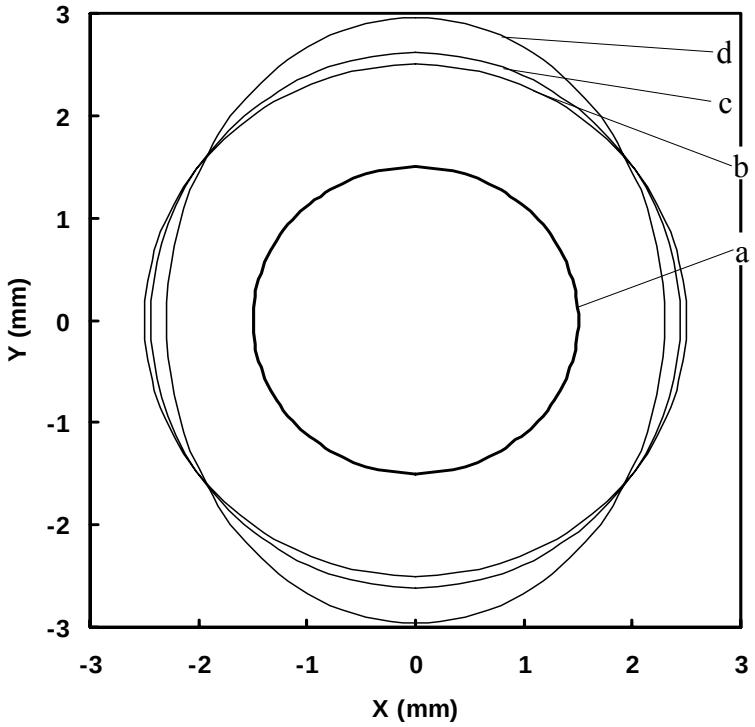

Figure 6.2 Computation of free and interfacial surface of an Al-Pb droplet in microgravity: (a) interfacial surface shape (r_i/r_0 = 0.6); (b) un-deformed free surface of liquid sphere; (c) $E_0 = 1.5\times10^6$ (V/m) and Q = 0 (C); (d) $E_0 = 2.5\times10^6$ (V/m) and Q = 0 (C)

6.2.2 Steady-state temperature and flow fields

As stated earlier, the Maxwell stress only has a component normal to the surface of the droplet and is zero inside. Because it is non-vortical in nature, the stress does not induce internal flow in the droplet. However, the laser heating of the droplet generates a non-uniform temperature distribution both inside and along the surface of the droplet. This temperature variation along the free surface and the interface of the two immiscible fluids gives rise to a non-uniform thermocapillary forces that drive the recirculating fluid flows in both liquids.

Fig. 6.3 summarizes the possible different thermal and flow patterns inside the immiscible droplets electrostatically positioned in microgravity. Here A-B (e.g. Si-Co) means that the outer layer of the droplet is A (i.e. Si) and the inside core is A (i.e. Co); this convention will be used hereafter unless otherwise indicated. The droplet shapes are calculated based on the condition given in Table 6.2. The deformation of the droplet is a result of balance between the electric and surface tension forces along the droplet surface, which differs from droplet to droplet, as shown in Fig. 6.3. The temperature and the velocity distributions along the free surface and along the immiscible interface are shown in Figs. 6.4 and 6.5 respectively.

Analyses are made to understand the underlying physics that governs these complex thermal and fluid field distributions in these droplets. Let us start with the thermal fields. A feature common to these cases is that the temperature field is symmetric with respect to the equator plane, a mere consequence of the laser beams being applied at

the north and south pole regions of the droplets. Detailed examination of the temperature contour distributions in these droplets illustrates that the thermal energy transport inside these droplets are dominant by conduction mechanism and convection plays a minor role. A higher temperature exists near the laser heating spot and decreases along the fee surface and inside towards the equator plane. This is a manifestation of the small Prandtl number associated with these liquid metal droplets (see Table 6.1). It is further noticed that in the case of Pb-Fe, the temperature contours are distorted somewhat more severely than those in other cases, which is attributed to a relatively larger Pr number of Pb and Fe.

We now turn our attention to the thermally induced fluid flow phenomena inside the droplets. First the flow motion in the outer liquid layer is considered. As the temperature decreases from the pole region to the equator plane, the surface tension force increases accordingly. A fluid particle on the free surface experiences a surface force gradient and is dragged from the low to the high force region, thereby causing the melt flow from the pole to the equator regions along the free surface. This surface tension effect is common to in all the six cases shown in Fig. 6.3. At the equator plane, the fluid particle is forced inward into the droplets and finds a way back to the low force region to satisfy the mass conservation, thereby forming a visible recirculating flow insider the outer fluid layer.

The flow distributions near the interface region and insider the inner fluid core, however, display very complex patterns and differ from case to case. While a detailed flow distribution depends on both thermal and physical properties and applied conditions, the complex fluid flow patterns are considered to be attributed to a combined effect of the

interfacial thermocapillary forces and the inertia in the outer fluid layer. Similar to the Marangoni force on the free surface, the interfacial thermocapillary force increases also with a decrease in temperature along the interface and pulls the fluid steam from the high to the low temperature region (see Figs. 6.4b and 6.5b). The interfacial force acts as a momentum source that drives the flow in both fluids. Other the other hand, the flow resulting from the free surface Marangoni force produces an inertia that superimposes the interface and counterbalances the effect from the thermocapillary force. It is this competing mechanism that drives the flow near the interface and the flow inside the core of the droplet.

In the case of Al-In, a strong flow driven by the free surface Marangoni force provides a strong inertia near the immiscible interface and almost completely overpowers the interfacial thermocapillary force, thereby resulting in a very weak flow in the inner fluid core (see Fig. 6.3a). Exchanging the inside and outside fluids gives rise to a weaker flow is generated in the outer layer. Thus a visible recirculating flow appears in the inner fluid (see Fig. 6.3b and Fig. 6.5). Perhaps, this competing mechanism for the internal flows is most revealing in the results shown in Fig. 6.3c. There are four strong recirculating eddies that comprise the entire flow field, with two in the outer and two in the inner fluids. The largest and yet strongest eddy occurs in the outer layer near the equation, which is driven by the free surface Marangoni forces. The eddy in the inner fluid near equator is clearly the consequence of the inertia force dominating the interfacial surface tension effect. In the region near the immiscible interface from the pole ($\theta = \pm\pi/2$) to ($\theta = \pm \pi/4$), the interfacial surface gradient shows its strongest effect and overpowers the inertia force from the outer fluid layer. It provides the major momentum

force that drives the two recirculating loops in the region. When the two fluids switched in positions in the droplet, the interfacial surface force gradient becomes even more effective in driving the fluid motion near the immiscible interface. This is evident in Fig. 6.5 (d) in that the inner fluid is now completely covered by one eddy, which is apparently a consequence of the interfacial force induced eddy engulfing the weak inner flow eddy from near the equator plane. The same can be said for the thermal and fluid flow fields in Figs. 6.3f and 6.3e, respectively. As expected, this competing mechanism between the interfacial surface force gradient and outer flow inertia can cause a variety of different flow conditions.

The flow pattern, velocity intensity and thermal field distribution inside the droplets depend upon various parameters, as discussed above. These fluid dynamics and thermal characteristics are also affected by the ratio of the outer and inner fluid volumes. Two of these cases are shown in Fig. 6.6 for the Si-Co immiscible melt droplets with two different volumes of fluids. Comparison of Fig. 6.6 with Fig. 6.3(e) shows that the interfacial thermocapillary force becomes much stronger when the inner radius over ratio is reduced. Indeed, Fig. 6.6(a) suggests that the flow insider the inner fluid shows an overwhelmingly strong effect from the interfacial surface tension gradient. This contrasts with the case of Fig. 6.6(b), which shows that the effect of the interfacial thermocapillary force is essentially suppressed by the momentum from the outer layer fluid, when the inner-outer radius ratio is reduced to 0.4. This effect is obviously attributed to the fact that a much higher surface temperature gradient exists along the immiscible interface, because of the improved heat conduction due to the increased ratio of the inner over outer radius.

Parameters	Al-ln	ln-Al	Fe-Pb	Pb-Fe	Co-Si	Si-Co	Si-Co	Si-Co
$E\times10^{-6}$ (V/m)	2.5	1.0	2.5	1.5	2.5	2.0	2.0	2.0
$Q_0\times10^{-5}$ (W/m^2)	1.0	1.0	11	11	10	10	10	10
a_d (mm)	2.5	2.5	2.5	2.5	2.5	2.5	2.5	2.5
a_l (mm)	1.85	1.85	1.85	1.85	1.85	1.85	1.85	1.85
a_{di} / a_{do}	0.6	0.6	0.6	0.6	0.6	0.6	0.9	0.4
V_{maxo} (outer surface) (cm/s)	2.44	0.89	7.72	9.17	7.01	5.69	3.90	6.15
V_{maxi} (inner surface) (cm/s)	0.32	0.22	2.48	3.74	2.68	2.36	3.00	1.09
ΔT K (outer surface)	1.40	2.60	16.20	59.90	11.8	8.90	10.3	8.80
ΔT K (inner surface)	0.47	0.58	7.32	8.89	3.24	3.06	7.64	1.33
Ma_i	3.82	3.82	69.73	69.73	18.39	18.39	72.28	12.58
Ma_o	25.45	13.41	264.9	529.8	164.8	58.45	67.12	57.34
Re_o	111.9	82.68	246.2	923.7	323.8	379.8	260.3	410.5

Table 6.2 Parameters and some calculated results

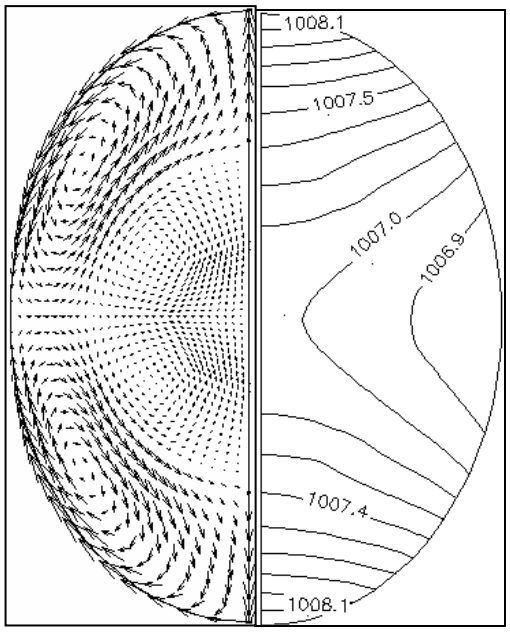

(a) Al-ln

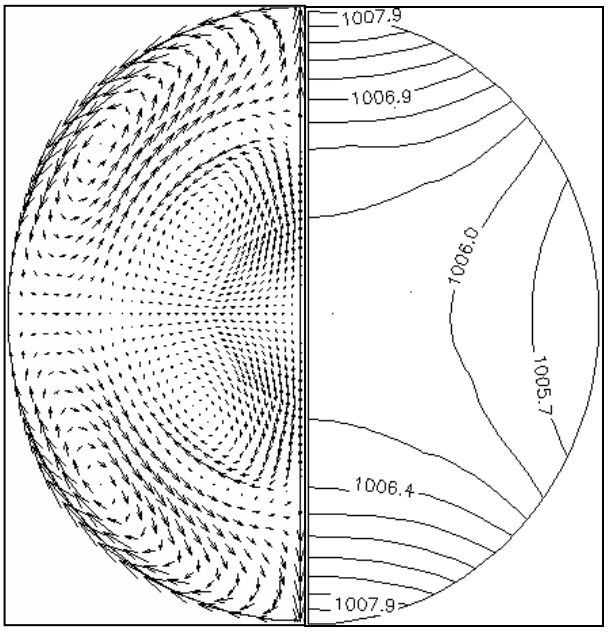

(b) ln-Al

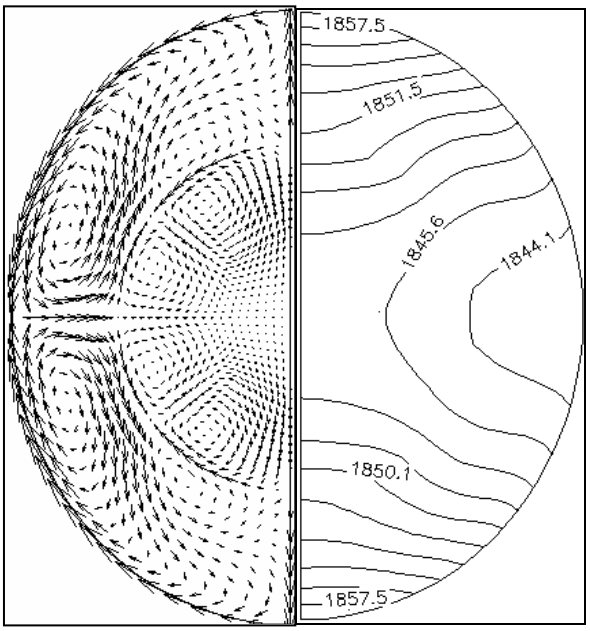

(c) Fe-Pb

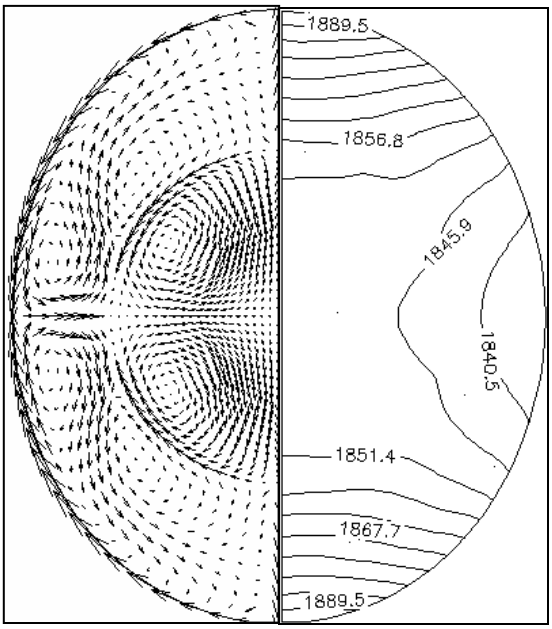

(d) Pb-Fe

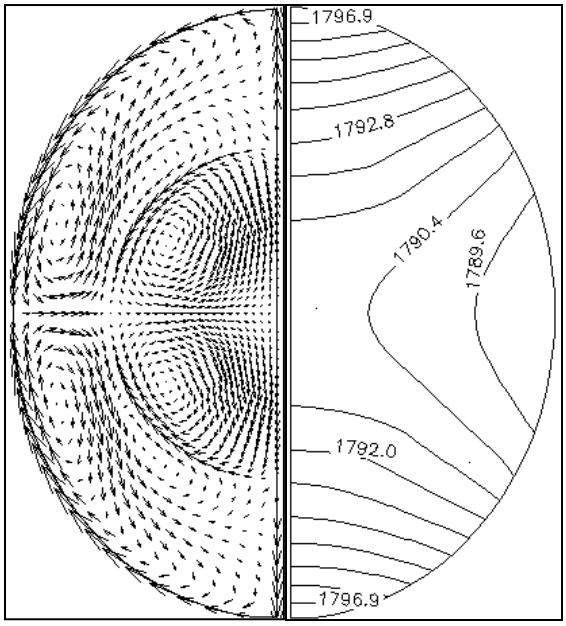

(e) Si-Co

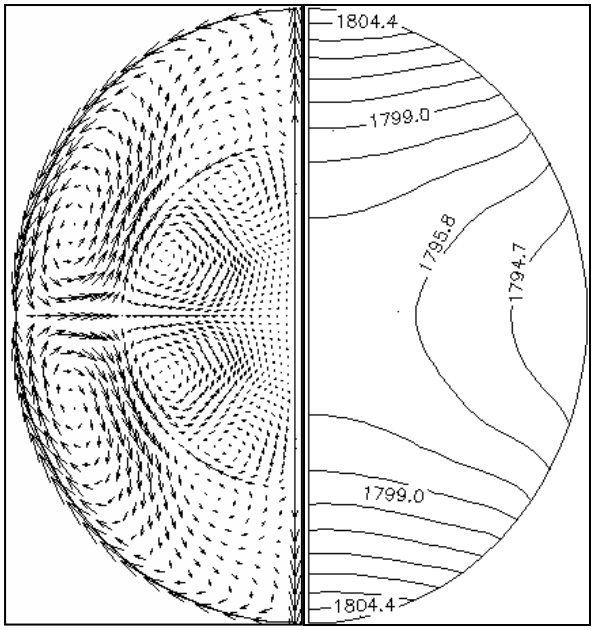

(f) Co-Si

Figure 6.3 Steady-state fluid flow and temperature distribution in the droplet (r_i / r_o = 0.6) for some immiscible materials.

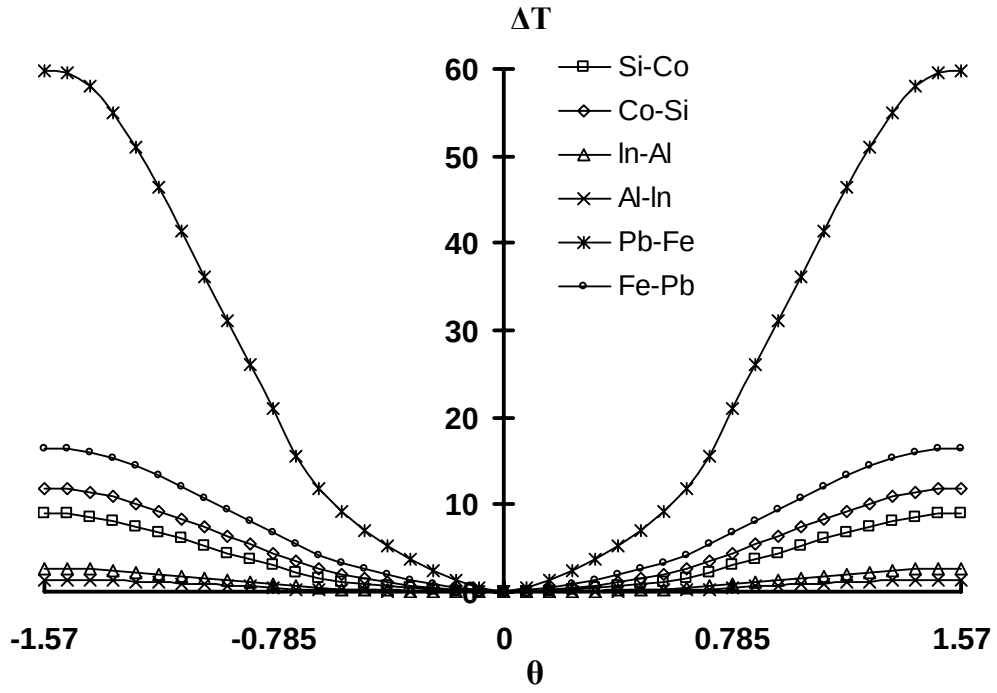

(a)

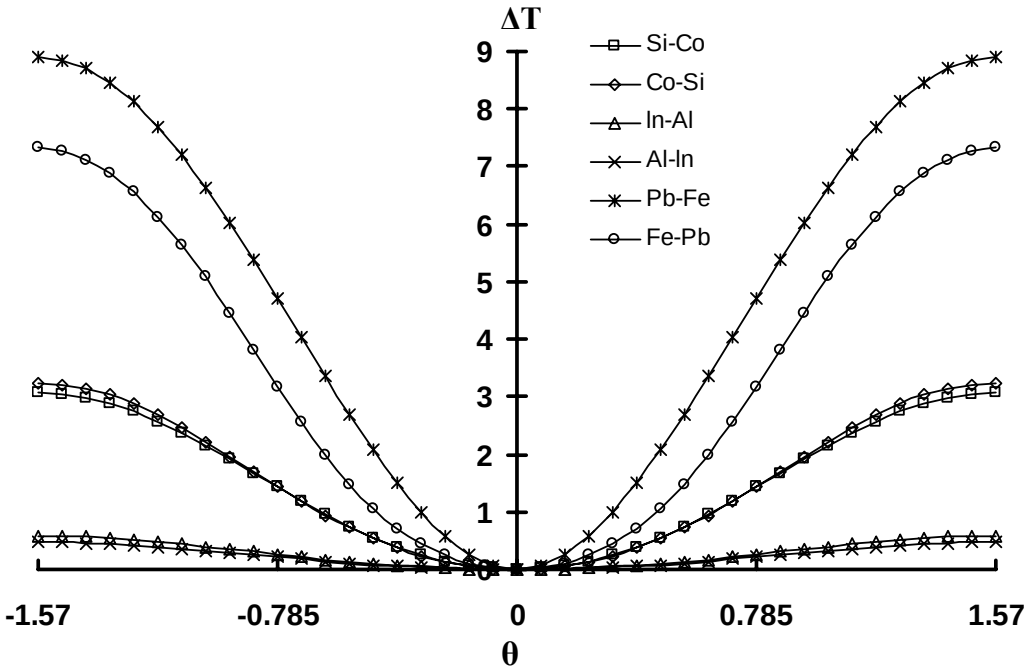

(b)

Figure 6.4 Steady state temperature distribution ($\Delta T = T-T_{smin}$, where T_{smin} is the minimum surface temperature) along the free surface (a) and the interface between the

two immiscible liquid metals (b). The surface is measured from south ($\theta = -\pi/2$) to north ($\theta = \pi/2$) pole.

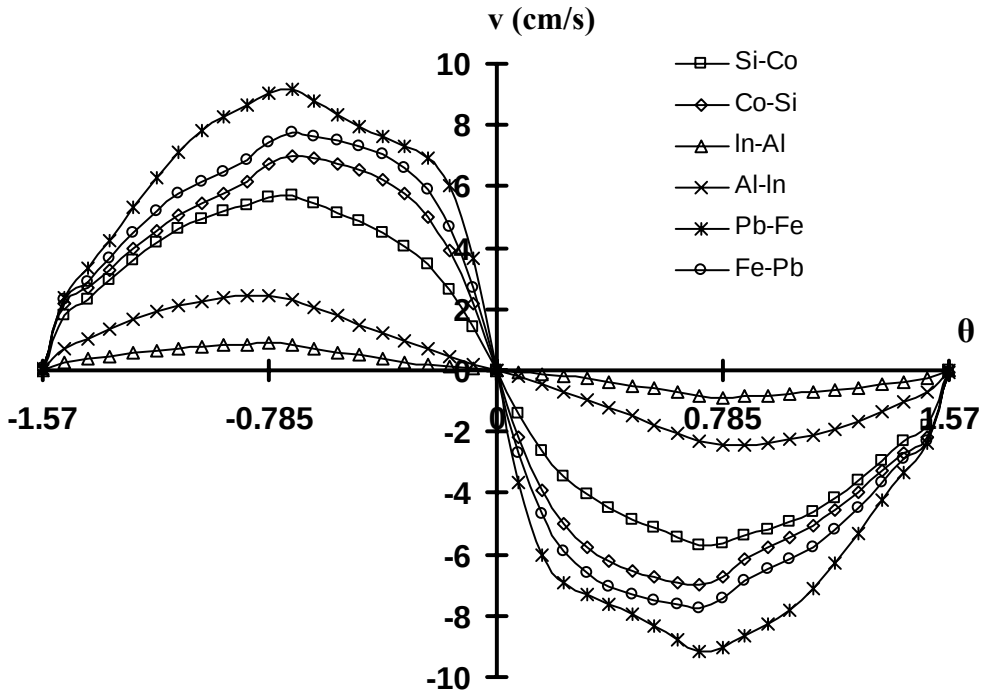

(a)

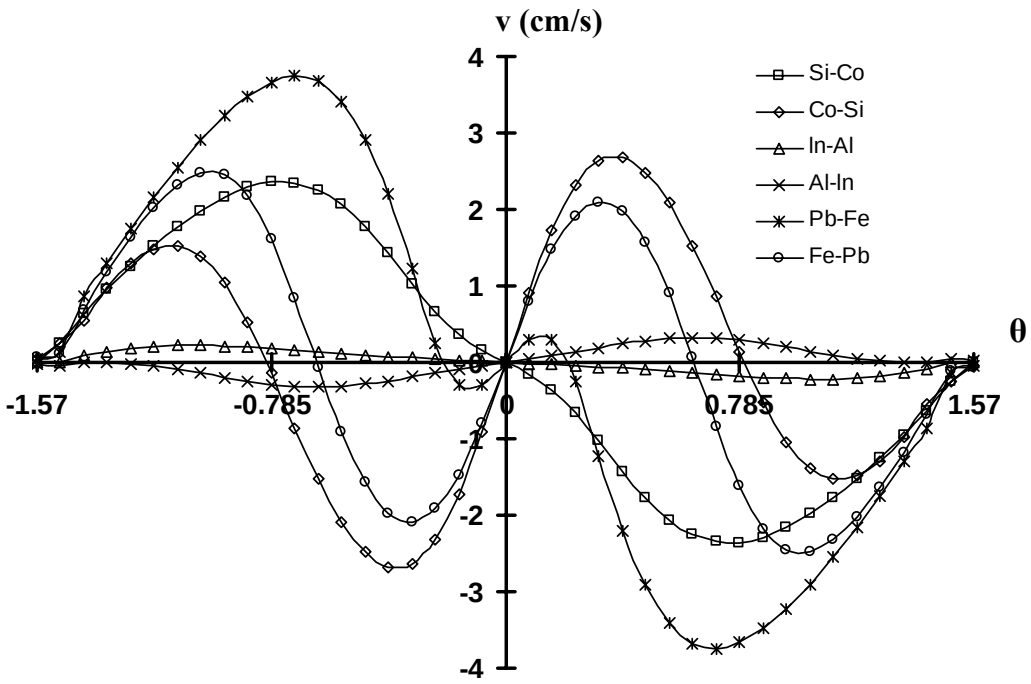

(b)

Figure 6.5 Steady state fluid flow distribution along the free surface boundary (a) and the interface between the two immiscible liquid metals (b). The angle θ is measured from (θ = -π/2) to (θ = π/2). The velocity is positive in the clockwise direction and negative in the anti-clockwise direction

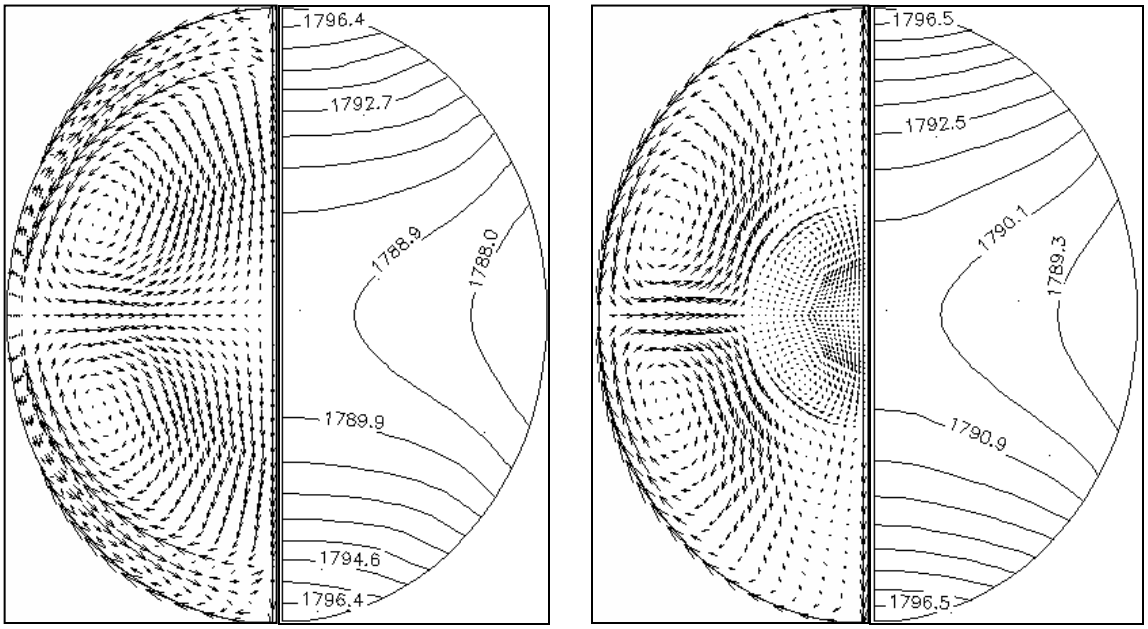

(a) $r_i / r_o = 0.9$ (b) $r_i / r_o = 0.4$

Figure 6.6 Steady-state fluid flow and temperature distribution in the Si-Co droplet with different radius ratios

6.2.3 Evolution of fluid flow and temperature fields

Knowledge of the decay of both temperature and velocity fields in a levitated droplet of the immiscible metals, as it cools into an undercooling region, is crucial for the design of microgravity experiments with the droplet. In practice, when the levitation is stabilized

and the sample is heated to a desired temperature, the laser beams are turned off and the sample is allowed to cool below the melting point of one of the two fluids by radiation. The computational methodology discussed above may be applied to predict the dynamic development of transient thermal and fluid flow fields in electrostatically positioned droplets as they undergo undercooling. The Pb-Fe droplets are selected for discussion in this study, and the analysis should be applicable to other cases well.

Fig. 6.7 illustrates a set of snap shots of the time evolving velocity and temperature fields in the Pb-Fe droplet when the laser power is switched off and the droplet is allowed to cool for about 3 seconds. At this point, the temperature drops below the melting point of iron. The calculations began with the initial (t=0) velocity and temperature fields shown in Fig. 6.3 (d). The time development of the detailed temperature and velocity distributions both along the free surface and the immiscible interface are shown in Figs. 6.8 and 6.9. The two-fold symmetry with respect to the equator plane is apparently a consequence of the initial fields and thus does not need an elaboration.

Cross-examination of Figs. 6.7 to 6.9 reveals some of most interesting features associated with this complex evolving thermal and fluid flow phenomena as the droplet cools into the undercooling region. First, the temperature drops very rapidly over t=0 to t=0.1 (sec) after the laser power is turned off and the decrease continues afterwards but at a slower pace. At t = 0.1 (sec), the outer surface temperature difference at the pole ($\theta=\pm\pi/2$) has decreased by about 30 times, which compares with a factor of 5 for a drop in the inner temperature difference at $\theta=\pm\pi/2$ (also see Fig. 6.4). On the free surface, the temperature gradient is completely reversed at about 0.2 (sec) in that the temperature at

the pole becomes smaller than that at the equator. In comparison, the reversal takes about 0.3 (sec) along the immiscible interface. After the reversal completes, the temperature gradient direction remains the same along both the free surface and the interface. Again, this dynamic evolution of the thermal field is by conduction and surface radiation, and the convection effect is relatively weak or minimal, as evident by the small Prandlt number of the melts. As thermal radiation is stronger near the pole where temperature is high, the temperature reversal starts there. This change in the thermal field is responsible for the complex evolving fluid flow field in the droplet, as shown in Fig. 6.7.

Fig. 6.7a shows that at t=0.1 (sec), the four-loop structure remains unchanged despite a significant drop in temperature. This is because the surface tension force gradient is unchanged. The large drop in the temperature, however, is reflected in the velocity magnitude, as is evident by comparing Fig. 6.6 and Fig. 6.9, where the velocity distribution along the free and inter surfaces are plotted. At some time close to t=0.2 (sec), the temperature gradient along the free surface is reversed such that the temperature at the equator plane becomes higher than that at the pole. This change in temperature gradient causes a corresponding reversal of the surface tension force gradient, with a higher pulling force now at the pole. Consequently, the fluid stream along the free surface flows from the equator plane to the poles (see Fig. 6.7b), which causes the outer fluid eddy near the equator to reverse its rotation. At this point, however, the interfacial surface force gradient still is the same as before, and intends to drive the flow from the pole to the equator region. Thus, in the near interfacial region, the outer flow inertia force complements the interfacial surface force gradient, thereby giving rise to the fluid pattern as shown in Fig. 6.7b. As the evolution continues, the interface gradually completes its

temperature reversal. Then the inertia force starts competing with the interface surface force in driving the fluid flow near the interfacial region. Figs. 6.7c and 6.7d reveal that the outer flow inertia force becomes more powerful from t = 0.3 (sec) onwards and drives the flow near the immiscible interface region. This means that the flow in both the immiscible fluids of the droplet comes primarily from the free surface Marangoni effect and the interfacial surface force has a negligible role.

6.3 **Concluding remarks**

This chapter has presented a numerical study of the free surface deformation and Marangoni convection in immiscible droplets electrostatically positioned under microgravity. The computational methodology employs the boundary element method for the solution of the electrostatic field outside the conducting droplet and couples with the weighted residuals method for solving the unknown free surface shapes along the free surfaces. With the droplet fee surface shapes determined, the temperature and fluid flow fields are solved using the Galerkin finite element method. Both the transient and steady state thermal and fluid flow fields are solved, with the implicit backward Euler scheme used for the time matching. Analyses show that the inner interface demarking the two immiscible fluids in an electrically conducting droplet is immune to the applied electrostatic field and maintains its sphericity in microgravity. The free surface or the outer surface, however, deforms into an oval shape and its equilibrium shape is determined by the balance of the Maxwell stress and the surface tension. The deformation is caused by the pulling action of the electric forces resulting from the interaction of the

induced charges and the applied electric field. The thermal and fluid flow distributions are rather complex in an immiscible droplet. The dominant mechanism for thermal transport in the droplet is heat conduction and convection plays only a minor role. The flow near the free surface is driven by the well-known Marangoni convection mechanism, which causes the fluid particle to move from the high to low temperature regions. The flow inside the inner fluid and near the immiscible interface, however, is driven by a competing mechanism between the thermally induced interfacial surface tension gradient and the inertia force in the outer fluid layer induced by the free surface Marangoni convection. During cooling into an undercooled state after the laser hearting is switched, the surface temperature gradients, both along the free surface and the immiscible interface, experience a reversal, which is caused by surface radiation. This reversal in the temperature gradients results in a reversal of the surface flow. During the time between the surface thermal gradient reversals along the free and the interfacial surfaces, the flow near the interfacial region may be driven by a complimentary mechanism between the interfacial and the inertia forces during the thermal and fluid flow transitional period. Before and after the completion of the interfacial thermal gradient reversal, however, the interfacial flows are driven by the competing mechanism between the interfacial and inertia forces, with the latter overwhelmingly dominating after the thermal reversal is completed along both the free and interfacial surfaces.

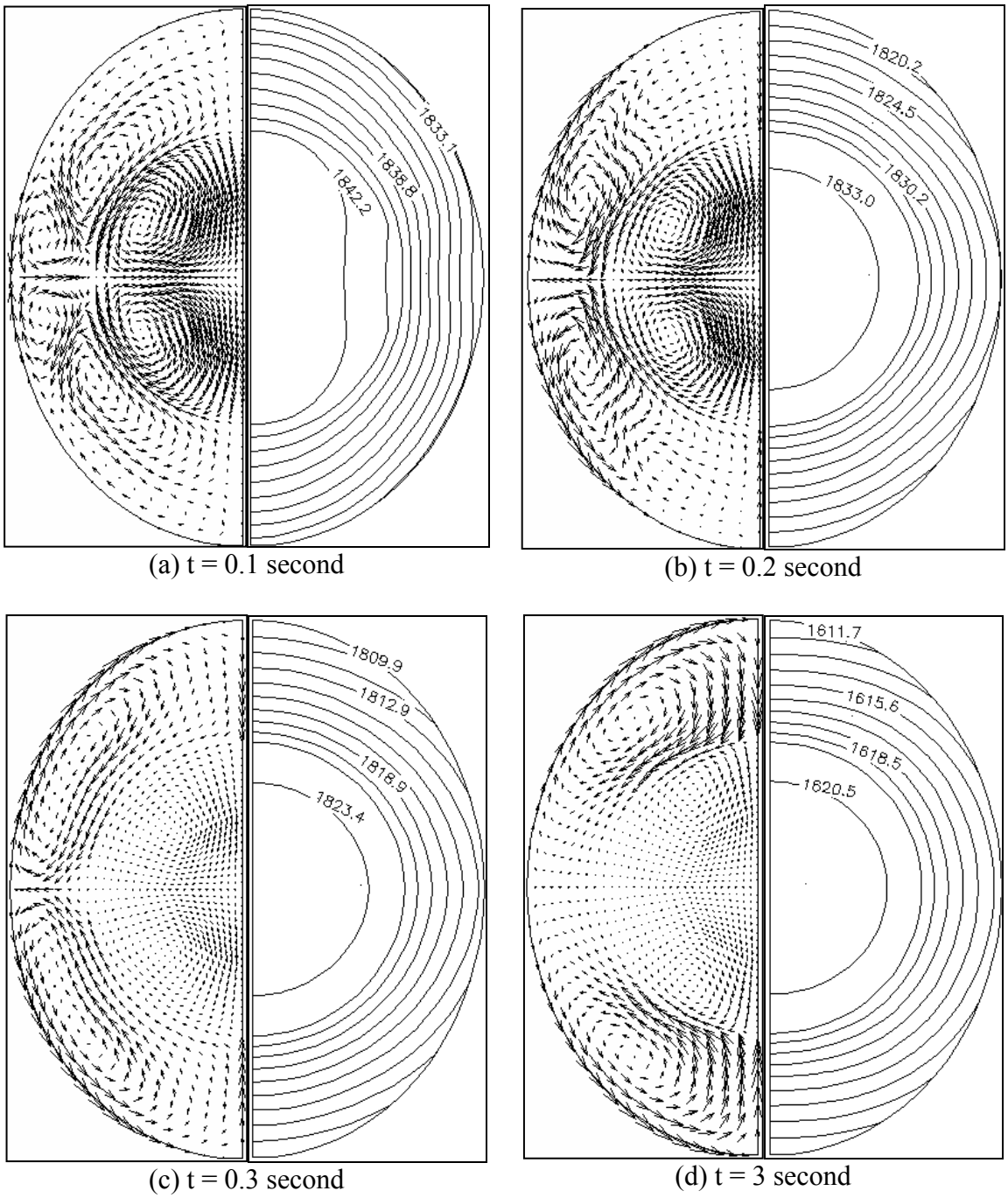

(a) t = 0.1 second (b) t = 0.2 second

(c) t = 0.3 second (d) t = 3 second

Figure 6.7 Transient fluid flow and temperature distributions in a Pb-Fe droplet after the heating lasers are turned off.

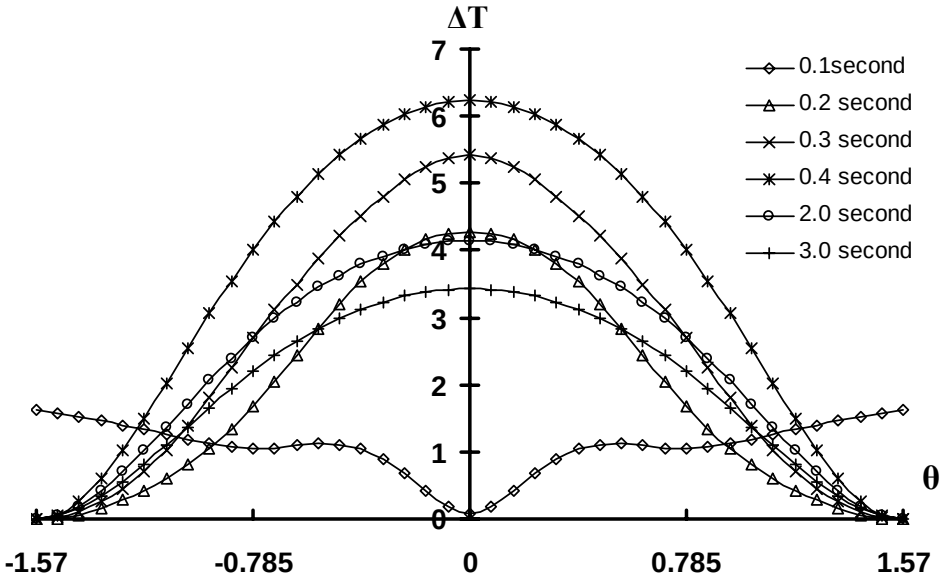

(a)

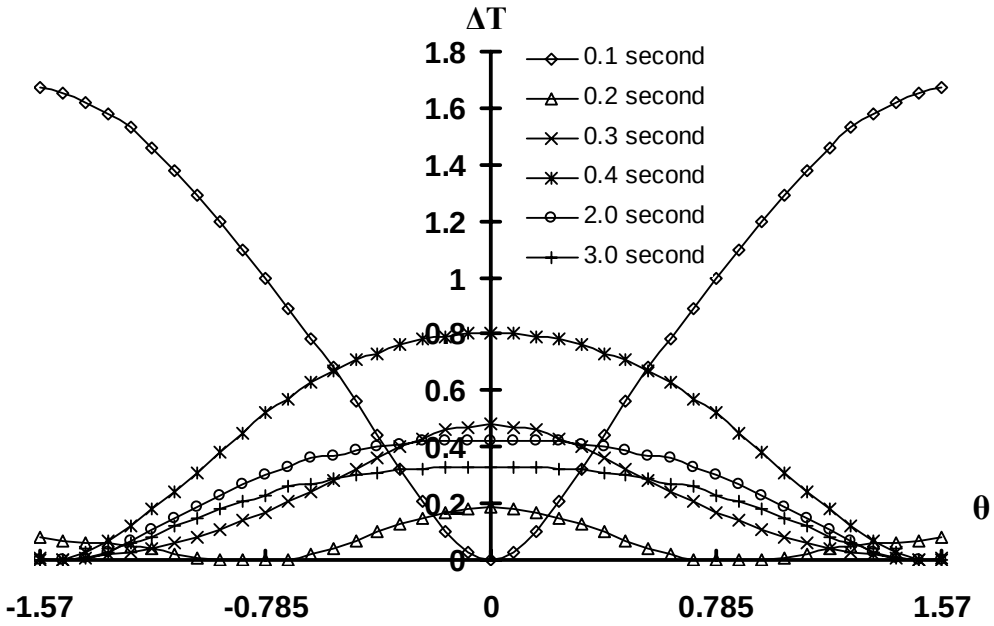

(b)

Figure 6.8 Transient temperature distribution ($\Delta T = T-T_{min}$) along the surface from ($\theta = -\pi/2$) to ($\theta = \pi/2$): (a) free surface and (b) the immiscible interface (Pb-Fe).

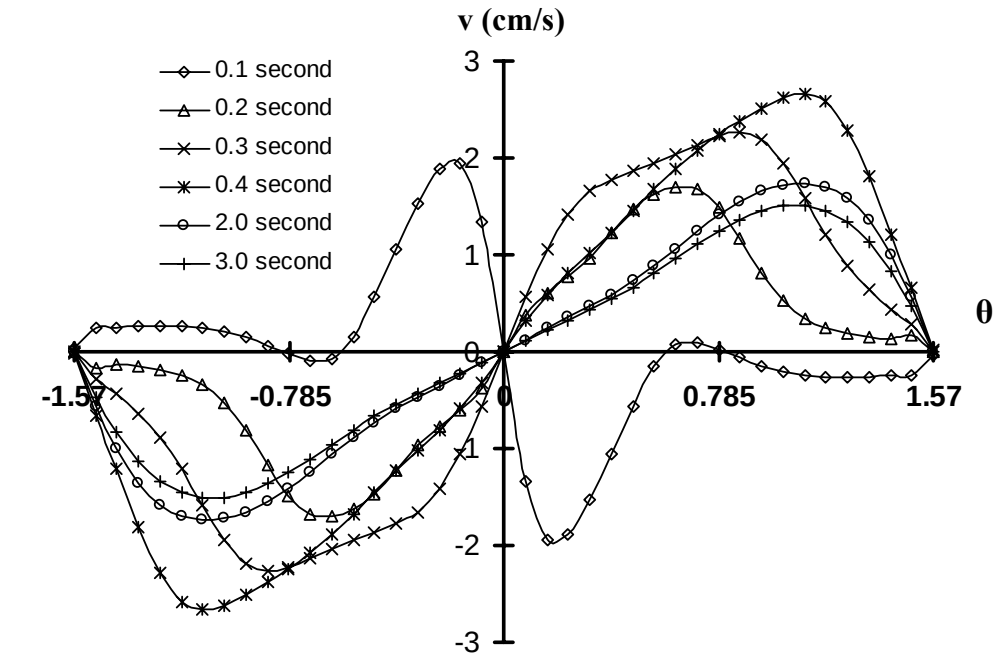

(a)

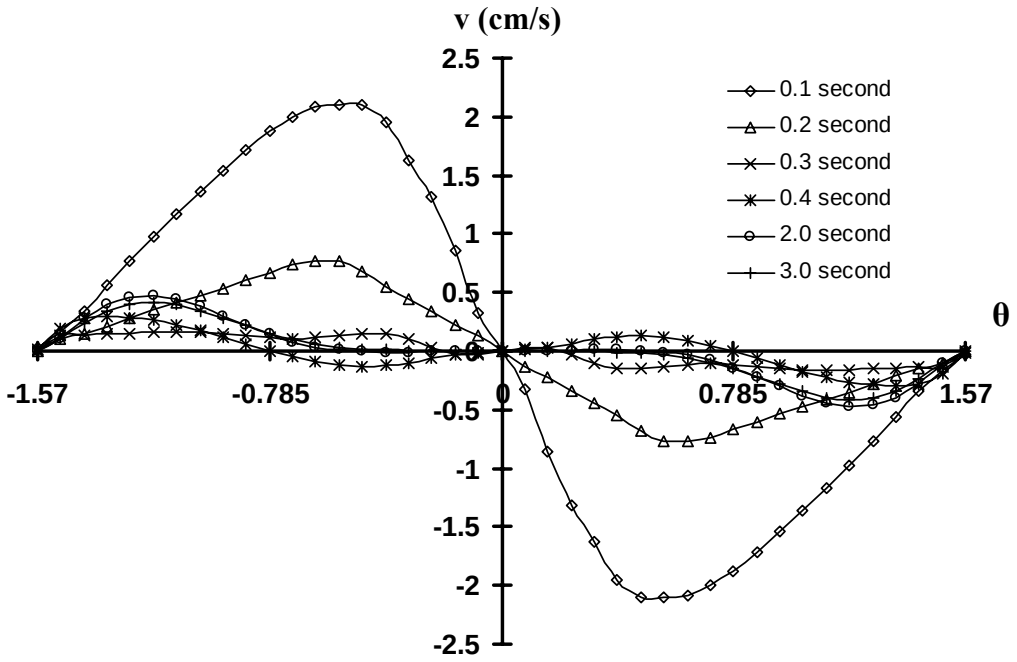

(b)

Figure 6.9 Transient fluid flow distribution along the surface from ($\theta = -\pi/2$) to ($\theta = \pi/2$): (a) free surface and (b) the immiscible interface (Pb-Fe). The velocity is positive in the clockwise direction and negative in the anti-clockwise direction

CHAPTER 7

2-D FEM/BEM SIMULATION OF THE OSCILLATION OF THE ELECTROSTATICALLY LEVITATED DROPLET

7.1 Introduction

In this chapter, a mathematical model is developed for the oscillation of the electrostatically levitated droplet under microgravity. The computational methodology entails solving the Laplace equation by the boundary element method, solving the Navier-Stokes equations by the Galerkin finite element method, and the use of deforming elements to track the oscillating free surface shapes. The pressure-velocity formulation is used in the finite element model for the internal fluid flow. To incorporate the free surface kinematical boundary condition, the front tracking technique is applied. The electric fields, surface driven flow fields and deformed surface shapes are calculated iteratively for each time step during drop oscillation. Computed results are presented for both free surface oscillations and internal fluid flows in electrostatically positioned droplets in microgravity environment. The effect of both the electric field and the surface tension on the frequency of the oscillation is studied. The effect of the viscosity on the damping constant is also analyzed.

7.2 Problem Statement

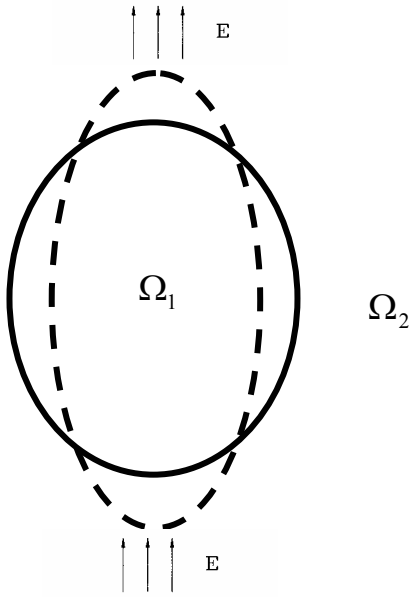

Figure 7.1 Schematic representation of an initial (dash line) and steady-state for the computation of the electrostatically levitated droplet

Figure 7.1 shows the initial and steady state positions in the oscillation of the electrostatically levitated droplets. A complete description of the electrically induced surface oscillation and pressure fluid flow phenomena in a droplet requires the solution of the coupled Maxwell and Navier-Stokes equations. At present, the Maxwell equation is simplified to a partial differential equation governing the distribution of the electric field outside the droplet. The buoyancy effects being neglected for microgravity applications, the equations for the electric and fluid flow may be written as follows,

$$\nabla^2 \Phi = 0 \qquad \in \Omega_2 \qquad (7.1)$$

$$\nabla \cdot \mathrm{u} = 0 \qquad \in \Omega_1 \qquad (7.2)$$

$$\rho\frac{\partial \mathrm{u}}{\partial t}+\rho\mathrm{u}\cdot\nabla\mathrm{u}=-\nabla p\ +\nabla\cdot\eta\left(\nabla\mathrm{u}+(\nabla\mathrm{u})^{T}\right)+F_{surface} \qquad \in\Omega_1 \qquad (7.3)$$

The solution of above electric field and fluid flow equations may be obtained by applying the appropriate boundary conditions, which are stated below

$$\Phi=\Phi_0 \qquad \in\Omega_1\cap\Omega_2 \qquad (7.4)$$

$$\varepsilon_0\mathbf{n}\cdot\nabla\Phi=-\sigma_e \qquad \in\Omega_1\cap\Omega_2 \qquad (7.5)$$

$$\oiint_{\partial\Omega_1}\sigma_e ds=-\oiint_{\partial\Omega_1}\varepsilon_0\mathbf{n}\cdot\nabla\Phi ds=Q \qquad \in\Omega_1\cap\Omega_2 \qquad (7.6)$$

$$\Phi=-E_0R\cos\theta \qquad R\to\infty \qquad (7.7)$$

$$F_{surface}=\mathbf{n}\cdot\bar{\sigma}\cdot\mathbf{n}-\mathbf{n}\cdot\mathbf{T}_E\cdot\mathbf{n} \qquad \in\Omega_1\cap\Omega_2 \qquad (7.8)$$

$$\mathbf{n}\cdot\bar{\sigma}\cdot\mathbf{n}=2H\gamma \qquad \in\Omega_1\cap\Omega_2 \qquad (7.9)$$

$$\mathbf{T}_E=\frac{1}{2}\varepsilon\nabla^2\Phi \qquad \in\Omega_1\cap\Omega_2 \qquad (7.10)$$

$$\frac{\mathrm{dX}}{\mathrm{dt}}+\mathrm{u}\cdot\nabla\mathrm{X}=0 \qquad \in\Omega_1\cap\Omega_2 \qquad (7.11)$$

$$\int_{\Omega_1}dV=V_0 \qquad \in\Omega_1\cap\Omega_2 \qquad (7.12)$$

$$\int_{\Omega_1}z dV=z_c \qquad \in\Omega_1\cap\Omega_2 \qquad (7.13)$$

In the above, Eq. (7.5) is the jump condition for the electric field along the droplet surface, a manifestation of a well known fact that charges are distributed only on the surface of a conducting body. Eq. (7.7) describes the electric potential condition at

infinity. The law of charge conservation is described by Eq. (7.6), where Q is the total free charge applied on the droplet, which is zero for the problem under consideration for microgravity applications. Eq. (7.8) describes the force induced by the Maxwell and surface tension stresses along the normal direction. In Eq. (7.9), $\overline{\sigma}$ is the stress tensor, γ is the surface tension and H is the Gaussian mean curvature. Eq. (7.10) describes the Maxwell stress associated with the electric potential. Eq. (7.11) is the kinematic condition, which describes the interface, represented by the $X(x_i,t)=0$ always remains an interface. The constraints of the volume conservation (Eq. (7.12)) and the center of the mass (Eq. (7.13)) of the electrostatically levitated droplet are needed to determine the shape and position of the droplet.

7.3 Method of Solution

7.3.1 BEM solution of the electric potential

The numerical solution of the electric potential equation (Laplace equation) along the free surface boundary conditions is obtained by applying the BEM. We are seeking an approximate solution to the problem governed by Eq. (7.1). The error introduced by replacing Φ by an approximate solution can be minimized by writing the following weighted residual statement:

$$\int_{\Omega_2} \nabla^2 \Phi(r) G(r_i, r) d\Omega(r) = \int_{\Gamma} q(r) G(r_i, r) d\Gamma(r) - \int_{\Gamma} \Phi(r) q^*(r_i, r) d\Gamma(r) \qquad (7.14)$$

where G is interpreted as a weighting function and

$$q^*(r_i, r) = \frac{\partial G(r_i, r)}{\partial n(r)} \tag{7.15}$$

After some transformation, we can get the final form used for the BEM simulation.

$$\begin{aligned} &C(r_i)\Phi'(r_i) + \oint_{\partial\Omega_2} \Phi'(\mathbf{n}\cdot\nabla G) r d\Gamma + \oint_{\partial\overline{\Omega}_2} \Phi'(\mathbf{n}\cdot\nabla G) r d\Gamma = \\ &\oint_{\partial\Omega_2} G(\mathbf{n}\cdot\nabla\Phi') r d\Gamma + \oint_{\partial\overline{\Omega}_2} G(\mathbf{n}\cdot\nabla\Phi') r d\Gamma \end{aligned} \tag{7.16}$$

where

$$C(r_i) = \begin{cases} 1; & \text{when } r_i \text{ lies inside domain} \\ \dfrac{1}{2}; & \text{when } r_i \text{ lies on a smooth domain} \\ \dfrac{2\pi - \beta_1 - \beta_2}{2\pi}; & \text{when } r_i \text{ lies on a nonsmooth domain} \end{cases}$$

and $\Phi' = \Phi + Er\cos\theta$, $\partial\Omega_2$ designates the surface of the droplet and $\partial\overline{\Omega}_2$ denotes the boundary at infinity. The Green function, G, and its normal derivative are calculated by the following expressions written for a cylindrical coordinate system [Jackson, 1975].

$$G(r_i, r) = \frac{4}{\sqrt{(r_i + r)^2 + (z - z_i)^2}} K(\kappa) \tag{7.17}$$

$$\frac{\partial G}{\partial n} = \frac{4}{\sqrt{(r+r_i)^2+(z-z_i)^2}} \left\{ \begin{array}{l} \frac{n_r}{2r}\left[E(\kappa)-K(\kappa)\right]- \\ \frac{n_r(r-r_i)+n_z(z-z_i)}{(r-r_i)^2+(z-z_i)^2}E(\kappa) \end{array} \right\} \tag{7.18}$$

where κ is the geometric parameter calculated by

$$\kappa^2 = \frac{4r_i r}{(r_i+r)^2+(z_i-z)^2} \tag{7.19}$$

The function G and Φ' have the following asymptotic properties,

$$\Phi'(r_i,R) \approx O(R^{-2}), \quad \frac{\partial \Phi'}{\partial n}(r_i,R) \approx O(R^{-3}) \text{ as } R \to \infty \tag{7.20}$$

$$G(r_i,R) \approx O(R^{-2}), \quad \frac{\partial G}{\partial n}(r_i,R) \approx O(R^{-3}) \text{ as } R \to \infty \tag{7.21}$$

Also $d\Gamma = R(\theta)\, d\theta$. Thus, the two integrals each approach zero as $R \to \infty$,

$$\oint_{\partial\Omega_2} \Phi'(\mathbf{n}\cdot\nabla G) r d\Gamma \to 0 \text{ and } \oint_{\partial\Omega_2} G(\mathbf{n}\cdot\nabla\Phi') r d\Gamma \to 0 \text{ as } R \to \infty \tag{7.22}$$

Thus, Eq. (7.16) simplifies to a boundary integral that involves only the surface of the droplet, $\partial\Omega_2$. Following the standard boundary element discretization, noticing that the potential on the surface is a constant and substituting $\Phi = \Phi' - Er\cos\theta$ into the resultant

equation, one obtains the final matrix form for the unknowns on the surface of the droplet,

$$\mathbf{H}\{\Phi_0\} = -\mathbf{G}\left\{\frac{\partial \Phi}{\partial n}\right\} + E\mathbf{G}\left\{\frac{\partial z}{\partial n}\right\} - \mathbf{H}E\{z\} \tag{7.23}$$

where **H** and **G** are the coefficient matrices involving the integration of $\partial G/\partial n$ and G over a boundary element. To complete the solution, Eq. (7.6) is discretized and solved along with the above equation to obtain the surface distribution of $\partial\Phi/\partial$n and the constant Φ_0.

7.3.2 FEM solution of the fluid flow and free surface movement

The transport equations for the internal fluid flow along with the boundary conditions are solved using the Galerkin finite element method. The continuity and N-S equations with the pressure-velocity formulation can be discretized as follows,

$$\left(\int_{\Omega_1} \psi(\hat{i}\cdot\nabla\phi^T + \delta_{2i}\phi^T/r)d\Omega\right)\mathrm{U}^i = 0 \tag{7.24}$$

$$\left(\int_{\Omega_1} \rho\phi\phi^T d\Omega\right)\frac{\partial \mathrm{U}^i}{\partial t} + \left(\int_{\Omega_1} \rho\phi\mathrm{u}\cdot\nabla\phi^T d\Omega\right)\mathrm{U}^i - \left(\int_{\Omega_1} (\hat{i}\cdot\nabla\phi + \delta_{2i}\phi/r)\psi^T d\Omega\right)\mathrm{P} +$$
$$\left(\int_{\Omega_1} \eta(\nabla\phi\cdot\nabla\phi^T + 2\delta_{2i}\phi\cdot\phi^T/r^2)d\Omega\right)\mathrm{U}^i + \left(\int_{\Omega_1} \eta(\hat{i}\cdot\nabla\phi)(\hat{j}\cdot\nabla\phi^T)d\Omega\right)\mathrm{U}^i = \tag{7.25}$$
$$\int_{\partial\Omega_1} \mathrm{n}\cdot\bar{\sigma}\cdot\hat{i}\,\phi d\Gamma - \int_{\partial\Omega_1} \mathrm{n}\cdot T_E\cdot\hat{i}\,\phi d\Gamma$$

where U is a global vector containing all nodes values of u and v, and P the global vector containing the nodal values of pressure. Once the form of the shape functions is specified, the integrals defined in the above equations can be calculated numerically. It is noted that the selection of the shape functions must satisfy Babuska-Brezzi condition. The discretized momentum and energy equations may be combined into a single global matrix equation,

$$\begin{bmatrix} \mathrm{M} & 0 \\ 0 & 0 \end{bmatrix} \begin{bmatrix} \dot{\mathrm{U}} \\ \dot{\mathrm{P}} \end{bmatrix} + \begin{bmatrix} \mathrm{A(U)+K} & -\mathrm{C} \\ -\mathrm{C}^{\mathrm{T}} & 0 \end{bmatrix} \begin{bmatrix} \mathrm{U} \\ \mathrm{P} \end{bmatrix} = \begin{bmatrix} \mathrm{F} \\ 0 \end{bmatrix} \tag{7.26}$$

where the coefficient matrices in the above equation are defined by,

$$\mathrm{M} = \int_{\Omega_1} \rho\phi\phi^T d\Omega ; \qquad C_j = \int_{\Omega_1} (\hat{j}\cdot\nabla\phi + \delta_{2j}\phi/r)\psi^T d\Omega ;$$

$$\mathrm{A(U)} = \int_{\Omega_1} \rho\phi \mathrm{u}\cdot\nabla\phi^T d\Omega ; \qquad \mathrm{F}_i = \int_{\partial\Omega_1} \mathrm{n}\cdot\overline{\sigma}\cdot\hat{i}\,\phi d\Gamma - \int_{\partial\Omega_1} \mathrm{n}\cdot T_E\cdot\hat{i}\,\phi d\Gamma ;$$

$$\mathrm{K}_{ij} = \left(\int_{\Omega_1} \eta(\nabla\phi\cdot\nabla\phi^T + 2\delta_{2i}\phi\cdot\phi^T/r^2) d\Omega \right)\delta_{ij} + \left(\int_{\Omega_1} \eta(\hat{i}\cdot\nabla\phi)(\hat{j}\cdot\nabla\phi^T) d\Omega \right)$$

where j = 1, 2 and δ_{ij} is a delta function. The assembled global matrix equations are stored in the skyline form and solved using the Gaussian elimination method. For free surface problem, F has a contribution from the normal stress balance, which my be further simplified by the theorem of differential geometry.

$$\oint_{\Gamma_f} \phi_k \mathrm{n} \cdot \bar{\sigma} \cdot \mathrm{n} d\Gamma = \oint_{\Gamma_f} \phi_k \gamma H d\Gamma = \oint_{\Gamma_f} \phi_k \nabla_S \cdot \mathrm{n} d\Gamma = -\oint_{\Gamma_f} \nabla_S \phi_k \cdot \mathrm{n} d\Gamma + \oint_{\partial\Gamma_f} \phi_k \mathrm{m} \cdot \mathrm{n} d\Gamma \qquad (7.27)$$

where ∇_S is the surface gradient operator, Γ_f is the free surface or boundary, $\partial\Gamma_f$ is the bounding curve for the free surface and m is the normal to $\partial\Gamma_f$ but tangential to Γ_f.

To incorporate the free surface kinematric boundary condition, the front tracking technique is applied, By this techniques, the nodes along the free surface are allowed to move such that they remain on the oscillating surface all the time. Thus, Eq. (7.12) can be solved using the Weighted Residuals Methods (WRM) with the result,

$$\int_{\Gamma_f} \chi \left(\frac{\mathrm{dX}}{\mathrm{dt}} + \mathrm{u} \cdot \nabla \mathrm{X}\right) d\Gamma = 0 \qquad (7.28)$$

where χ is the shape function for the free surface coordinates. Discretization, followed by numerical integration and assembly, gives rise to the following matrix equation,

$$\hat{\mathrm{M}}\dot{\mathrm{X}} + \hat{\mathrm{K}}\mathrm{X} = 0 \qquad (7.29)$$

where $\hat{\mathrm{M}}$ and $\hat{\mathrm{K}}$ are global matrices for free surface coordinates. Because the nodes of the free surface are allowed to move to satisfy Eq. (7.29), these movement must be superimposed on the velocity at the nodal points and therefore the convection term in Eq.

(7.3) must be modified accordingly, that is, $\rho \mathrm{u} \cdot \nabla \mathrm{u}$ is replaced by $\rho(\mathrm{u}+\mathrm{u}_s) \cdot \nabla \mathrm{u}$ where u_s is the nodal velocity due to the free surface movement.

7.3.3 Numerical procedures

The solution of the above equations defining the droplet oscillation in the electrostatic levitation mechanism requires an iterative procedure. The required nonlinear iterations are preformed using the successive substitution scheme method. The time derivatives are approximated by the implicit finite difference scheme, with automatic time step control. The iterative procedure starts with an initial condition for the free surface shape. With the initial condition, the electric potential on the free surface is calculated by using BEM. The fluid flow is then calculated with the updated Maxwell stress and the free surface coordinates. The updated free surface is used to start another set of calculations for the updated electric potential. The iterative procedure continues until all of the variables converge within a preset tolerance. The convergence criterion for the calculations is set such that the relative error between the two consecutive iterations is within 1×10^{-4}.

7.4 Analytical Solutions from Other Researchers

Lord Rayleigh (1882) first derived the formula $f_0 = (2\gamma/\pi^2 a^3 \rho)^{\frac{1}{2}}$ for the fundamental vibrational frequency, where a is the radius of the droplet, ρ the density of the droplet, and γ the surface tension. Experimental studies showed that the fundamental vibrational frequency agreed well with the formula derived by Lord Rayleigh. Taylor

(1964) demonstrated that the equilibrium drop shape was aspherical and might be approximated by a prolate spheroid. In his study, the equilibrium equations were satisfied at the poles and the equator. For the droplet in a uniform electric field E_0, Taylor derived the following formulation,

$$E_0 a^{\frac{1}{2}} \gamma^{-\frac{1}{2}} = (8\pi)^{\frac{1}{2}} M(\alpha) I \tag{7.30}$$

where

$$M(\alpha) = \alpha^{\frac{2}{3}} (2 - \alpha^{\frac{1}{2}} - \alpha^{\frac{3}{2}})^{\frac{1}{2}};$$

$$\alpha = (a_l / a_s)^2$$

where a_l is the semi-major axis and a_s is the semi-minor axis for prolate spheroid as $x^2/a_l^2 + y^2/a_s^2 = 1$. He concluded that the onset of instability occurs when $E_0 (R/\gamma)^{1/2} = 1.625$ and the deformation, expressed as the ratio a_l / a_s of the semi-major and semi-minor axis of the drop is equal to 1.86.

Based on the assumption of spheroidal oscillatory shapes, the characteristic frequency of the two-lobed mode for an uncharged conducting drop in a uniform electric field was shown to decrease as the applied electric field strength increases [Rosenkilde 1969; Brazier-Smith et al. 1917]. In Smith's study, the fundamental frequency of an uncharged drop in a uniform electric field may be written as follows,

$$f = \frac{1}{\pi}\left(\frac{2\gamma x}{r^3 \rho}\right)^{\frac{1}{2}} \tag{7.31}$$

where

$$x = \frac{\frac{17\alpha^{-2}}{8} + \frac{11}{8} - 2\alpha - \frac{e^{-4}\alpha^{-2}}{2I}\left[\frac{9}{4e}\ln\left(\frac{1+e}{1-e}\right) - \frac{3}{2(1-e^2)} - 3\right](2\alpha - a^{-2} - 1)}{\alpha + (1/2\alpha)}$$

$$\alpha = (a_l / a_s)^2$$

$$e = \left(1 - \left(\frac{a_s}{a_l}\right)^2\right)^{\frac{1}{2}}$$

Therefore, we can find the relation between frequency f and surface tension γ. Since the relation between α and E_0 is known, as shown in Eq. (7.30), the variation of f with E_0 can be found.

Later on, the equilibrium shapes and the stability of a charged conducting drop levitated by a uniform electric field were analyzed by Adornato and Brown (1983) whose asymptotic and numerical analysis for the equilibrium drop shape in small electric fields showed the appearance of second and third Legendre functions. Feng and Beard (1990) further studied the nature of the axisymmetric oscillation of electrostatically levitated droplets by using an analytic multiple parameter perturbation method. In Feng and Bear's study, the oscillatory response at each frequency consists of several Legendre

Polynomials rather than just one, and the characteristic frequency for each axisymmetric mode decreases from that calculated by Rayleigh for stronger applied electric field. Feng and Beard's frequency correction term for axisymmetric n=2 may be written as,

$$f^2 = f_0^2[1 - F(\gamma, q, e)] \tag{7.32}$$

where

$$F(\gamma, q, e) = \frac{(243.31\gamma^2 - 63.14q^2\gamma + 1.54q^4)e^2}{176\gamma^3 - 120q^2\gamma^2 + 27\gamma q^4 - 2q^6}$$

$$q^2 = \frac{Q_s^2}{16\pi^2 r^2 \varepsilon_0}$$

$$e^2 = E_0{}^2 r\varepsilon_0$$

Q_s is the electric charge induced into the droplet, E_0 is the uniform electric field, and ε_0 is the electric permittivity in the free space.

7.5 Numerical Results and Discussion

The computational methodology described above can be applied to predict the distribution of electric potential, free surface oscillation and viscous flow in the electrostatically positioned droplets. Because of limited space, a few computed results are presented here from extensive numerical simulations. The calculation used 20 quadratic

boundary elements in half-circle model to calculate the electric potential fields, while 175 9-node finite elements in the quarter-circle model were employed for the computation of fluid flow and free surface oscillations, as shown in Fig. 7.2. The criterion for the convergence of non-linear iteration is set to 1×10^{-4} (norm-2 relative error).

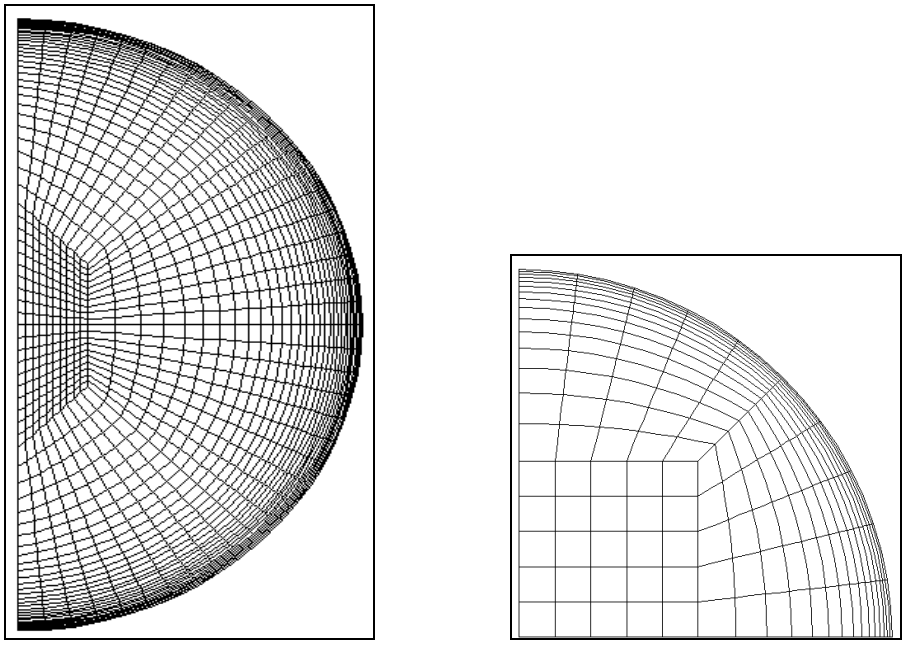

(a) (b)

Figure 7.2 Boundary element and finite element meshes: (a) boundary element mesh for the computation of the electric potential, (b) finite element mesh for the computation of the fluid flow and free surface oscillations

Since Lord Rayleigh (1882) first calculated the characteristic frequencies for small-amplitude oscillations of a charged drop in the absence of external fields about the spherical shape, the study of the droplet in the electric field has received a wide interesting. Most of the studies focus on the analytical method except that Adornato and

Brown (1983) used FEM compared with the analytical method to study the shape and stability of the droplet elevated in the uniform electric field. At present, we analyzed the oscillation of the droplet levitated in the uniform electric field by using the FE/BE method. Fig. 7.3 depicts three computed positions (initial, steady-state and the minimum) of the oscillation of a liquid Aluminum droplet in the uniform electric field (E_0=2.0×10^6 v/m), whose properties is shown Table 7.1. It is assumed that the droplet is kept the elongated prolate spheroid with $a = 2.5\times10^{-3}$ m, $a_l = 3.553\times10^{-3}$ m, $a_s = 2.07\times10^{-3}$ m, and $a_l / a_s = 1.716$ at the initial time. Therefore, the computed oscillation of the droplet levitated in the electric field is below the critical values derived by Taylor and satisfied with the stability condition. In the electrostatic levitation mechanism, the elongated spherical droplet is first dragged back to the steady state position along the axis direction by the surface tension with the velocity of the poles increasing and enlarged at the equator surface in order to satisfy the mass conservation. Then the droplet reaches the steady-state prolate spheroid form, as described in chapter 4. Because of the effect of the inertial force, the droplet will pass by the steady-state position. After passing by the steady-state position, the electric force is larger than the surface tension and the moving velocity of both poles is reduced, but it still keeps moving towards the center of the droplet. Finally, the poles of the droplet reach the closest position to the center of the droplet (the minimum position as shown in Fig. 7.3), in which position the surface tension has the minimum value and the Maxwell stress has the maximum value so that the deformation of the droplet will be reversed. In order to depict the effect of the hydrodynamic force, the velocity distribution of the large amplitude of the droplet in one period is shown in Fig. 7.4

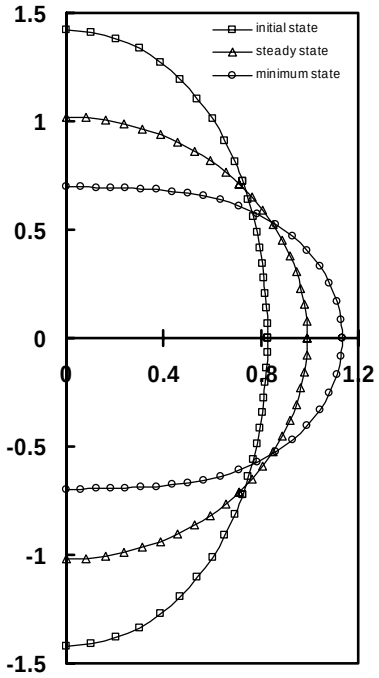

Figure 7.3 Three position of the droplet in half period of the oscillation of the droplet in the electric field (E_0=1.0×10^6 V/m)

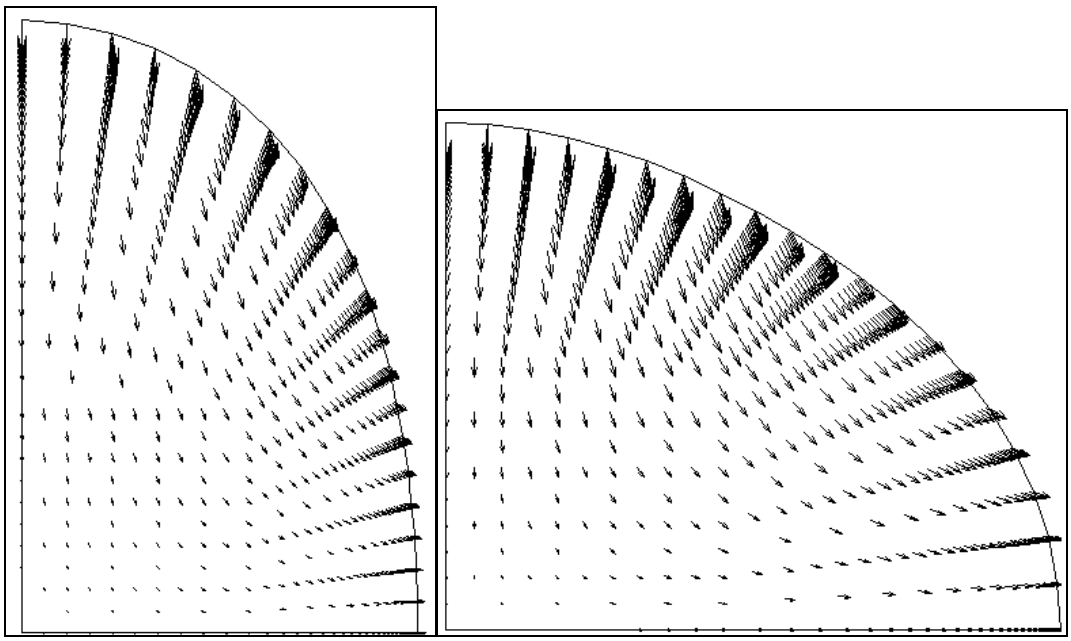

(a) t=1.9×10^{-3} s V_{max}=23.47 cm/s (b) t=5.8×10^{-3} s V_{max}=31.72 cm/s

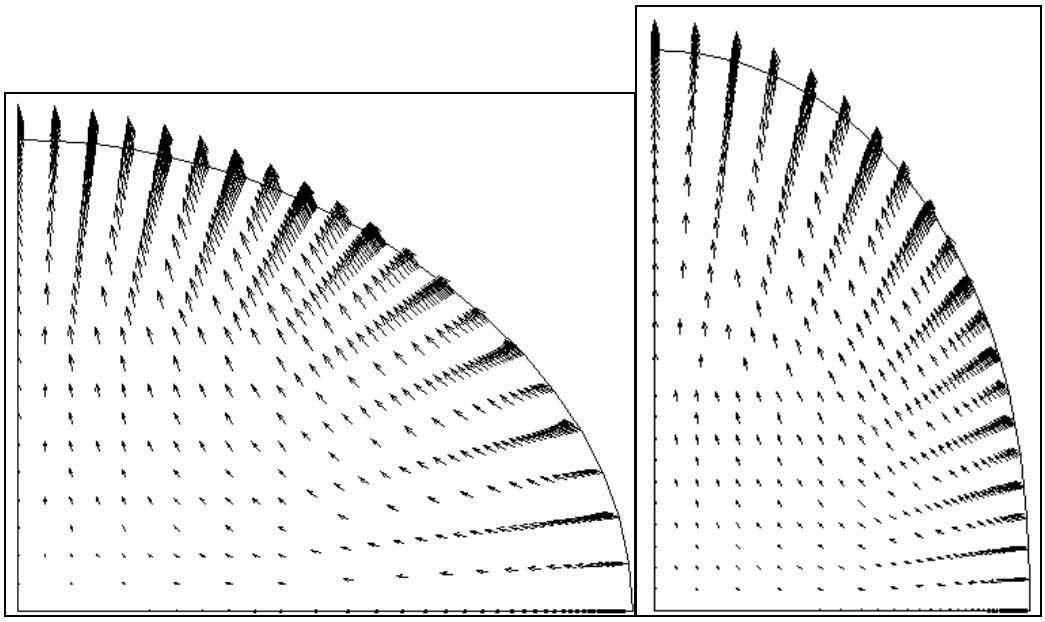

(c) $t=9.6\times10^{-3}$ s $V_{max}=31.00$ cm/s (d) $t=13.6\times10^{-3}$ s $V_{max}=24.96$ cm/s

Figure 7.4 Oscillation of an electrostatically levitated, aluminum droplet under microgravity conditions in one period, (a) 1/8 period, (b) 3/8 period, (c) 5/8 period, and (d) 7/8 period. The initial diameter of the droplet is 5 mm, $E_0=1.0\times10^6$ (V/m), the initial deformation of the droplet is like that in Fig. 7.3.

Parameters	Al
ρ (kg/m^3)	2385
$\mu \times 10^3$ (kg/m-s)	1.3
γ (N/m)	0.914
a (mm)	2.5

Table 7.1 Parameter used for the computation

Rosenkilde (1969) and Brazier-Smith *et al.* (1971b) found that the characteristic frequency of the two-lobed mode for an uncharged conducting droplet in a uniform electric field decreased as the applied electric field intensity increased. Feng and Beard (1990) also investigated the oscillation characteristics of electrostatically levitated droplets. In the present study, the effect of the frequency associated with variation of the electric field and surface tension is investigated. The computed results are first compared with Feng and Beard's analytical solution. Fig. 7.5 depicts the change of the normalized characteristic frequency of a conducting droplet with electrical field intensity. From Fig. 7.5, we can find that the frequency decreased with the electric field intensity becoming stronger. As shown in Fig. 7.5, the numerical results agree very well with the analytical prediction derived by Feng and Beard. The Maximum relative error is equal to 2.7%, which occurs when the electric field intensity reaches 2.1×10^6 (v/m). Fig. 7.6 shows the frequency of the oscillation of the droplet changes with the surface tension. The frequency of the droplet is increasing with the surface tension becoming larger. Compared with the Feng and Beard's results, the numerical results are good. However, the numerical curve is a little lower than the analytical curve in Fig. 7.6. The main reason is that the analytical solution only includes the major 2^{nd} mode and neglects the higher order modes. If the higher order Legendre polynomials are included, the formulation of the analytical method will become very complicated. Therefore, our numerical method may provide more accurate and fast results than the analytical method.

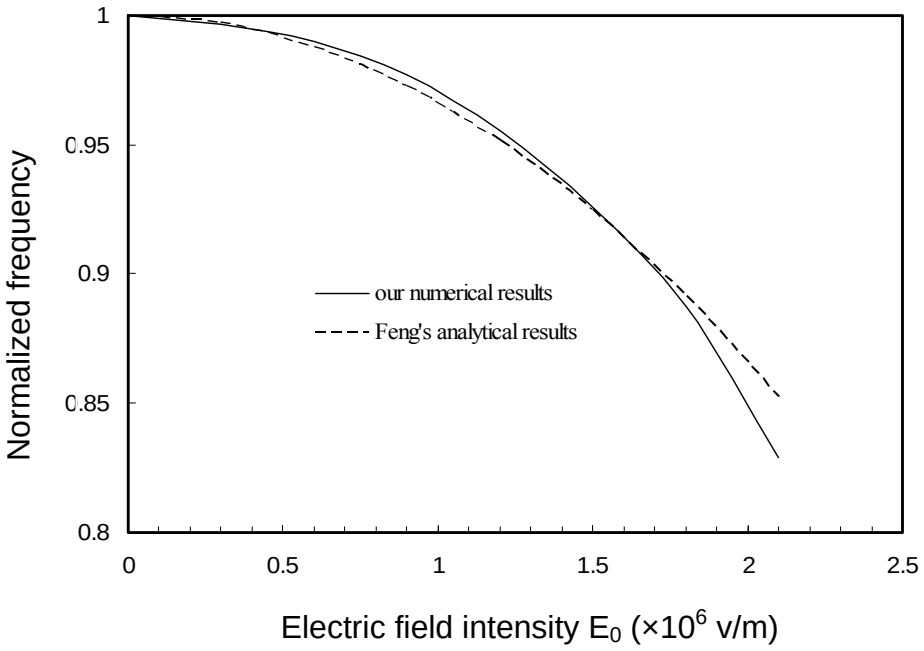

Figure 7.5 Normalized characteristic frequency of a conducting droplet changed with electrical field intensity E_0 with $a = 2.5\times10^{-3}$ m and $\gamma = 0.914$ (N/m). The initial deformation of the droplet is like that in Fig. 7.3

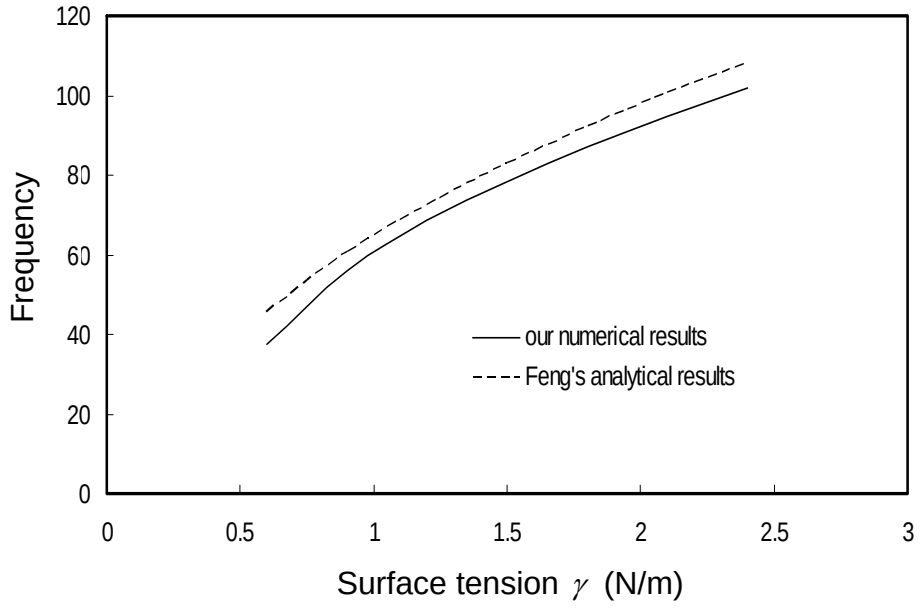

Figure 7.6 Characteristic frequency of a conducting drop changed with surface tension

In the other researchers' studies, the effect of the viscosity on the oscillation of the droplet is neglected, such as Feng and Beard used the Bernoulli's equation to describe the pressure field *p*. In present study, the Navier-Stokes equation is solved every time step and the effect of the viscosity is carried out. Fig. 7.7 shows the viscous decay of the oscillation amplitude of droplet. Fig. 7.7 (a) and (b) respectively depict the viscous decay of the oscillation amplitude without electric field and with electric field $E_0=1.0\times10^6$ (V/m). Fig. 7.7 (c) compares the result of (a) with that of (b), which shows that the frequency with the electric field is smaller than that without the electric field. As shown in Fig. 7.7, the frequency of the oscillation will keep unchanged with the decreasing of the amplitude of the oscillation caused by the viscous effect. The numerical experiments also describe that, unlike the electric fiend intensity and surface tension, the viscosity has no effect on the frequency of the oscillation of the electrostatically levitated droplet. In the present model, the damping constant τ is computed using the following equations,

$$a_l(t) = a + (a_l - a)\cos(2\pi ft)\exp(\frac{-t}{\tau}) \tag{7.33}$$

where $a_l(t)$ is the semi-major axis with time evolving, a is the radius of the spherical droplet, and a_l is the semi-major axis at initial time. The damping constant τ is not constant by using the current numerical model, which decreases with the time increasing. This result indicates that the high order mode plays a significant role in the damping of the oscillation.

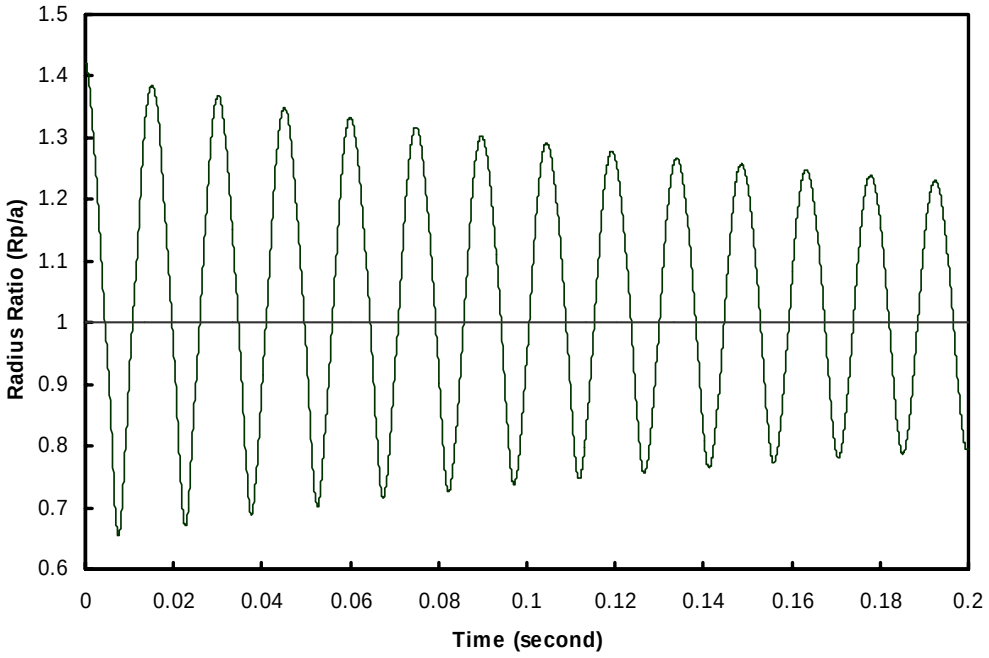
Radius Ratio (Rp/a)
1.5
1.4
1.3
1.2
1.1
1
0.9
0.8
0.7
0.6
0
0.02
0.04
0.06
0.08
0.1
0.12
0.14
0.16
0.18
0.2
Time (second)

(a)

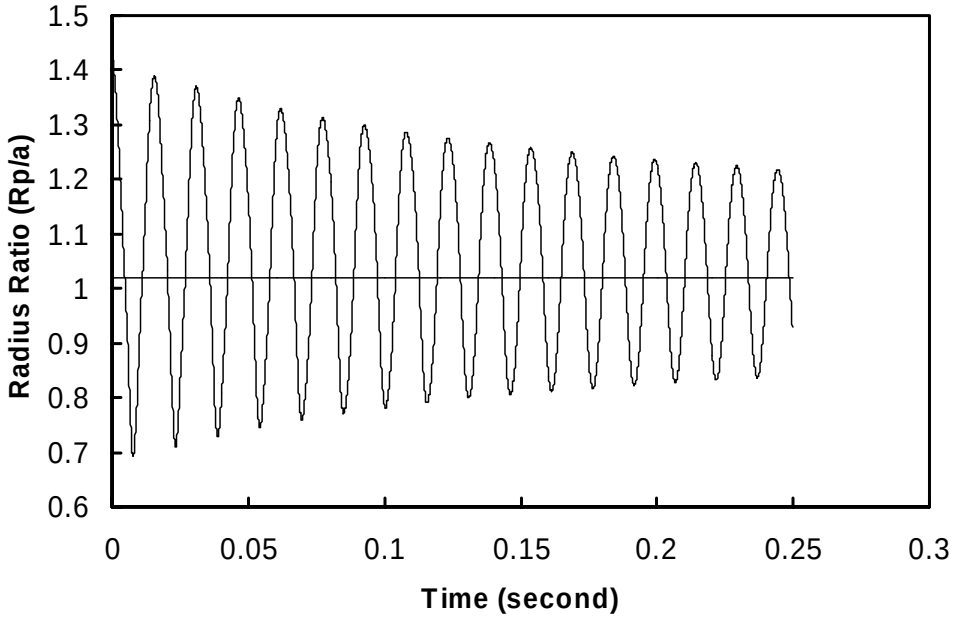
Radius Ratio (Rp/a)
1.5
1.4
1.3
1.2
1.1
1
0.9
0.8
0.7
0.6
0
0.05
0.1
0.15
0.2
0.25
0.3
Time (second)

(b)

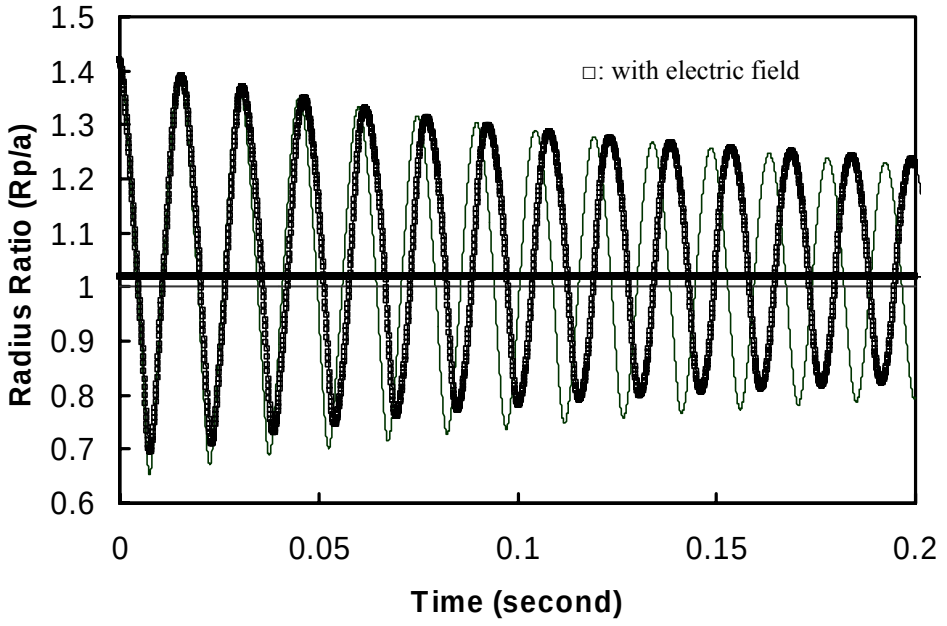

(c)

Figure 7.7 Viscous decay of oscillation amplitude ratio (divided by radius *a*) of the polar point of the droplet, where *a* = 2.5 mm and the center presents the steady state position, (a) oscillation without electric field, (b) oscillation with $E_0 = 1.0\times10^6$ (V/m), (c) Comparison with (a) and (b).

7.6 Concluding Remarks

In this chapter, a numerical study of melt droplet oscillation in electrostatic levitation mechanism has been described. Numerical analysis is based on the solution of the electric field by the boundary element method and the solution of the Navier-Stokes equations by the finite element, together with the use of deforming elements to track the oscillating free surface shapes. The computed result suggests that the frequency of the oscillation of the electrostatically levitated droplet decrease with the electric field increasing and increase with the surface tension increasing, which agrees with the prediction of the

analytic solution. The amplitude of the oscillation has no effect on the characteristic frequency. The damping constant is affected significantly by the high order mode.

CHAPTER 8

STABILITY OF THE DROPLET IN THE MAGNETIC LEVITATION MECHANISM

8.1 Introduction

This chapter presents a numerical study of the 3-D movement of the conducting spherical droplet in the magnetic levitation mechanism. The present chapter not only investigates the complex vertical and horizontal movement of the droplet, but also the self rotation of the droplet. The hybrid 3-D boundary element method (BEM) and finite element method (FEM) with edges elements are used to calculate electromagnetic fields, Lorentz force, and torques with respect to the axis. By this method, finite elements are used to discretize the spherical droplet region, while boundary elements are applied in the free space outside the droplet region with the surface of the droplet. The finite element and boundary element regions are then coupled through the interface boundary conditions. The iterative coupling of the BEM and FEM is applied to calculate the electromagnetic fields. The developed codes agree excellently with the available analytical and numerical solutions. Further, the complex 3-D movement of the magnetically levitated droplet is solved and analyzed by using the current FEM/BEM model.

8.2 Problem statement

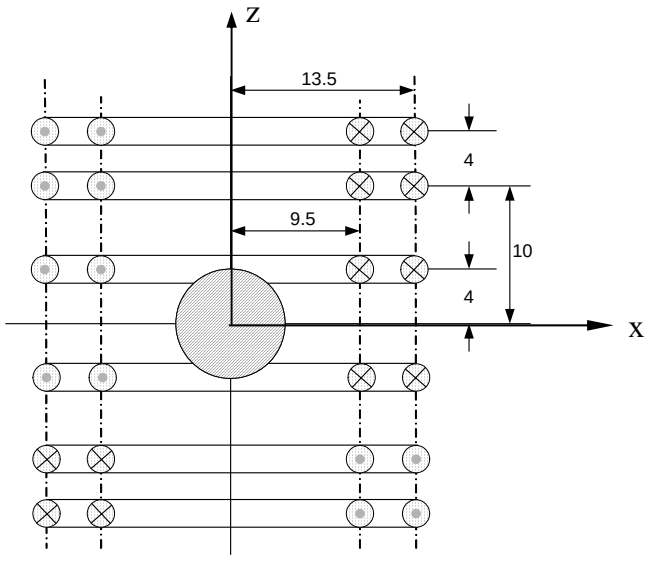

Figure 8.1 Schematic representation of magnetic levitation System

Figure 8.1 shows the TEMPUS device in use [Song, 1998a, 1998b, 1999a]. The system consists of two types of coils: (1) the inner four current loops (or heating coils) for sample heating and melting, and (2) the outer eight loops (or positioning coils) for sample positioning in space. During the operation, AC currents flow through these coils to generate an appropriate magnetic field. In magnetic levitation, eddy currents are induced in the sample and the dot product of eddy currents generates the Joule heating for the melting of the sample. These eddy currents also interact with the applied and induced magnetic fields to produce the Lorentz force in the sample. At present, we investigate the effect of the Lorentz force on the sample's 3-D movement in the magnetic levitation mechanism.

8.2.1 Governing equations and boundary conditions for the computation of the electromagnetic field

In order to calculate the distribution of electromagnetic fields in the specimen surrounded by the exciting coils, the Maxwell's equations have to be solved. However, Maxwell's equations are coupled partial differential equations, which have more than one unknown variables. Therefore, the vector wave equation derived from the Maxwell's equations combined with the energy equation is taken as the governing equations to simulate the microwave heating problems. With the analysis above, the equations for the electric and thermal fields may be written as follows

$$\nabla \times \frac{1}{\mu_r} \nabla \times \mathbf{E} - \omega^2 \mu \varepsilon_c \mathbf{E} = -j\omega\mu \mathbf{J}_i \tag{8.1}$$

In the above, $\mathbf{J}_i$ is an impressed or source current, and ε_c (=ε-jσ/ω) results from the combination of the induced current ($\sigma\mathbf{E}$) and displacement current (j$\omega\mathbf{D}$). The appropriate boundary conditions are stated below.

$$-\frac{1}{\mu_{r1}} \hat{\mathbf{n}}_1 \times \nabla \times \mathbf{E}_1 = -\mathbf{U}_1 = \mathbf{U}_2 = \hat{\mathbf{n}}_2 \times \nabla \times \mathbf{E}_2 \qquad \in \Omega_1 \cap \Omega_2 \tag{8.2}$$

where Ω_1 and Ω_2 are the FEM domain, BEM domain respectively. $\hat{\mathbf{n}}_1$ is outnormal from the FE region, and $\hat{\mathbf{n}}_2$ is outnormal from the BE region.

8.2.2 Governing equations and boundary conditions for the computation of the 3-D movement of the droplet in the magnetic levitation mechanism

After the computation of the electromagnetic fields, the time-averaged electromagnetic force induced in the sphere which is responsible for levitation as well as for fluid motion, is the cross product of induced current and the complex conjugate of the magnetic field,

$$\mathrm{F}_i = \frac{1}{2}\mathrm{Re}(\mathrm{J}\times\mathrm{B}^*) \tag{8.3}$$

$$\mathrm{F}_{ti} = \frac{1}{2}\mathrm{Re}(\mathrm{J}\times\mathrm{B}^*)\cdot dV_i \tag{8.4}$$

$$\mathrm{F}_{\mathrm{total}} = \int_V \mathrm{F}_{\mathrm{i}}\cdot dV_i \tag{8.5}$$

where *i* is the element number. As the levitating motion, we considered the translation. Therefore, the translation equations are introduced into this analysis. The Leap Frog Algorithm is used. This algorithm evaluates the velocities at half-integer time steps and uses these velocities to compute new positions.

$$\mathrm{v}^{\mathrm{n}+\frac{1}{2}} \equiv \frac{s^{n+1}-s^n}{\Delta t} \tag{8.6}$$

$$\mathrm{v}^{\mathrm{n}-\frac{1}{2}} \equiv \frac{s^n-s^{n-1}}{\Delta t} \tag{8.7}$$

So we can derive the new position, based on the old position and velocity:

$$\mathrm{s}^{\mathrm{n}+1} = \mathrm{s}^{\mathrm{n}} + \Delta \mathrm{t}\mathrm{v}^{n+\frac{1}{2}} \tag{8.8}$$

From the Verlet algorithm, we have the following expression for velocity:

$$\mathrm{v}^{\mathrm{n}+\frac{1}{2}} = \mathrm{v}^{\mathrm{n}+\frac{1}{2}} + \Delta t \mathrm{a}^{\mathrm{n}} \tag{8.9}$$

$$\mathrm{a}^{\mathrm{n}} = \mathrm{F}_{\mathrm{total}}^{n} / \mathrm{m} \tag{8.10}$$

where **a** is the acceleration, **m** is the weight of the metal, Δ**t** the width of time step, **v** the velocity at center of the metal and **s** the position vector. The fluid flow and temperature distribution may also be calculated at every time step.

After the time-averaged electromagnetic force is calculated, the torque with respect to the axis may be written as follows,

$$N_{ti} = \mathrm{R}_i \times \mathrm{F}_{ti} \tag{8.11}$$

$$\mathrm{N}_{\mathrm{total}} = \sum_{i=1} N_{ti} \tag{8.12}$$

The rotating moving equations at every time step are given by,

$$\omega^{n+1} = \omega^{\mathrm{n}} + \Delta\omega^{n} \tag{8.13}$$

$$\theta^{n+1} = \theta^{\mathrm{n}} + \Delta\theta^{n} \tag{8.14}$$

with

$$\Delta\omega^n = \mathrm{N}_{\text{total}} \Delta t / I_m \tag{8.15}$$

$$\Delta\theta^n = \omega^n \Delta t + \mathrm{N}_{\text{total}} \Delta t^2 / (2I_m) \tag{8.16}$$

where R_i is the radius vector drawn from center to surface of a sphere metal, ω the angular velocity, θ the rotational angle, and I_m the moment of inertia. In the present study, the droplet is assumed to be spherical without considering the deformation of the droplet. Therefore, the moment of inertia I_m may be written as,

$$I_m = (2/5)\mathrm{mR}^2$$

where m is the weight of the droplet, R the radius of the spherical droplet.

8.3 Method of Solution

The 3-D electromagnetic field may be solved using the edge finite element method [Huo, 2004c, 2005b]. The edge-based elements are necessary to satisfy the divergence-free constraint, $\nabla \cdot \mathbf{E}=0$ [Johns, 1971]. However, the huge sparse matrix produced by the FEM appears to be a major setback to finding an efficient numerical solution to a large scale problem. Our experience shows that this remains true even with various efficient solvers designed specifically for the solution of a large sparse system of linear algebraic equations to improve the computational efficiency. To alleviate the disadvantage of the finite element method, a hybrid finite element-boundary method is employed instead.

Using this approach, finite elements are used in the conducting droplet where power density is needed and material properties may be a function of temperature, while boundary elements are used elsewhere. The FEM and the BEM are coupled through the interface boundary conditions. This idea is shown in Figure 8.2

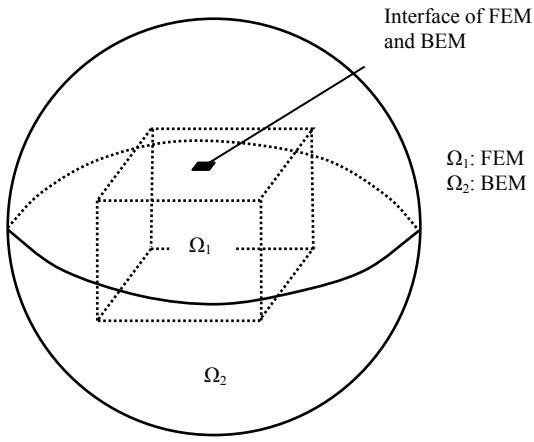

Figure 8.2 Schematic representation of the coupling of the finite element and boundary element

8.3.1 Finite element formulation

To develop a finite element formulation in the conducting droplet, the wave equation (8.1) is integrated with respect to a vector testing function δ**E** [Akarapu, accepted].

$$\iiint_V \delta \mathrm{E} \cdot \left(\nabla \times \frac{1}{\mu_r} \nabla \times \mathbf{E} - \omega^2 \mu \varepsilon_c \mathbf{E} \right) dV = -\iiint_V j\omega\mu \mathbf{J}_i \cdot \delta \mathrm{E} dV \qquad (8.17)$$

Integration by parts gives rise to the surface integral term,

$$\iiint_V \frac{1}{\mu_r}\nabla\times\mathbf{E}\cdot\nabla\times\delta\mathrm{E}\,dV-\iiint_V \omega^2\mu\varepsilon_c\delta\mathrm{E}\cdot\mathbf{E}\,dV= \oiint_S \frac{1}{\mu_r}\left(\delta\mathrm{E}\times\nabla\times\mathbf{E}\right)\cdot\mathbf{n}\,dS-\iiint_V j\omega\mu\delta\mathrm{E}\cdot\mathbf{J}_i\,dV \tag{8.18}$$

Making use of the vector identity

$$\left(\delta\mathrm{E}\times\nabla\times\mathbf{E}\right)\cdot\hat{\mathbf{n}}=-\left(\hat{\mathbf{n}}\times\nabla\times\mathbf{E}\right)\cdot\delta\mathrm{E} \tag{8.19}$$

and also the boundary conditions, the final integral formulation is obtained,

$$\iiint_V\left(\frac{1}{\mu_r}\nabla\times\mathbf{E}\cdot\nabla\times\delta\mathrm{E}-\omega^2\mu\varepsilon_c\delta\mathrm{E}\cdot\mathbf{E}\right)dV= -\oiint_S\left[\delta\mathrm{E}\cdot\mathbf{U}\right]dS-\iiint_V j\omega\mu\delta\mathrm{E}\cdot\mathbf{J}_i\,dV \tag{8.20}$$

With appropriate finite element discretization and necessary elemental calculations followed by assembly, one has the matrix representation of equation (3.46),

$$[\mathrm{K}]\{\mathrm{E}\}+[\mathrm{B}]\{\mathrm{U}\}=\{\mathrm{F}\} \tag{8.21}$$

where the matrix elements are calculated using the following expressions,

$$K_{ij} = \iiint_V \left(\frac{1}{\mu_r} \nabla \times \mathbf{N}_i \cdot \nabla \times \mathbf{N}_j - \omega^2 \mu \varepsilon_c \mathbf{N}_i \cdot \mathbf{N}_j \right) dV$$

$$B_{ij} = \oiint_S \mathbf{N}_i \cdot \mathbf{S}_j \, dS$$

$$F_i = -\iiint_V j \varpi \mu \mathrm{N_i} \cdot \mathrm{J_i} dV$$

Note that here $\mathbf{N}_i$ and $\mathbf{S}_i$ are edge-based vector shape functions and their derivatives.

8.3.2 Boundary element formulation using the dyadic Green function

The basic idea of the hybrid FE/BE method was first introduced for the study of electromagnetics by Silvester and Hsieh (1971) and McDonald and Wexler (1972) for solving exterior or unbounded field problems. Later, the method was applied to solve two- and three-dimensional antenna and scattering problems. Here, it is applied to solve the electromagnetic field in a microwave system, and the formulation is based on Green's theorem involving the dyadic Green function,

$$\begin{aligned} \iiint_V & \left(\mathbf{E} \cdot \nabla \times \nabla \times \overline{\overline{G}} - \overline{\overline{G}} \cdot \nabla \times \nabla \times \mathbf{E} \right) dV \\ &= \oiint_S \left(\overline{\overline{G}} \times \nabla \times \mathbf{E} - \mathbf{E} \times \nabla \times \overline{\overline{G}} \right) \cdot \hat{\mathbf{n}} \, dS \\ &= \oiint_S \left((\hat{\mathbf{n}} \times \mathbf{E}) \cdot \nabla \times \overline{\overline{G}} + (\hat{\mathbf{n}} \times \nabla \times \mathbf{E}) \cdot \overline{\overline{G}} \right) dS \end{aligned} \tag{8.22}$$

Now, substituting into the above equation the following wave equations and the equations for the dyadic Green function,

$$\nabla \times \nabla \times \mathbf{E} - k_0^2 \mathbf{E} = -j\omega\mu \mathbf{J}_i \tag{8.23}$$

$$\nabla \times \nabla \times \overline{\overline{G}} - k_0^2 \overline{\overline{G}} = \bar{\bar{I}} \delta(\mathbf{r} - \mathbf{r}') \tag{8.24}$$

and carrying out the necessary integration, we can get,

$$\begin{aligned} \mathbf{E}(\mathbf{r}) = & -jk_0 Z_0 \iiint_V \mathrm{J}(\mathrm{r}') \cdot \overline{\overline{G}}_0(\mathrm{r}, \mathrm{r}') dV' - \\ & \oiint_S \{[\hat{\mathrm{n}}' \times \mathrm{E}(\mathrm{r}')] \cdot [\nabla' \times \overline{\overline{G}}_0(\mathrm{r}, \mathrm{r}')] + \\ & [\hat{\mathrm{n}}' \times \nabla' \times \mathrm{E}(\mathrm{r}')] \cdot \overline{\overline{G}}_0(\mathrm{r}, \mathrm{r}')\} dS' \end{aligned} \tag{8.25}$$

The surface's unit normal direction points outward from the region Ω_2. In equation (8.25) the first term on the right-hand side is the field radiated by **J** in the free-space environment, thus denoted as $\mathbf{E}_{inc}$. With the following relation,

$$\nabla' \times \overline{\overline{G}} = \nabla' G_0(\mathrm{r}, \mathrm{r}') \times \bar{\bar{I}} \tag{8.26}$$

and the surface divergence theorem, equation(8.25) can be further simplified as

$$\begin{aligned} \mathbf{E}(\mathbf{r}) = & \mathbf{E}_{inc}(\mathrm{r}) - \\ & \oiint_S \left(\hat{\mathbf{n}}' \times \mathbf{E}(\mathrm{r}') \times \nabla' G(\mathrm{r}, \mathrm{r}') + \left(\hat{\mathrm{n}}' \times \nabla' \times \mathrm{E}(\mathrm{r}')\right) G(\mathrm{r}, \mathrm{r}')\right) dS(\mathrm{r}') \\ & - \frac{1}{k_0^2} \oiint_S \nabla G(\mathrm{r}, \mathrm{r}') \nabla' \cdot \left(\hat{\mathbf{n}}' \times \nabla \times \mathbf{E}(\mathrm{r}')\right) dS(\mathrm{r}') \end{aligned} \tag{8.27}$$

Taking the cross product of equation (8.27) with surface normal $\hat{\mathbf{n}}$ yields

$$\hat{\mathbf{n}}\times\mathbf{E}(\mathrm{r})=\hat{\mathbf{n}}\times\mathbf{E}_{inc}(\mathrm{r})-$$
$$\hat{\mathbf{n}}\times\iint_S\left(\hat{\mathbf{n}}'\times\mathbf{E}(\mathrm{r}')\times\nabla' G(\mathbf{r},\mathbf{r}')+\left(\hat{\mathbf{n}}'\times\nabla'\times\mathbf{E}(\mathrm{r}')\right)G(\mathbf{r},\mathbf{r}')\right)dS(\mathrm{r}') \tag{8.28}$$
$$-\frac{1}{k^2}\hat{\mathbf{n}}\times\iint_S\nabla G(\mathbf{r},\mathbf{r}')\nabla'\cdot\left(\hat{\mathbf{n}}'\times\nabla\times\mathbf{E}(\mathbf{r}')\right)dS(\mathbf{r}')$$

After the BE discretization using edge boundary elements, followed by calculations at the element level, equation (8.28) may be represented in the following matrix form,

$$[\mathrm{B}^{ss}]\{\mathrm{E}^s\}=\{\mathrm{b}^s\}-\sum_{\mathrm{t}}^{\mathrm{M_t}}[\mathrm{P}^{st}]\{\mathrm{E}^t\}-\sum_{\mathrm{t}}^{\mathrm{M_t}}[\mathrm{Q}^{st}]\{\mathrm{U}^t\} \tag{8.29}$$

where the matrix elements are calculated by

$$\left[\mathrm{B}^{ss}\right]=-\iint_{S^s}\left\{\mathbf{N}^s\right\}\cdot\left\{\mathbf{S}^s\right\}^T dS(\mathbf{r})$$

$$\left\{\mathrm{b}^s\right\}=\iint_{S^s}\left\{\mathbf{S}^s\right\}\cdot\mathbf{E}_{inc}(\mathrm{r})\,dS(\mathbf{r})$$

$$\left[\mathrm{P}^{st}\right]=\iint_{S^s}\left\{\left\{\mathbf{S}^s\right\}\cdot\iint_{S^t}\left\{\mathbf{S}^t\right\}^T\times\nabla' G(\mathbf{r},\mathbf{r}')dS(\mathbf{r}')\right\}dS(\mathbf{r})$$

$$\left[\mathrm{Q}^{st}\right]=\iint_{S^s}\left\{\left\{\mathbf{S}^s\right\}\cdot\iint_{S^t}\left\{\mathbf{S}^t\right\}^T G(\mathbf{r},\mathbf{r}')dS(\mathbf{r}')\right\}dS(\mathbf{r})$$
$$-k^{-2}\iint_{S^s}\left\{\left\{\nabla\cdot\mathbf{S}^s\right\}\iint_{S^t}\nabla'\cdot\left\{\mathbf{S}^t\right\}^T G(\mathbf{r},\mathbf{r}')dS(\mathbf{r}')\right\}dS(\mathbf{r})$$

With some matrix algebra, equation (8.29) is written more conveniently in the following form,

$$[\mathbf{B}_2]\{\mathbf{U}_2\} = \{\mathbf{F}_2\} + [\mathbf{K}_2]\{\mathbf{E}_2\} \tag{8.30}$$

where $\mathbf{B}_2$ is the boundary element matrix associated with the unknowns.

8.3.3 Coupling of boundary and finite elements

The boundary and finite element formulations for the solution of electric field distribution are coupled through the interface conditions along the boundary of Ω_1 and the boundary of Ω_2,

$$\frac{1}{\mu_{r1}}\hat{\mathbf{n}} \times \nabla \times \mathbf{E}_1 = \frac{1}{\mu_{r2}}\hat{\mathbf{n}} \times \nabla \times \mathbf{E}_2 \tag{8.31}$$

$$\hat{\mathbf{n}} \times \mathbf{E}_1 = \hat{\mathbf{n}} \times \mathbf{E}_2 \tag{8.32}$$

There are two ways to obtain a coupled solution of equations (8.21) and (8.30) with the use of the above interface conditions. One way is to use direct coupling, by which the entire boundary element region is treated as a macro element, and the boundary element global matrix is then incorporated into equation (8.21). This approach works efficiently for 2-D and moderately sized 3-D problems [Li, in print]. However, it becomes inefficient for large 3-D problems such as the one under consideration because it substantially increases the resultant edge finite element matrix bandwidth and hence the CPU times. Another approach is iterative [Huo, 2004c, 2005b]. By this approach,

equation (8.30) is solved for $\{\mathbf{U}_2\}$ with an assumed $\{\mathbf{E}_2\}$ on the interface. The standard LU-decomposition for complex matrix can be used for the solution. Then $\{\mathbf{E}_1\}$ is solved using equation (8.21) with known $\{\mathbf{U}_2\}$. The convergence on $|\{\mathbf{E}_2\}-\{\mathbf{E}_1\}|<\varepsilon$, where ε is the convergence criterion, is checked. If convergence is not achieved, $\{\mathbf{E}_2\}=\{\mathbf{E}_1\}$ along the interface is used to predict an updated $\{\mathbf{U}_2\}$ using equation (19) and then $\{\mathbf{E}_1\}$ is updated using equation (8.21). The process is repeated until the convergence is achieved.

It is worth noting here that for either of the two approaches, the matrix $\mathbf{B}_2$ requires an LU-decomposition only once and the decomposed matrices are stored in the memory for subsequent back substitutions when needed. In the case of the iterative procedure, this means that subsequent iteration between FE and BE requires only a back substitution procedure, thereby leading to a significant increase in computational speed.

8.4 Results and Discussion

The computational algorithm developed in section 8.3 is capable of predicting the electric field distribution, the magnetic field distribution, the energy distribution, the displacement distribution, and the temperature and fluid flow distribution. The criterion for the convergence of nonlinear iteration is set to 1×10^{-5}. The computer code for the simulation of the electromagnetic fields needs to be checked against the available analytic solution before applied for the droplet calculation. The testing is done in section 8.4.1 for two cases: 1) benchmark testing in a standard waveguide and 2) electromagnetic field distribution in the semi-infinite metallic slab. In the computation of the magnetically levitated droplet, there are also two cases compared with the available results: 1) 3-D

Joule heating distribution in a single current loop surrounding a conducting sphere and 2) Joule heating distribution of the steady state droplet in the poisoning coils

8.4.1 Validation of the computer model

First, the electric field distribution in the standard MW-975 waveguide is considered. The waveguide is filled with air, and the length of the waveguide in the propagation direction is $1.25\lambda_z$. The TE_{10} model from a device is launched at the entrance of the waveguide, and then the waves undergo reflection at the bottom surface. The reflected waves interfere with the incident waves to distribute the electrical field within the internal space. The analytic expression for the electric field is written as follows,

$$\mathbf{E}_y = \mathbf{E}_0^{+} e^{-jk_z Z} + \mathbf{E}_0^{-} e^{+jk_z Z} \tag{8.33}$$

Fig. 8.3 shows the 3-D view of the distribution of the electric field ($\mathbf{E}_y$-component) and the module of the electric field $|\mathbf{E}|$ distribution. Fig. 8.4 compares the numerically calculated electric field distribution along the central axis in the propagation direction with the analytic solution given by equation (8.33). The computed result from the FE/BE model is only plotted for the FE region because the surface integral is used in the BE region. Excellent agreement exists between the numerical and analytic solutions, thereby validating the present FE/BE formulation. Though not shown, the same results were obtained using the FEM only.

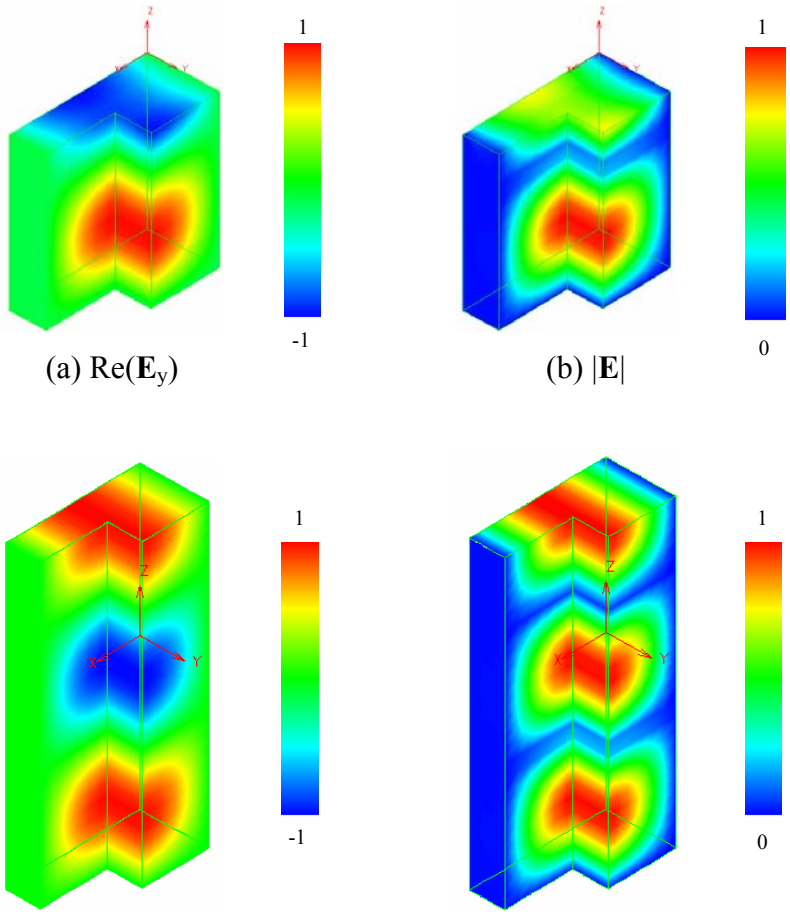

(a) Re($\mathbf{E}_y$) (b) |$\mathbf{E}$|

(c) Re($\mathbf{E}_y$) (d) |$\mathbf{E}$|

Figure 8.3 3-D view of the distribution of the dominant electric field ($\mathbf{E}_y$-component) and the module of the electric field ($\mathbf{E}$) in the standard WR-975 waveguide with $c_z=1.25\lambda_z$. The field value is normalized by the respective maximum values.

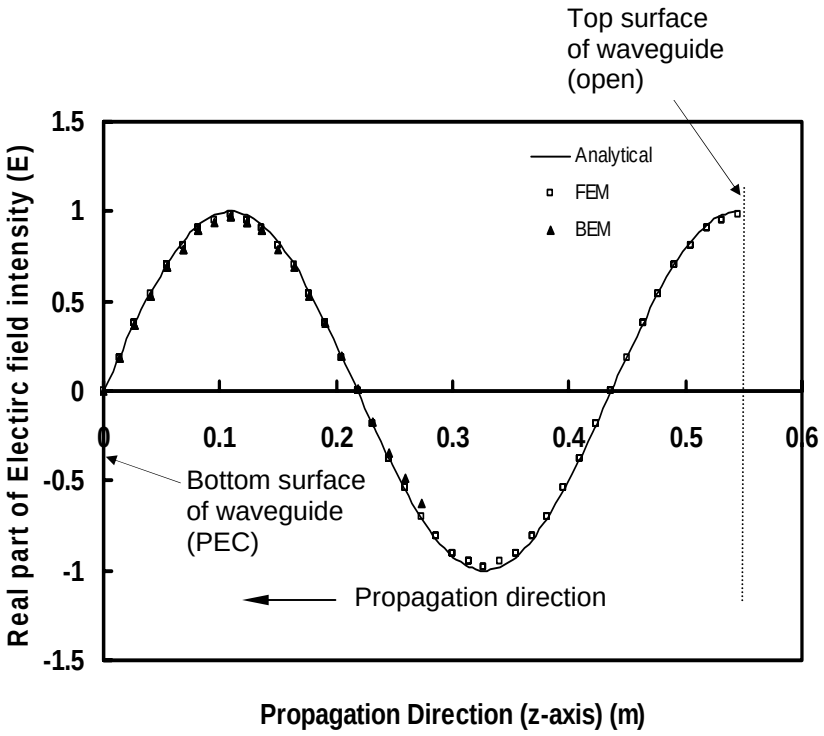

Figure 8.4 Dominant electric field ($\mathbf{E}_y$-component) distribution along the center line of the standard WR-975 waveguide in the propagation direction (negative z direction) obtained from the analytic, FEM and FE/BE solutions. The result by using FE/BE has only bottom half part which is the FEM part

As another comparison, a semi-infinite metallic slab shown as the insert in Fig. 8.5 is considered. The analytic equation for the electric and magnetic fields can be easily obtained,

$$\mathbf{E}_y = \mathbf{E}_s e^{-\gamma_m y}, \quad \mathbf{H}_y = \mathbf{H}_s e^{-\gamma_m y} \tag{8.34}$$

The coefficients are calculated by

$$\gamma_m = \alpha(1+j), \quad \text{and} \quad \delta = \frac{1}{\alpha} = \sqrt{\frac{2}{\sigma_m \omega \mu}}$$

where δ is the skin depth over which the electric and magnetic fields drop to 1/e of their value at the surface. Fig. 8.5 depicts that the numerical results from the FE/BE or FEM agree with the analytic results very well, thereby validating once again the FE/BE and/or FE implementations.

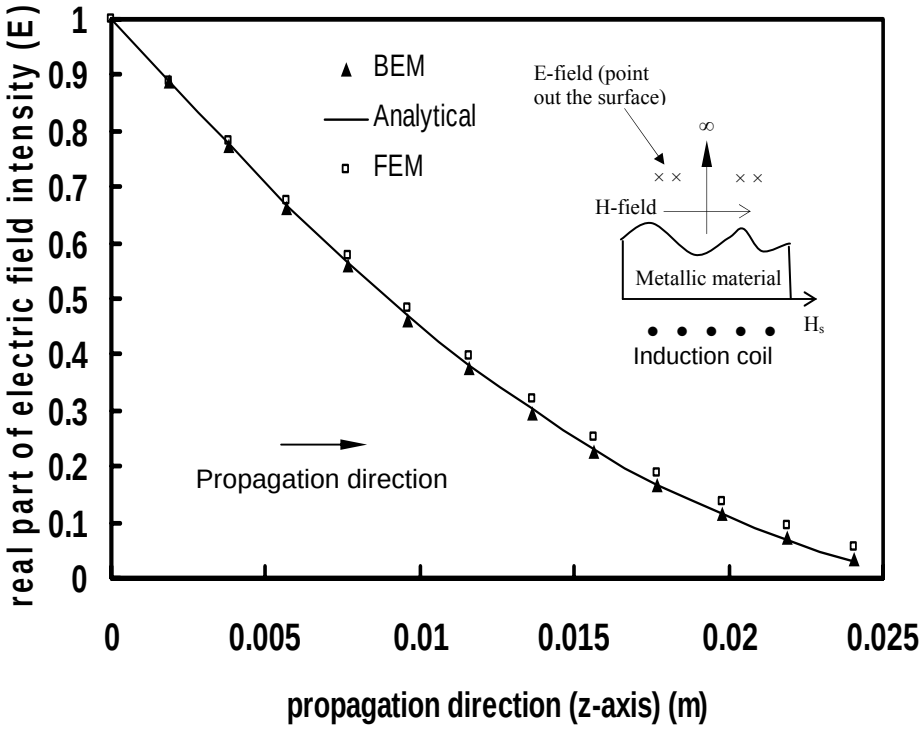

Figure 8.5 Electric field distribution ($\mathbf{E}_y$-component) for the semi-infinite metallic slab and part of induction heating coil.

8.4.2 Validation of the computer model in the magnetically levitated droplets

In the computation of the droplet, the unstructured meshes are shown in Fig. 8.6. First, the boundary and finite element program is tested against available solutions of the electromagnetic field and Joule heating for a simple geometry. We consider a single current loop surrounding a conducting sphere, as shown in Fig. 8.8a. The loop is located at the equator plane. Fig. 8.7 shows the Joule heating and temperature distribution within the sphere, which is compared with Song and Li's results (1998a), as shown in Fig. 8.6b. Clearly, near the current loop the Joule heating attains a maximum value and decays rapidly both in the θ- and r- directions away from the current loop, which is consistent with the predictions from the electromagnetic theory.

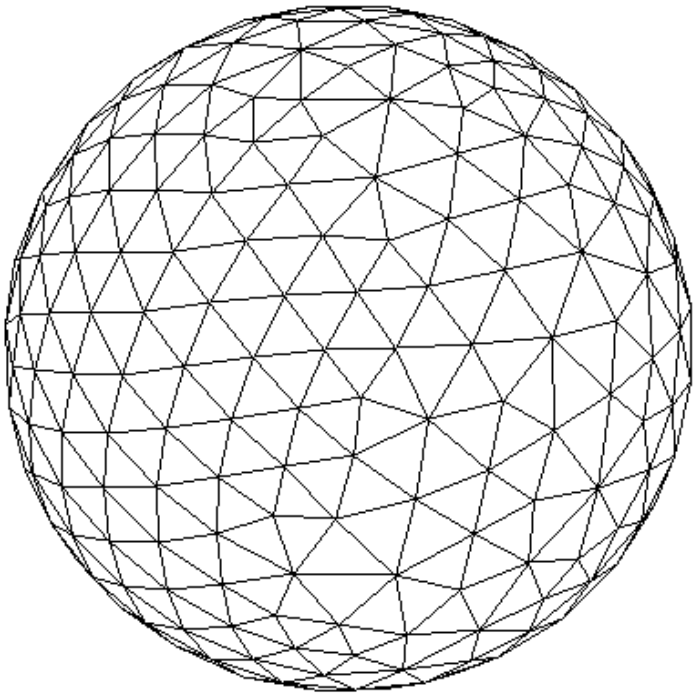

Figure 8.6 Finite element and boundary element meshes for the computation of the magnetically levitated droplet

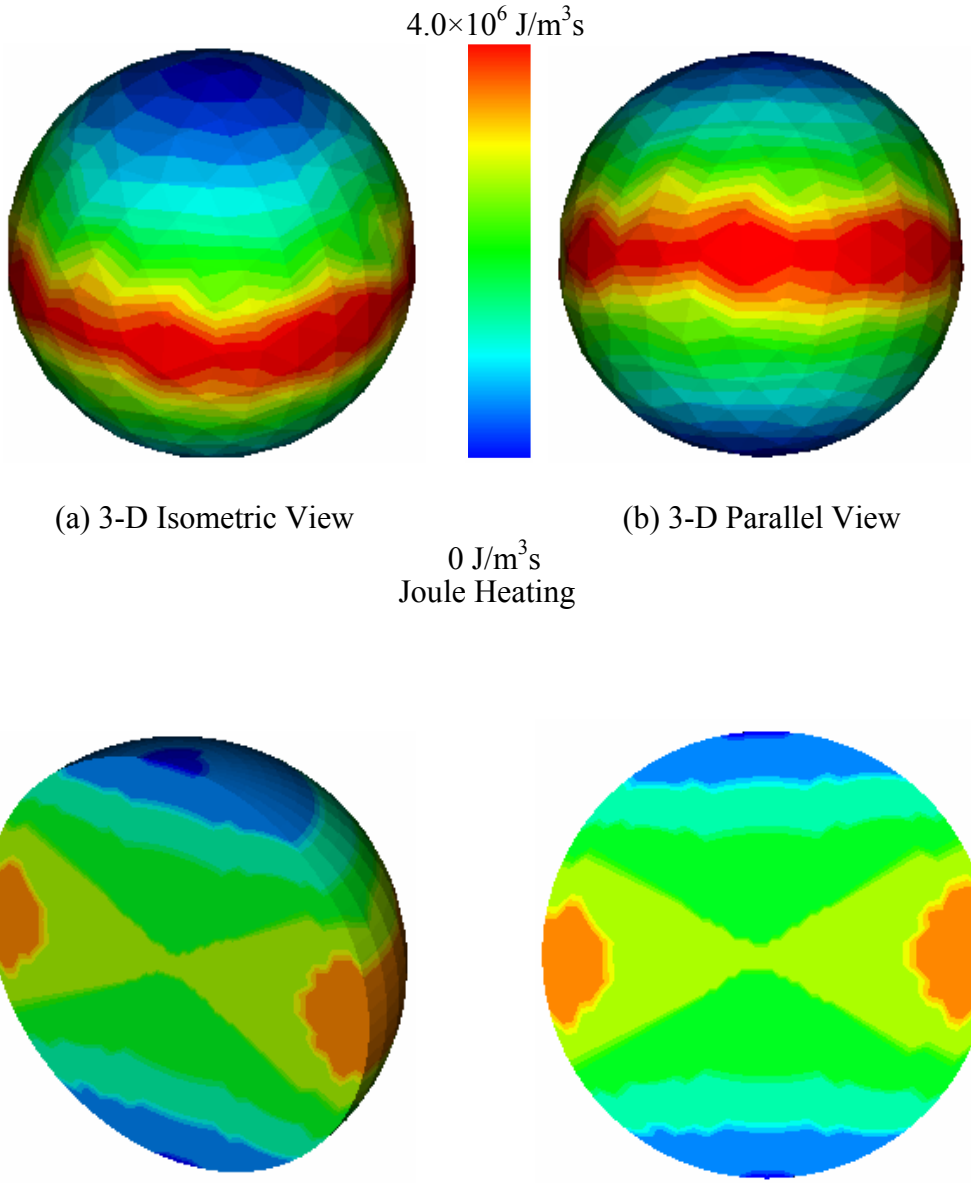

Figure 8.7 Joule heating and temperature distribution for the droplet surrounded by the single current coil, the conditions are used: coil current I (peak) =212 Amp, frequency = 1.45×10^5 Hz, radius of sphere a=6mm, radius of coil loop=9mm, electrical conductivity=3.85×10^6 1/(Ohm-m).

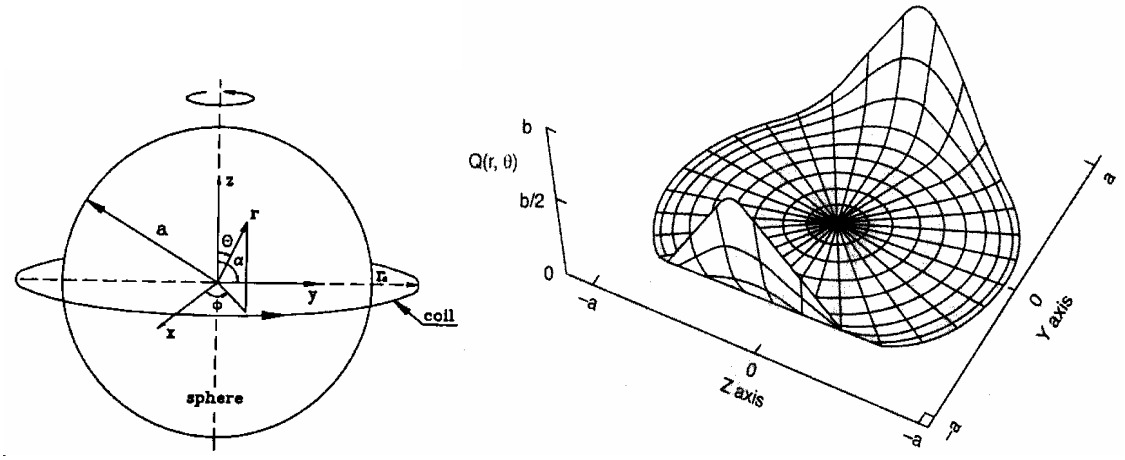

(a) (b)

Figure 8.8 Scanned figure from Song and Li (1998a). (a) Schematic representation of the conducting droplet surrounded by a single current coil, (b) Joule heating distribution for the conducting droplet in (a), where $b=4.0\times10^6$ J/m^{3}s

Second, let us see the distribution of the Joule heating and temperature inside the droplet when the positioning coils (see Fig. 8.1) are only turned on. In contrast with the strong droplet deformation and heating effect of the heating coils, the positioning coils are designed mainly to keep the droplet from drifting in space. It is of interest to know what effect the positioning coils would have on a liquid droplet. Song and Li (1999b) had investigated the temperature distribution under the action of positioning coils only. Figure 8.9 shows the Joule heating of the silver sample (see Table 8.1) under the action of positioning coils only. It demonstrates the quadrupole effect produced by the positioning coils. The maximum Joule heating occurs at two locations symmetric about the equator plane and the minimum Joule heating at the equator plane. The temperature based on this Joule heating distribution agrees with the result of Song and Li (1999b) very well. This

Joule heating distribution should not come as a surprise given the positioning coils are 180^0 out of phase and thus produce a canceling effect at the equatorial plane and a lower Joule heating. As shown in Fig. 8.10, the temperature distribution of the magnetically levitated droplet for different positions is also investigated. Fig. 8.11 shows the temperature distribution of magnetically levitated droplet at different initial position along the horizontal X axis.

Parameters	Value	Units
Density of liquid silver	9346	Kg/m^3
Electric conductivity of liquid silver	6.0×10^6	$(\Omega\text{-m})^{-1}$
Frequency (positioning)	1.44×10^5	Hz
Applied current (peak, positioning)	140	A
Radius of sphere	5.0	mm

Table 8.1 Parameters for computation of the droplet in the magnetically levitation mechanism under the microgravity environment

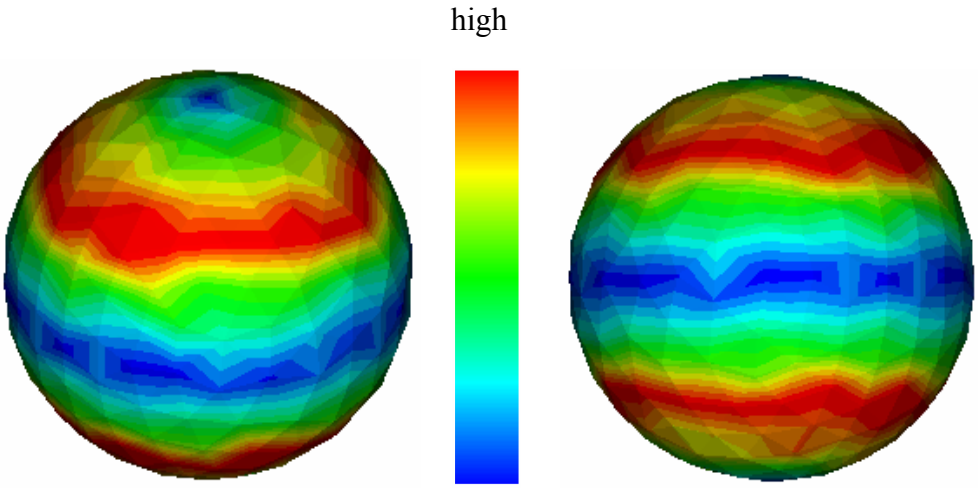

(a) 3-D Isometric View (b) 3-D Parallel View

Joule Heating

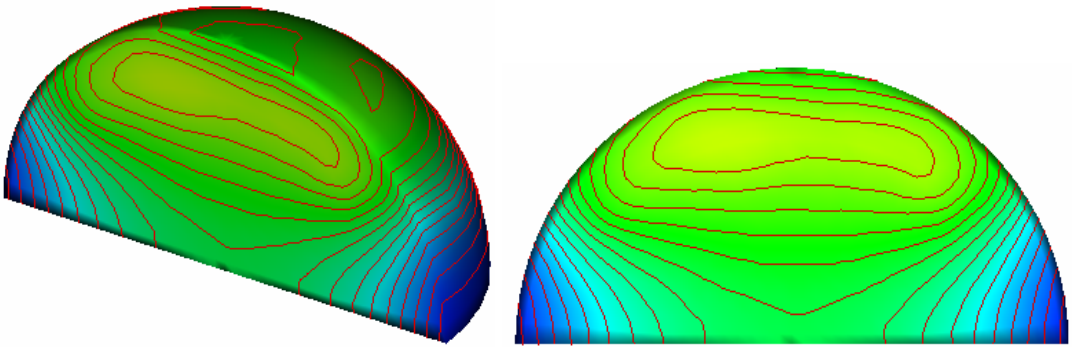

(c) 3-D Isometric View (d) 3-D Parallel View

Temperature

Figure 8.9 Joule heating and temperature distribution in a silver droplet induced by positioning coils only with 180^0 out of phase in the TEMPUS system and microgravity conditions.

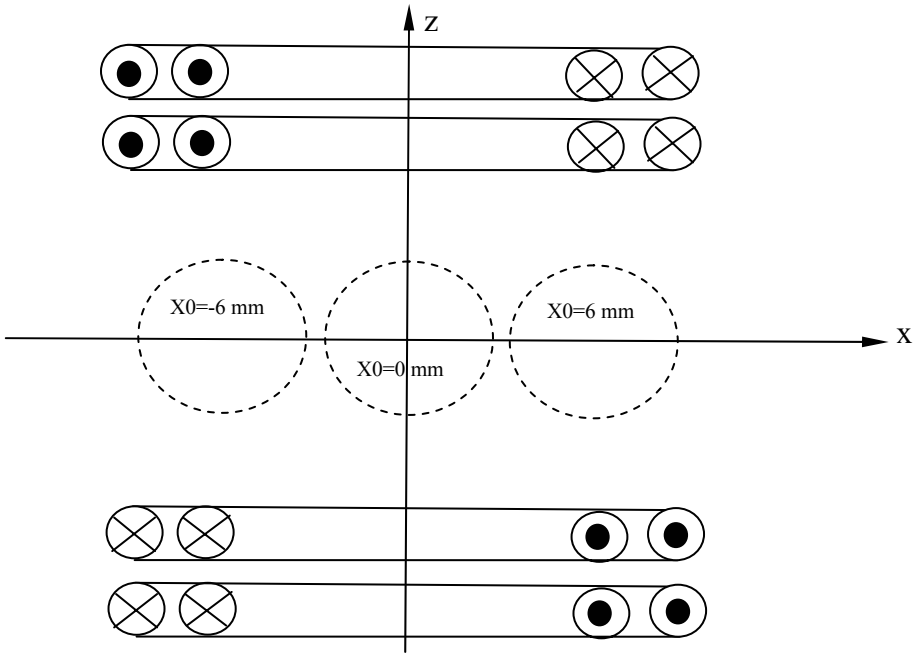

Figure 8.10 Schematic representative of the magnetically levitated droplet with different initial position along the horizontal X axis.

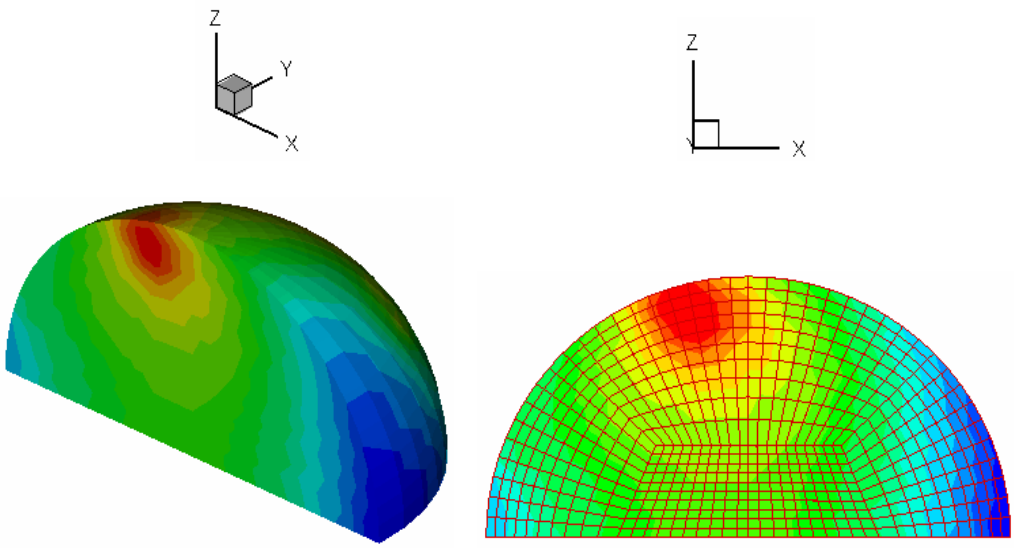

(a) X0 = -6 mm

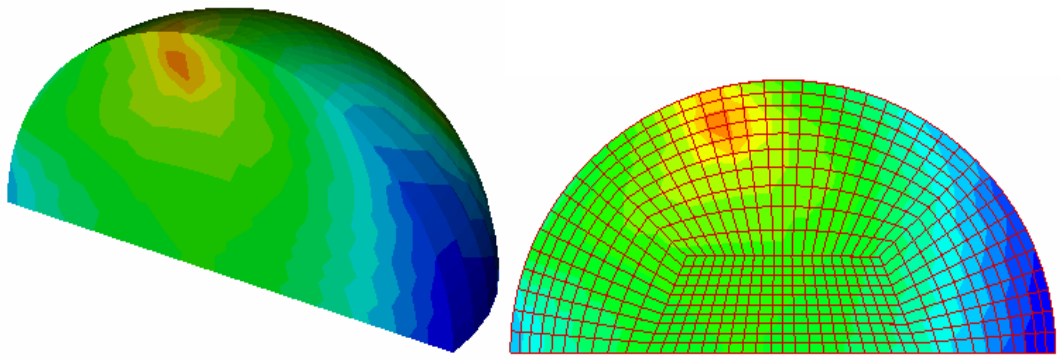

(b) X0 = -4 mm

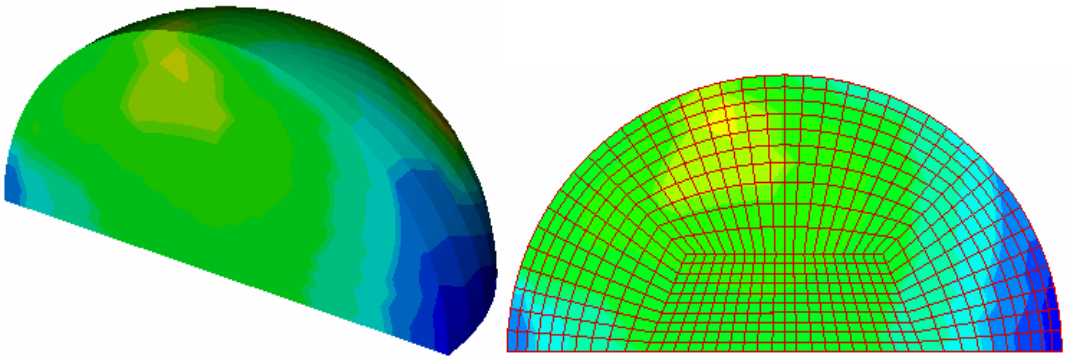

(c) X0 = -2 mm

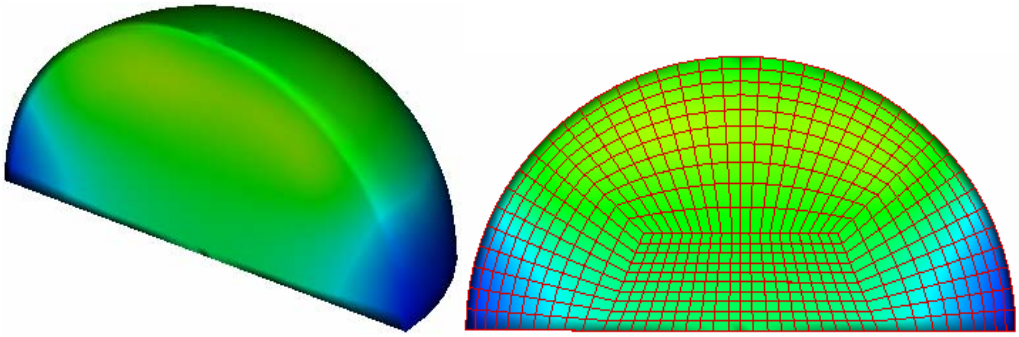

(d) Steady-state position

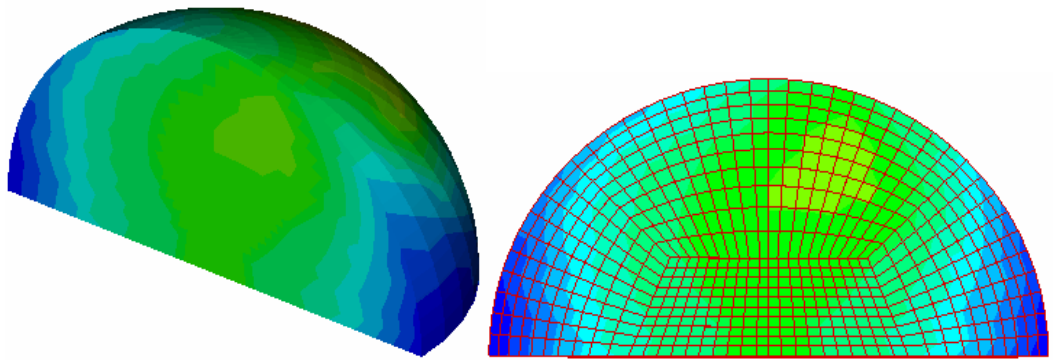

(e) X0 = 2 mm

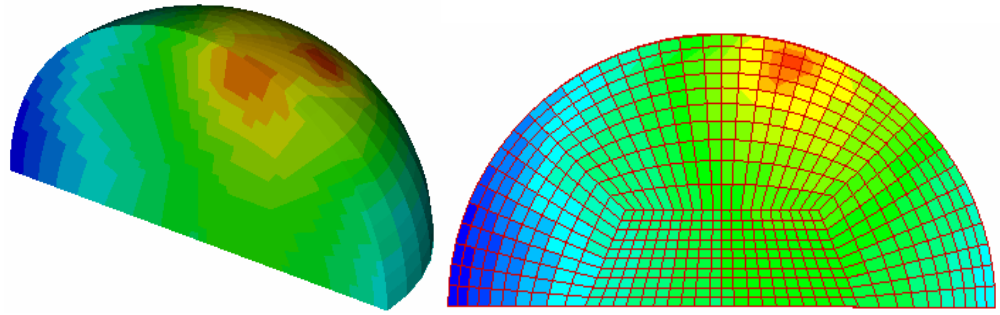

(f) X0 = 4 mm

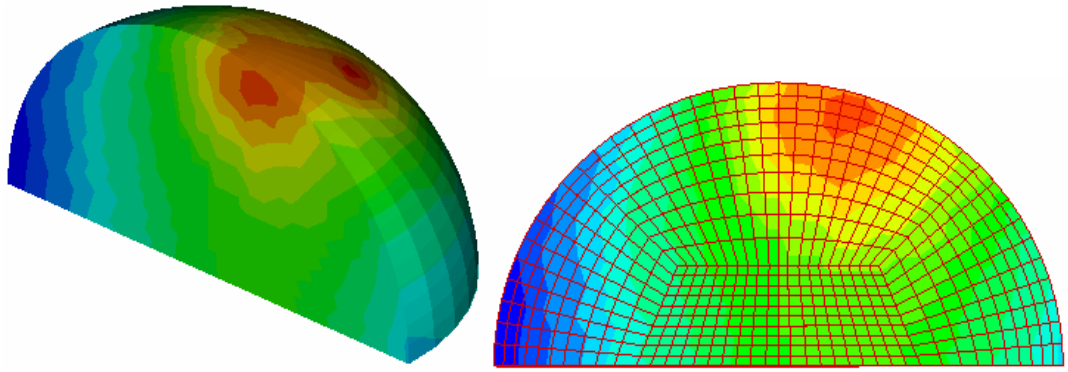

(g) X0 = 6 mm

Figure 8.11 Temperature distribution in a silver droplet induced by positioning coils only with 180^0 out of phase in the TEMPUS system and microgravity conditions with different initial position along the horizontal X axis.

8.4.3 3-D translation of the magnetically levitated droplet

The purpose of this chapter is to study how the magnetically levitated droplet moves. In this section, we focus on the 3-D translation of the magnetically levitated droplet. The levitating conducting droplet is assumed to be liquid silver sphere, whose properties are shown in Table 8.1. In the study of the movement of the magnetically levitated droplet, the steady-state position of the levitating droplet is assumed to stay at the original point (0, 0, 0) in the rectangular coordinate. The centers of the coils are fixed above or below the steady-state position along the z axis. There are no movement and rotation if the initial position of the magnetically levitated droplet is at the steady-state position. However, it is difficult to pose the initial position of the magnetically levitated droplet to the steady-state position. Therefore, it is necessary to investigate the 3-D movement of the magnetically levitated droplet. Fig. 8.12 (a) presents the 3-D movement of the magnetically levitated droplet when the initial position vertically deviates from the steady-state position. Various magnitudes of initial positions (Z0=2 mm, 3 mm) away from the equilibrium position in the Z-axis are investigated. The computed results (as seen in Fig. 8.12 (a)) show that the frequency changes a little and it may be assumed to be kept the same no matter how large deviation from the equilibrium position at the starting time. Also in Fig. 8.12(a), it is shown that the amplitude of the oscillation along the z-axis does not change with the time evolving. Like the initial positions away from the equilibrium position in the vertical direction, the computed results with the initial positions (X0=2 mm, 3mm) away from the equilibrium position in the horizontal direction present that the frequencies have small difference for different amplitude of the oscillation with the evolvement of the time, as shown in Fig. 8.12 (b). Comparing Fig.

8.12 (a) with Fig. 8.12 (b) illustrates that the frequency in the vertical movement is clearly faster than that in the horizontal movement. The computed results show, when the initial position of the droplet is above 14 mm or below -14 mm along z axis, the oscillation of the droplet does not occur and the droplet will move away from the levitated mechanism.

The complex initial deviation from the steady-state position is also investigated. When the initial position deviate horizontally and vertically from the steady-state position (0, 0, 0), there is a complex 3-D movement of the magnetically levitated droplet. Although the 3-D movement is complex, it presents the same rules of variation as the 3-D movement with only horizontal or vertical deviation when it is projected in the horizontal X-axis and vertical Z-axis. Fig. 8.13 (a) shows the 3-D movement of the magnetically levitated droplet with initial position (X0=2 mm, Z0=2 mm), which is projected in the horizontal X-axis and vertical Z-axis. Fig. 8.13 (b) shows the 3-D movement of the magnetically levitated droplet with different initial position (X0=3 mm, Z0=3 mm). Comparison between Fig. 8.12 and Fig. 8.13 depicts that the oscillation of the magnetically levitated droplet follows the same rules of variation in only horizontal or vertical directions.

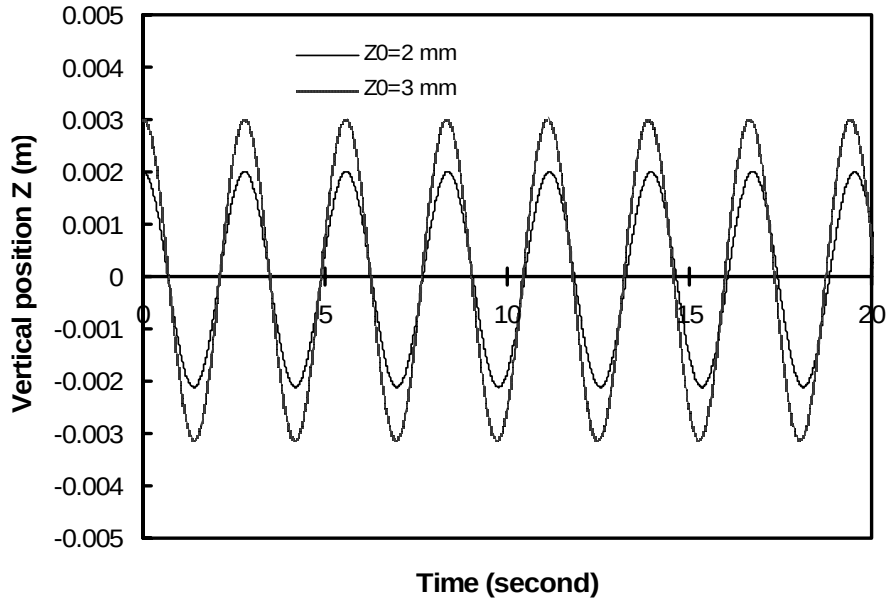

(a)

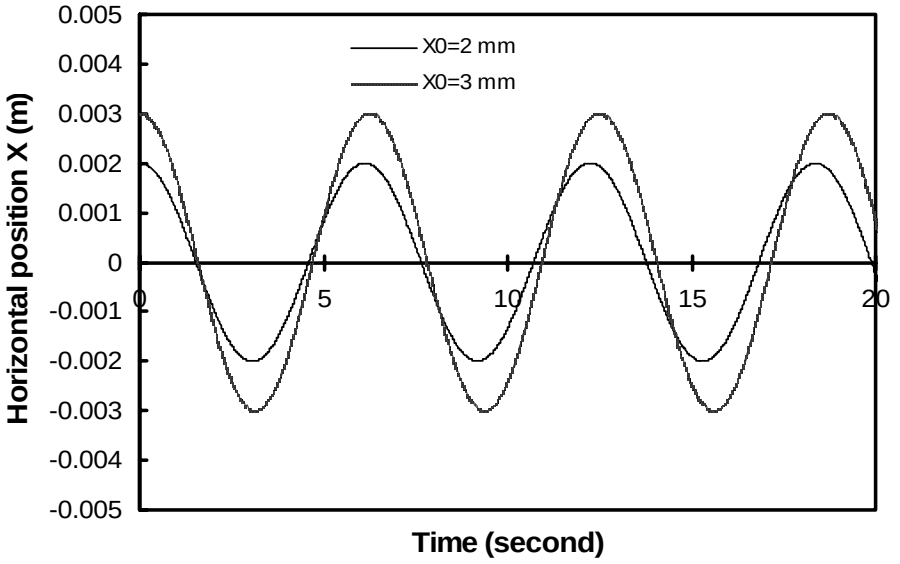

(b)

Figure 8.12 Vertical and Horizontal movements of the magnetically levitated droplets (a) Vertical movements for different initial position Z0, (b) Horizontal movements for different initial position X0

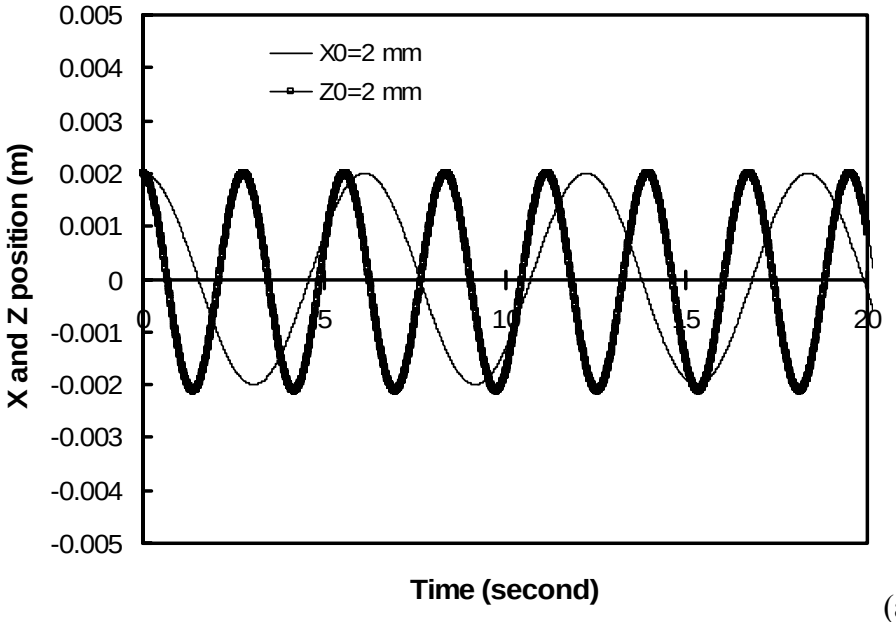

(a)

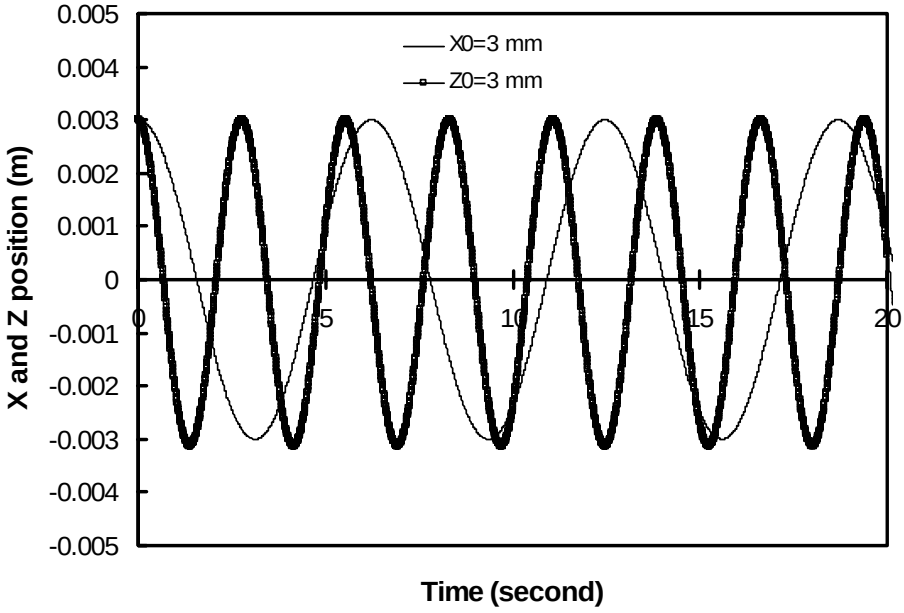

(b)

Figure 8.13 3-D movements of the magnetically levitated droplets, which is projected to the horizontal X-axis and vertical Z-axis, (a) initial position is X0=2 mm and Z0=2 mm, (b) initial position is X0=3 mm and Z0=3 mm.

8.4.4 3-D rotation of the magnetically levitated droplet

The rotation is another important 3-D movement of the magnetically levitated droplet, which is emphasized in this section. It has been observed since the early fifties when the first experiments on the electromagnetic levitation were done that under certain circumstances the levitated droplet can start to rotate or oscillate which often leads to the breakdown of the levitation melting. The rotation is undesirable because it can affect the deformation of the liquid droplet so that the measurement of the thermophysical properties of the liquid metal becomes not accurate. When the droplet is deformed, it will further reverse to change the rotation of the liquid droplet. However, in present study, the droplet is assumed to be solid sphere because the rotation has a little effect on the spherical solid droplet. Since the droplet is assumed to be spherical and the rotating movement of the droplet is self-spin-up rotation, the rotation has no effect on the translation movement of the droplet. Fig. 8.14 (a) shows the variation of the angle velocity ω with time evolving. Fig. 8.14 (b) shows the rotational angle θ and the vertical position Z with time evolving. The angle velocities ω with respect to the X and Y axis presents the oscillation which is similar to sinusoid wave, as shown in Fig. 8.14 (a). In Fig. 8.14 (b), the rotation angles θ with respect to X and Y axis present the similar oscillating characteristics to the vertical oscillating movement along the Z axis. However, the frequency of the oscillation of the rotation angles θ is lower than that for the vertical oscillating movement. Also the center of the oscillation of the rotation angles θ is not at the angle zero, which is lager than zero with respect to X axis and smaller than zero with respect to Y axis.

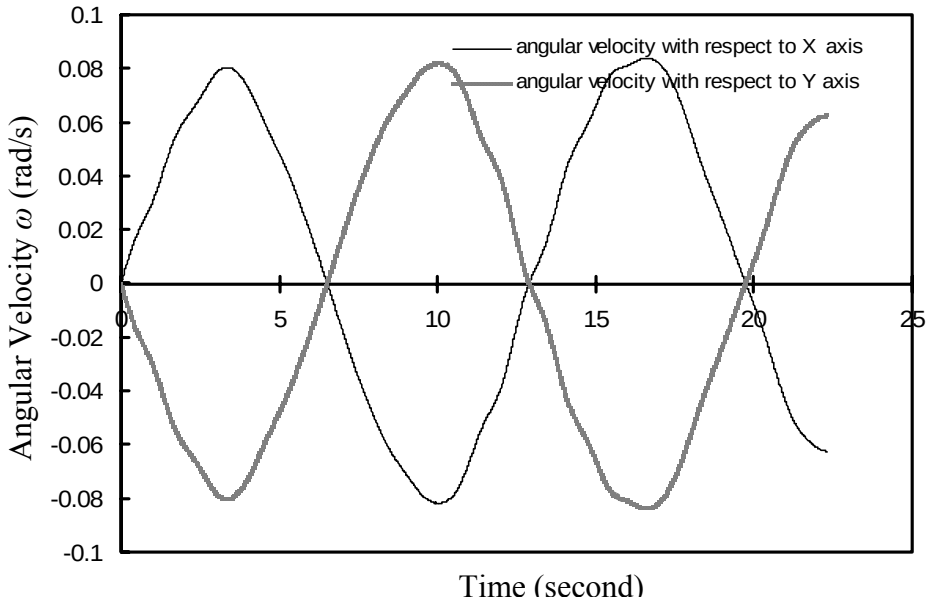

(a)

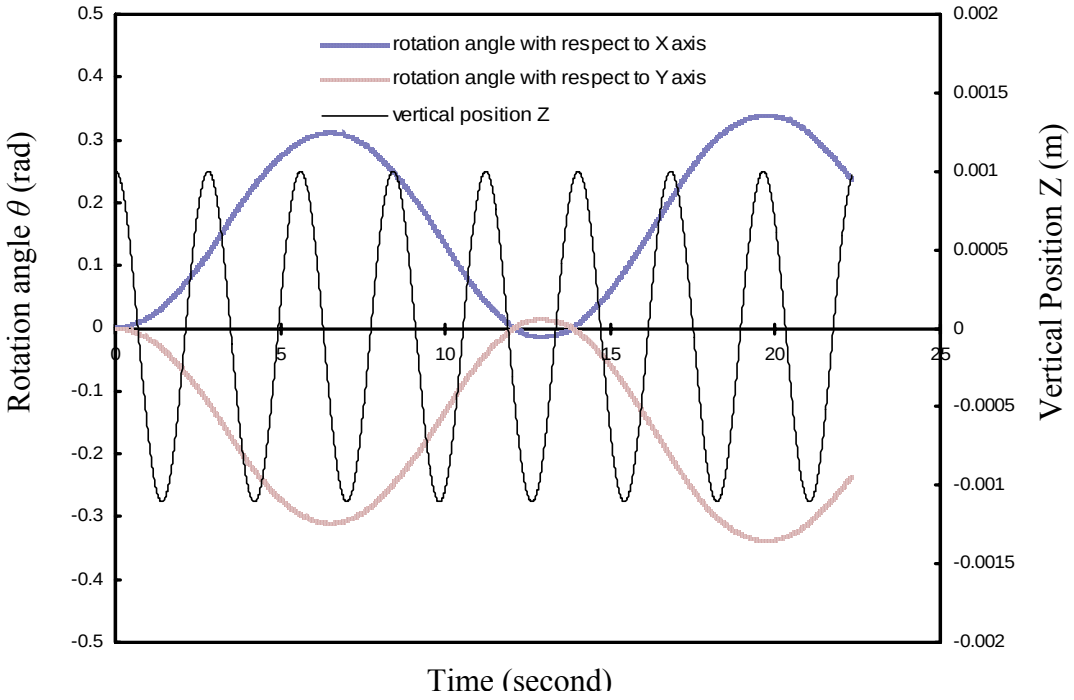

(b)

Figure 8.14 Rotating movement of the magnetically levitated droplet with the initial position (X0=0, Z0=1 mm), (a) variation of Angular velocity ω with time evolving (b) variation of rotation angle θ and vertical position Z with time evolving.

8.5 Concluding Remarks

This chapter presents the numerical study of the 3-D movement of the magnetically levitated spherical droplet using the coupled boundary and finite element methods. The hybrid boundary and finite element methods are compared with the various analytical solutions. The Whitney edge elements are used in both boundary and finite elements, which avoids the spurious solutions using the node elements. The numerical model is further tested against with the available results by calculating the Joule heating in the magnetically levitated droplet surrounded by different coils. The computed results agree with the results from the other researchers very well. When the 3-D horizontal and vertical movement of the droplet is computed in the magnetic levitation mechanism, it is found that the change of the magnitude of the initial position away from the equilibrium has no effect on the frequency and the amplitude of the oscillation of the droplet increases with the time evolving. The rotation of the droplet is also investigated. The variation of the angular velocity and rotational angle with time evolving is depicted.

BIBLIOGRAPHY

Adornato, P. M., Brown, R. A., 1983, Shape and stability of electrostatically levitated drops. *Proc. R. Soc. London A*, 389, pp. 101-117.

Ai, X., and Li, B.Q., 2004 Melt flow instability and turbulence in electro-magnetically levitated droplets, *Materials and Manufacturing Process*, Vol. 19(4), pp.737-759

Ajayi, O.O., 1978, A note on Taylor's electrohydrodynamic theory, *Proc. R. Soc. London A*, 364, pp. 499-508

Akarapu, R., Huo, Y., Li, B.Q., Tang, J. and Liu, F., Integrated modeling of microwave food processing and comparison with experimental measurements, *Journal of Electromagnetic Power and Microwave Technology*, Accepted

Bayazitoglu, Y. and Sathuvalli, U.B., 1994, Eddy current heating in an electrically conducting sphere, *J. Materials Processing and Manuf. Sci*., Vol. 3, pp. 117-141

Bayazitoglu, Y. and Sathuvalli, U.B., 1996a, The Lorentz forces on an electrically conducting sphere in an alternating magnetic field, *IEEE Trans. on Magn*., Vol. 32(2), pp. 386-400

Bayazitoglu, Y., Sathuvalli, U.B., Suryanarayana, P.V.R. and Mitchell, G.F., 1996b, The Lorentz forces on an electrically conducting sphere in an alternating magnetic field, *Physics of Fluids*, Vol. 8(2), pp. 370-383

Brazier-Smith, P.R., 1971a, Stability and shape of isolated and pairs of water drops in an electric field, *Physics Fluids*, 14, pp. 1-6

Brazier-Smith, P.R., Brook, M., Latham, J., Saunders, C.P.R. and Smith, M.H., 1971b, The vibration of electrified water drops. *Proc. R. Soc. Lond*., A322, pp. 523-534

Brown, R.A. and Scriven, L.E., 1980, The shape and stability of rotating liquid drops, *Proc. R. Soc. London A*, 371, pp. 331-357

Duff, I.S. and Reid, J.K., 1996, The design of MA48, a code for the direct solution of sparse unsymmetric linear systems of equations, *ACM Trans. Math. Softw*., 22(2), pp. 187-226

Engelman, M.S., Sani, R.L., Gresho, P.M., 1982 The implementation of normal and tangential velocity boundary conditions in finite element codes for incompressible fluid flow, *Int. J. Num. Meth. Fluid***,** 2, pp. 225-238.

Enokizono, M., Todaka, T., Yokoji, K., Wada, Y., Matsumoto, I., 1995, Three-dimensional moving simulation of levitation-melting method, *IEEE TRANSACTIONS ON MAGNETICS*, Vol. 31 (3), pp. 1869-1872

Feng, J. Q. and Beard, K. V., 1990, Small-Amplitude Oscillations of Electrostatically Levitated Drops. *Proc. R. Soc. London A*, 430*, No. 1878*, pp. 133.

Flemings, M. C., Trapaga, G. and Hyers, R., 1996, The measurement of the viscosity and surface tension of undercooled melts under microgravity conditions and supporting MHD calculations, *NASA Microgravity Materials Science Conference*, Huntsville, AL, 76.

Huo, Y., Li, B.Q., 2004a, Three-dimensional marangoni convection in electrostatically positioned droplets under microgravity, *Int. J. Heat Mass Trans*. 47, pp. 3533-3547

Huo, Y., Song, S.P. and Li, B.Q., 2004b, Droplet deformation and 2-D/3-D Marangoni flow phenomena in droplets levitated by electric fields, *Materials and Manufacturing Process* 19(4), pp. 761-775

Huo, Y., Li, B.Q., and Akarapu, R., 2004c A finite element-boundary integral method for 3-D electromagnetic heating analysis, *ASME Heat Transfer/Fluids Engineering Summer Conference*, Charlotte, North Carolina

Huo, Y. and Li, B.Q., 2005a, A mathematical model for marangoni flow and mass transfer in electrostatically positioned droplets, *Metallurgical and Materials Transactions B*, Volume 36B, pp. 271-281

Huo, Y. and Li, B.Q., 2005b, Boundary/finite element modeling of 3-d electromagnetic heating during microwave food processing, *ASME Journal of Heat Transfer*, in print

Jackson, J.D., 1975, Classical Electrodynamics (2nd edition), *New York: Wiley*

James R. Melcher, Continuum electromechanics. 1981 *Cambridge, Mass.: MIT Press*

Johns, P.B. and Beurle, R.L., 1971, Numerical solution of two-dimensional scattering problems using a transmission line matrix, *Proc. Inst. Eng*., Vol. 118, 1203-1208.

Johnson, W.L., Schroers, J. and Rhim, W.K., 2002, Studies of properties of undercooled glass forming metallic alloys, *Materials Science Conference,* Huntsville AL, pp. 307

Li, B.Q., 1993, The magnetothermal phenomena in electromagnetic levitation processes, *Int. J. Eng. Sci.,* Vol. 31, No. 2, pp. 201-220

Li, B.Q., 1994a, The fluid flow aspects of electromagnetic levitation processes, *Int. J. Eng. Sci*., Vol. 32(1), pp. 45-67

Li, B.Q., 1994b, The transient magnetohydrodynamics in electromagnetic levitation processes, *Int. J. Eng. Sci*., Vol. 32(8), pp. 1315-1336

Li, B.Q., Cui, X. and Song, S.P., A Galerkin boundary element formulation of surface radiation problems, Int. J. Boundary Element Analysis, in print

Li, B.Q., Song, S.P., 1999, Thermal and fluid flow aspects of magnetic and electrostatic levitation of liquid droplets, *J. Microgravity Sci. Tech*., Vol. XI No. 4, pp. 134-143

Lohofer, G., 1989, Theory of an electromagnetically levitated metal sphere I: absorbed power, SIAM J. Appl. Math., Vol. 49 (2), pp. 567-581

Lohofer, G., 1993, Force and torque of an electromagnetically levitated metal sphere, *J. Quarterly Appl. Math*., LI(3), pp. 495

Lohofer, G., 1994, Magnetization and impedance of an inductively coupled metal sphere, *Int. J. Eng. Sci*., 32(1), pp. 107

Mestel, A.J., 1982, Magnetic levitation of liquid metals, *J. Fluid. Mech*., Vol. 117, pp. 17-43

McDonald, B.H., Wexler, A., 1972, Finite element solution of unbounded field problems, *IEEE Trans. Microwave Theory Tech.***,** MTT-20, pp. 841-847

Muhlbauer, A., Muiznieks, A. and Jakowitsch, A., 1991, Modeling of the electromagnetic field in induction furnaces with a cold crucible, *industrielle Electrowarme*, Vol. B3, pp. 130-141

Muck, O., Germ. Pat. No. 422004 (1923)

Natarajan, R. and Brown, R.A., 1987, The role of three-dimensional shapes in the break-up of charged drops, *Proc. R. Soc. London A*, 410, pp. 209-227

Okress, E.C., Wroughton, D.M., Comenetz, G., Brace, P.H., and Kelly, J.C.R., 1952, Electromagnetic levitation of Solid and Molten Metals, *J. Appl. Phy.,* Vol. 23, No. 5, pp. 545-552

Paradis, P.F. and Rhim, W.K., 1999, Thermophysical properties of zirconium at high temperature, J. Mater. Res., Vol. 14 (9), pp.3713

Rayleigh, J.W.S., 1882, On the equilibrium of liquid conducting mass charged with electricity. *Phil. Mag.*, 14, 184.

Reitz, J. R., Milford, F. J. and Christy, R. W. 1979, *Foundations of electromagnetic theory*. Addison-Wesley, Reading, MA.

Rhim, W.K., Chung, S.K., Barber, D., Man, K.F., Gutt, G., and Rulison, A., 1993, An electrostatic levitator for high-temperature containerless materials processing in lg, *Rev. Sci. Instrum*, 64 (10), pp. 2961-2970

Rhim, W.K., 1997a, *Private Communication*, Jet Propulsion Laboratory, California Institute of Technology, Pasadena, CA.

Rhim, W.K., 1997b, Thermophysical property measurements of molten semiconductors, *NASA Microgravity Materials Science Conference*, Ed. F. Szofran, D. McCauley and C. Walker, 427

Rony, P.B., 1969, The electromagnetic levitation melting of metals, *Trans. Vac. Met. Conf.,* American Vacuum Society, Boston, 55-135

Rosenkilde, C.E., 1969, A dielectric fluid drop in an electric field, *Proc. R. Soc. Lond.,* A312, pp.473-494

Sadhal, S.S., Trinh, E.H. Wagner, P., 1996, Thermocapillary Flows in a Drop With Unsteady Spot Heating in a Microgravity Environment. *Journal of Microgravity Sci. Tech.*, Vol. 9, No. 2, pp. 80

Sathuvalli, U.B. and Bayazitoglu, Y., 1993, Electromagnetic force calculations for a concial coil, *Met. Trans*., Vol. 24B, pp. 737-748

Sathuvalli, U.B. and Bayazitoglu, Y., 1994, The Lorentz force on a sphere due to an axisymmetric non-homogeneous alternating magnetic field, *ASME Winter Meeting*, AMD Vol. 194, 293-305

Silvester, P.P., Hsieh, M.S., 1971, Finite element solution of 2-dimensional exterior field problems. *IEE Proc.,* 118, pp. 1743-1747

Song, S.P., Li, B.Q., and Khodadadi, J.M., 1998a, Coupled boundary/finite element solution of magnetothermal problems, *Int. J. Num. Meth. Heat and Fluid Flow*, 8(3), pp. 321-349

Song, S.P. and Li, B.Q., 1998b, A boundary/finite element analysis of magnetic levitation systems in normal and micro gravity: surface deformation and thermal phenomena, *ASME Journal of Heat Transfer*, 120, pp. 491-503

Song, S.P., Li, B.Q., 1999a, A coupled boundary/finite element method for the computation of magnetically and electrostatically levitated droplet shapes, *Int. J. Numer. Meth. Engng*., VOL. 44, pp. 1055-1077

Song, S.P. 1999b, Finite element analysis of surface oscillation, fluid flow, and heat transfer in magnetically and electrostatically levitated droplets, *Ph.D thesis*, Washington State University, Pullman, WA

Song, S.P., Dailey, P., Li, B.Q., 2000a, Effects of heating source arrangements on internal convection in electrostatically levitated droplets. *AIAA J. Thermophy. Heat Trans*., *14 (3)*, pp. 335-362.

Song, S.P. and Li, B.Q., 2000b, Free surface shapes and thermal convection in electrostatically levitated droplets, *Int. J. Heat Mass Trans*., *43*, pp. 3589-3606.

Song, S.P., Li, B.Q., 2001, A hybrid boundary/finite element method for simulating viscous flows and shapes of droplets in electric fields, *Int. J. Comp. Fluid Dynamics*, *15*, pp. 293-308.

Suryanarayana, P.V.R. and Bayazitoglu, Y., 1991, Effect of static deformation and external forces on the oscillations of levitated droplets, *Physics of Fluids A*., Vol. 3, pp. 967-977

Taylor, G.I., 1964, Disintegration of water drops in an electric field, *Proc. R. Soc. Lond. A*, 280, pp. 383-397

Taylor, G.I., 1966, The force exerted by an electric field on a long cylindrical conductor, *Proc. R. Soc. Lond. A*, 291, pp. 145-159

Torza, S., Cox, R.G., and Mason, S.G., 1971, Electrohydrodynamics deformation and burst of liquid drops. Phil. Trans. R. Soc. Lond. *A. 269*, pp. 295

Tsamopoulos, J.A. and Brown, R.A., 1984, Resonant oscillations of inviscid charged drops, *J. Fluid Mech*., vol. 147, pp. 373-395

Weatherburn, C.E., 1930, *Differential geometry of three dimensions*. Cambridge University Press Fetter Lane, London

Zgraja, J., 1991, The current concentrations for induction heating, *industrielle Electrowarme*, Vol. B3, pp. 142-148

Zong, J.H., Li, B.Q., and Szekely, J., 1992, The electrodynamic and hydrodynamic phenomena in magnetically-levitated droplets, Part I. steady state behavior, *Acta Astronautica*, 26(6), pp. 435-449

Zong, J.H., Li, B.Q., and Szekely, J., 1993, The electrodynamic and hydrodynamic phenomena in magnetically-levitated droplets, Part II. transient behavior and heat transfer considerations, *Acta Astronautica*, 29(4), pp. 305-311